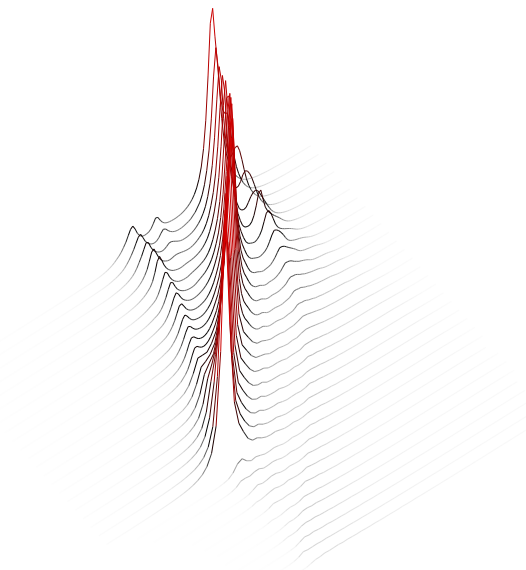


INSTITUTE FOR
THEORY OF CONDENSED MATTER
DEPARTMENT OF PHYSICS



Dynamics of one-dimensional electron systems



PhD thesis

by

Tobias Küchel né Ulbricht

Examiner: Prof. Dr. Peter Wölfle
Second examiner: Prof. Dr. Alexander Mirlin
Date of Examination: October 23, 2009

The cover art depicts the spectral response of a one-dimensional Hubbard chain in a magnetic field upon removing an electron with spin $+\frac{1}{2}$, revealing the underlying elementary excitation in the spin (left branch) and charge sectors (main red branch).

Dynamics of one-dimensional electron systems

Zur Erlangung des akademischen Grades eines
DOKTORS DER NATURWISSENSCHAFTEN
von der Fakultät für Physik der Universität (TH) Karlsruhe

genehmigte

DISSERTATION

von

Tobias Küchel geb. Ulbricht

aus Schwäbisch Hall

Referent: Prof. Dr. Peter Wölfe
Korreferent: Prof. Dr. Alexander Mirlin
Tag der Prüfung: 23. Oktober 2009

Contents

Contents	v
1 Introduction	1
1.1 Structure of the manuscript	3
1.2 Publication list	3
2 Methods: Theory	5
2.1 One-dimensional models	5
2.1.1 The tight-binding model	5
2.1.2 The Hubbard model	6
2.2 Time-evolution of a Gaussian potential	7
2.3 Time-evolution of an additional electron	11
2.4 Dynamical correlation functions	17
2.5 Summary	22
3 Methods: Simulation	25
3.1 Exact diagonalisation	25
3.2 The Density Matrix Renormalisation Group	27
3.2.1 Infinite lattice algorithm	27
3.2.2 Finite lattice algorithm	31
3.3 Time development DMRG	31
3.3.1 Full td-DMRG	32
3.3.2 Adaptive td-DMRG	32
3.4 Dynamical correlation functions: DMRG	33
3.5 Summary	34
4 Spin-charge separation	35
4.1 Luttinger liquid	35
4.2 Hubbard model in one dimension	37
4.3 Observation of spin-charge separation	38
4.3.1 Experimental evidence	40
4.3.2 Numerical simulation evidence	41
4.4 Spin-charge separation of one electron in the Hubbard model	41
4.4.1 Non-interacting case	42
4.4.2 Strongly interacting case	44
4.4.3 Spin-charge separation in a transport setup	46

4.5	Spectral function in the Hubbard model	49
4.5.1	Spectral function	49
4.5.2	Half-filled band	52
4.5.3	Below half-filling	53
4.5.4	Trapped Hubbard model	55
4.6	Summary	59
5	Spin polarisation	61
5.1	Tracking spin and charge	63
5.2	Spin imbalance: A closer look	67
5.3	Summary	70
6	SU(3) colour-charge separation	73
6.1	Colour-charge separation in the Hubbard model	74
6.1.1	Introduction to SU(3)	74
6.1.2	Hubbard model	75
6.1.3	Additional fermion	75
6.1.4	Gaussian perturbation	77
6.2	Summary	78
A	Appendix	81
A.1	Error analysis for time evolution with DMRG	82
A.2	Towards numerics on graphics cards	84
	Bibliography	87

Acknowledgements

I am very grateful to my supervisor and mentor, Peter Schmitteckert, who advised, helped and motivated me during the many years of this thesis. Especially during times, when the system administration absorbed most of my resources, he convinced me, along with Prof. Peter Wölflé and my wife Christina that I could make it. I thank my advisors Prof. Peter Wölflé and Prof. Alexander Mirlin for making it possible for me to achieve this PhD by employing me, examining the work and supporting me all the time.

Christina, you believing in me made and still makes my day. Every day.

During the last months, I profited a lot from discussions with members of the institute, Dmitry Aristov, Alexander Branschädel, Stefan Kremer, Stefan Rachel, Johannes Reuter, Burkhard Scharfenberger, Michael Schütt, Ronny Thomale and many more. Holger “ \hbar ” Schmidt, thank you for the great time and now, “let it rock and let it roll”.

There are many people that made the time worthwhile, above all Rose Schrempp, Andreas Poenicke and Daniel Hermann for the great teamwork, the TKM and TFP institute with ever more challenges for our IT management, my crazy family Ulbricht and the Kùchels for supporting and comforting me. There is no better public place to mention Jens, Miruna, Peter, Malte, Wiebke, Barbara and Patrick, Alex und Tac and all my friends for their enduring friendship and support.

I dearly thank the voluntary work of the GNU/Debian, Ubuntu and many more free software communities. Special mentioning deserve the GNU/Debian utilities, gnuplot, bash, GNU compiler, python, inkscape, emacs and latex, which were mainly used to create all of this work. Additionally, I exceedingly exploited the service of Radio Český Rozhlas D-dur providing high-quality classical music.

1 Introduction

‘‘The chances of finding out what really is going on are so absurdly remote that the only thing to do is to say hang the sense of it and keep yourself occupied. Look at me: I design coastlines. [...] I’d far rather be happy than right any day.’’

(Slartibartfast in *The Hitchhiker’s Guide to the Galaxy*, Douglas Adams)

An estimated 4.4 billion people on the planet (2/3 of the world’s population) use mobile phones for their every day lives, as of August 2009¹, with the fastest growth coming from newly industrialised and developing countries. These two facts (mass and growth) show that the miniaturisation reaching from yesterday’s micro-electronics (as in mobile phones) via nano-technology of today down to the atomic scale has a huge social and economical impact on the world. For example, every shrinking step in the CMOS microchip technology up to now resulted in an enhanced performance and capacity together with a reduced energy consumption per operation.

At the atomic level of $\sim 0.1\text{nm}$, (quasi-)one- and two-dimensional objects become the building blocks for technological structures. Besides the scientific curiosity there is a global demand to understand how electronics (or spintronics, photonics) work in these low-dimensional systems. Due to the domination of quantum-mechanics over electro-mechanics at this scale, the physical challenges here are incredibly manifold and physicists explore, among many more, the effects of interaction, single impurities or disorder, frustration, temperature and external fields. We concentrate in this thesis on strictly one dimension (one-dimensional atomic chains), where we investigate mainly the effect of interaction on the dynamics of electrons.

Why electrons in one dimension? The geometry of electron systems in one dimension is *less complex* than in higher dimensions, which allows us to employ numerical tools that can solve the full many-body problem. Equally important, the step to one dimension involves a *change of paradigms*. While metals in geometries of dimension larger than two are well described by a Fermi liquid of effectively free fermions with renormalised parameters, metals in one dimension may be Luttinger liquids with inherently different properties: Most notably, the quasi-particle description breaks down and all low-energy excitations are of a collective and bosonic nature. This has far reaching consequences. For instance, if we put an electron into an interacting chain of electrons, it fractionalises, i.e. gets decomposed into spin “spinon” and charge “holon” degrees of freedom. This so-called spin-charge separation is one of the major theoretical and most counter-intuitive predictions that still awaits to be clearly experimentally verified. Other peculiarities in one-dimensional strongly correlated systems are non-universal power-law decays of

¹http://www.eito.com/pressinformation_20090807.htm

correlation functions, the Anderson localisation and the unresolved interplay between disorder and interaction.

This work The strongest emphasis within this thesis lies on spin-charge separation. We ask the following question: What happens to an electron, when it is injected into an interacting one-dimensional structure? One is usually interested in transport properties and as a first step towards non-equilibrium transport, we compute the exact time evolution of an electronic wave packet as it moves through a non-interacting or an interacting metal.

In analogy to the $SU(2)$ spin-symmetric case of interacting electrons, we take the excursion to investigate the more artificial case of $SU(3)$ symmetric particles. While $SU(3)$ symmetry is rather known from quantum-chromodynamics (the colour property of quarks), using the technology of ultra-cold atomic gases, realisations of artificial $SU(3)$ “colour” particles are already work in progress. In similar time evolution simulations, we show how colour and charge, too, separate as soon as interaction comes into play.

Back in the familiar domain of real electrons, we ask further: How does the fractionalisation of the electron take place? In frequency and momentum domain, the dynamic response of an electronic excitation – the spectral function – gives much more information about the underlying physics and it is experimentally much better accessible. We compute the trajectory of the electron response as it decomposes into the spinon and holon responses along a parameter as simple as an external magnetic field. Along the way, we find that these questions are also rich in new and unexplained physics.

As mentioned first, one dimension is not only an undesirable restriction, it turns out to be an advantage, too. Our main tool, the density matrix renormalisation group (DMRG) is best suited for these kinds of problems. There is no other numerical software so far that can accomplish in higher dimensions what the DMRG does in one dimension. Since reality is far too complex to simulate, we have to reduce the complexity. On the one hand, DMRG projects the problem onto a smaller subspace of the Hilbert space and this projection is optimal for the quantity we aim to calculate. On the other hand, we simulate reality by using the simplest non-trivial models. In particular, we use the single-band Hubbard model as a prototypical model of interacting electrons in one dimension. The Hubbard model is exactly solvable in one dimension by the Bethe ansatz and thus serves as an optimal playground to benchmark numerical results. In the low-energy regime close to half-filling the Hubbard model is well described by a Luttinger liquid and we can always compare our results in that limit to analytical predictions of Luttinger liquid theory. But as a major benefit of DMRG, we can access the full energy and momentum range and work at any interaction strength of the Hubbard model.

Finally, although we speak of modelling and simplification, there are real materials that carry a clear one-dimensional character. These are certain polymers, some organic molecules and fabricated nano-structures like single-wall carbon nano-tubes or even nano-wires, where atoms are placed in a chain on edges of a substrate, which comes very close to what we model. The reason is that in these materials the intra-chain coupling is magnitudes stronger than the inter-chain coupling in the other two dimensions.

They are invaluable for the verification or falsification of theoretical predictions. Last but not least, ultra-cold atomic gases are already now a standard environment to imitate solid state physics. To accommodate this fact, we examined cases that include an additional trap potential which is sometimes found in the optical lattices.

1.1 Structure of the manuscript

This thesis is divided into six parts. While chapter 1 and 2 are introductory material only, chapter 3 introduces the numerical method (DMRG) and chapter 4 presents various aspects of the spin and charge separation and our research on the dynamics of electrons within the subject. In Chapter 5, we investigate the effect of a magnetic field on the observability of the specific nature of one dimension. Finally, chapter 6 shortly discusses that the one-dimensional physical peculiarities are not restricted to the usual SU(2) spin- $\frac{1}{2}$ physics and can be extended to the SU(3) case. The appendix extends some of the error analysis of chapter 2 and introduces the novelty of graphics card numerics for physical simulation.

For quick reading, we provide a short introduction at the beginning of each chapter and a summary at the end of each chapter. The main results and outlooks are thus comprised in the summaries of chapter 4, 5 & 6.

1.2 Publication list

Parts of section 4.4 are published in

- *Is spin charge separation observable in a transport experiment?* [1]
T. Ulbricht, P. Schmitteckert
EPL **86**, 57006 (2009).
- *Signal transport in and conductance of correlated nanostructures.* [2]
Tobias Ulbricht and Peter Schmitteckert.
In Wolfgang E. Nagel, Dietmar B. Kröner, and Michael Resch, editors, *High Performance Computing in Science and Engineering '08*, pages 71–82. Springer, Berlin, 2008.

The benchmarking of appendix A.2 and parts of section 3.2.1 are part of the publication

- *Conductance of correlated nanostructures.* [2]
Alexander Branschädel, Tobias Ulbricht and Peter Schmitteckert.
to be published in *High Performance Computing in Science and Engineering '09*

Parts of chapter 5 are in preparation to be published in

- *Tracking spin and charge with spectroscopy in polarised systems*
T. Ulbricht, P. Schmitteckert
submitted to Europhysics Letters (EPL)
preprint: arXiv:0910.1827v1

Scientific work of chapter 6 is prepared to be published in

- *Colour-charge separation in trapped $SU(3)$ fermionic atoms*
T. Ulbricht, R. Molina, R. Thomale, P. Schmitteckert
in preparation

Other publications:

- *Magnetic excitations in a bond-centered stripe phase: Spin waves far from the semi-classical limit* [3]
Matthias Vojta and Tobias Ulbricht
Phys. Rev. Lett. **93**, 127002–127006 (2004).

Conference contributions:

- *Is Spin-charge Separation observable in transport experiments?*
Oral presentation
72. Jahrestagung der DPG und DPG Frühjahrstagung des Arbeitskreises Festkörperphysik, Berlin 2008
- *Wave Packet Dynamics in Disordered Quantum Systems*
Poster presentation
384. Wilhelm and Else Heraeus Seminar, Nonequilibrium Transport of Strongly Correlated Systems, Bad Honnef 2007

2 Methods: Theory

There is a theory which states that if ever anyone discovers exactly what the Universe is for and why it is here, it will instantly disappear and be replaced by something even more bizarre and inexplicable. There is another theory which states that this has already happened.
(from *The Restaurant at the End of the Universe*, Douglas Adams)

This chapter shortly presents the underlying models which we will investigate in later chapters. We derive the dynamics of excitations caused by an external potential or by an addition of an electron in a tight-binding chain. Further, we investigate the extraction of real-time variables as well as the single particle spectral function and how the finite-sized lattice effects them.

2.1 One-dimensional models

We assume that the reader is familiar with Quantum mechanics and the formalism of second quantisation and the basics of solid state theory. Further, the knowledge of Fermi liquid theory in chapter 4 makes it easier to see a difference to the Luttinger liquid concept sketched there.

We will only consider lattice models in this work. This is a major restriction, since most analytic models are based on the continuum “thermodynamic” limit. However, considering finite lattice models are closer to experimental realisation than their continuum counterpart when it comes to nano-technological fabrication of, especially, purely one-dimensional arrays.

2.1.1 The tight-binding model

We use the common simplest approach to a solid state crystal, the tight-binding method, where the band structure of conducting electrons is constructed by overlapping atomic orbitals and restricting to nearest neighbour hopping between the localised states. On a lattice with M sites, N spinless fermions, the simplest tight-binding Hamilton operator is defined (in second quantisation) as

$$H_{\text{tb}} = -t_{\text{tb}} \sum_{x=1}^M (c_x^\dagger c_{x-1} + c_{x-1}^\dagger c_x), \quad (2.1)$$

where c_x are annihilation operators at position x and t_{tb} is the hopping matrix element, which is constant and set to 1 in all our treatments. Above Hamiltonian represents a

tridiagonal matrix in the single particle basis $\{c_x\}$. The analytical solution by Fourier transformation leads to the diagonal Hamiltonian

$$H_{\text{tb}} = \sum_k \varepsilon(k) c_k^\dagger c_k, \quad (2.2)$$

where $\varepsilon(k) = -2t_{\text{tb}} \cos(k)$ defines the dispersion relation of single particle states k . The system is very sensitive to the boundary conditions. The M levels are discretely distributed over the cosine band, but while for hard-wall boundary conditions (HWBC, omit c_0 term) one has $k = n\pi/(M+1)$, $n \in \{1, \dots, M\}$, the periodic boundary conditions (PBC, $c_0 = c_M$) yield $k = \frac{2\pi(n-1)}{M} - \pi$ and the anti-periodic (twisted) boundary conditions (APBC, $c_0 = -c_M$) fit on the cosine with $k = \frac{\pi(2n-1)}{M} - \pi$, see Fig. 2.1. The choice of

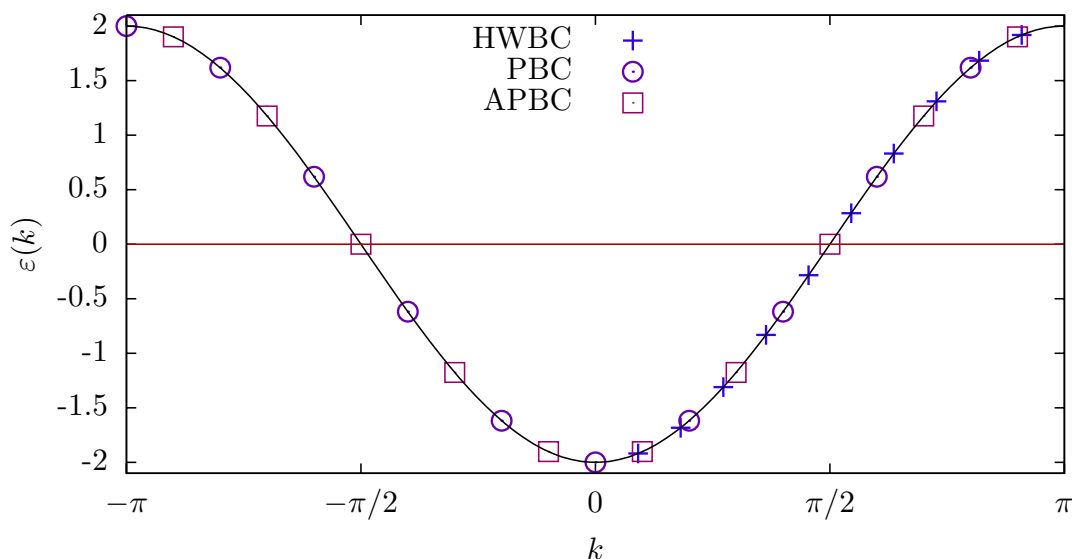


Figure 2.1: Energy levels of the tight-binding Hamiltonian for different boundary conditions placed on the cosine band dispersion.

boundary conditions is crucial for the calculation of ground state properties. As seen in Fig. 2.1, for 10 sites, the Fermi energy was drawn at $\varepsilon(k) = 0$ corresponding to 5 fermions occupying the lowest levels for HWBC or PBC. However, APBC are unsuitable for this combination of sites and particles, since the ground state would be degenerate. APBC should be used whenever $M/2$ is even.

2.1.2 The Hubbard model

Allowing more than one particle type on each site in a lattice, one writes down a tight-binding model for each type. The simplest interaction that connects the particle types, is an on-site interaction between the densities. One immediately arrives at the famous Hubbard model, which is for electrons having two possible spin orientations in S_z given

by

$$H_{\text{Hubbard}} = \sum_{\sigma=\uparrow,\downarrow} H_{\text{tb},\sigma} + U \sum_{x=1}^M \left(\hat{n}_{x,\uparrow} - \frac{1}{2} \right) \left(\hat{n}_{x,\downarrow} - \frac{1}{2} \right). \quad (2.3)$$

Here, $n_{x,\sigma} = c_{x,\sigma}^\dagger c_{x,\sigma}$ and we have written the interacting term $U n_\uparrow n_\downarrow$ already in a particle-hole symmetric way by adding corresponding chemical potentials $-\frac{1}{2}U \sum_\sigma n_\sigma$ and $\frac{1}{4}U$ at each site.

Although being simple to write down, the Hubbard model is yet far from being completely understood, even in one dimension [4]. The most prominent property is the metallic character for any filling, except for the commensurate filling $\nu = 0.5$ (= “half-filling” with M particles on M sites), where the system becomes a Mott insulator where the elementary excitations in the charge sector acquire a gap. One major advantage is the exact solvability of the model within the Bethe ansatz. In section 4.2 we will sketch how the notion of “spinons” and “holons” are established using the exact solution.

Further, particle numbers of both spin types are conserved separately and the SU(2) symmetry yields the conservation of spin. Beyond that, the Hubbard model has more subtle symmetries. For example, the reversal of all spins leaves the Hubbard Hamiltonian invariant. Also, when particles and holes are exchanged for both spin species with a factor of (-1) on every second site, then, together with a switch of sign in the interaction U , the Hubbard Hamiltonian with appropriate boundary conditions is invariant under this so-called “Shiba transformation”. It allows for the construction of so-called “ η -pairing” operators that generate a second SU(2) symmetry, which is hidden in the Hubbard Hamiltonian at first sight. This symmetry allows to exploit mappings between the attractive and the repulsive Hubbard model.

In the strong coupling limit, the Hubbard model prohibits double occupation and upon this projection from 4 to three possible states at each site, the Hubbard model transforms into the t - J -model and for half-filling into the antiferromagnetic Heisenberg model. Then only the spin interaction $J = (4t^2)/U$ governs the dynamics.

2.2 Time-evolution of a Gaussian potential

Let us look at a lattice with M sites and N spinless fermions. Our time evolution Hamiltonian will be called H_0 and for now let us use the tight-binding Hamilton operator

$$H_0 = H_{\text{tb}} = -t_{\text{tb}} \sum_{x=1}^M (c_x^\dagger c_{x-1} + \text{h.c.}) \quad (2.4)$$

with arbitrary boundary conditions. This Hamiltonian is distorted in the density at time $t = 0$ by a Gaussian potential of width σ_x , height $\frac{1}{\sigma_x\sqrt{2\pi}}$ around the position x_0

$$H_1 = H_0 + \sum_{x=1}^M G(x) c_x^\dagger c_x,$$

$$G(x) = \frac{1}{\sigma_x\sqrt{2\pi}} e^{-\frac{(x-x_0)^2}{2\sigma_x^2}}.$$

At time $t = 0$, the Hamiltonian is diagonalised by some unitary matrix U^G , defined by $U^{G\dagger} H_1 U^G = \text{diag.}$ and the local operator basis transforms as

$$\begin{aligned} \mathbf{c} &= U^G \mathbf{d}, & \mathbf{d} &= U^{G\dagger} \mathbf{c}, \\ \mathbf{c}^\dagger &= \mathbf{d}^\dagger U^{G\dagger}, & \mathbf{d}^\dagger &= \mathbf{c}^\dagger U^G. \end{aligned}$$

The ground state of H_1 is made of the N single particle states $\{|d_p\rangle\}$ with the lowest energy $\varepsilon(p)$:

$$|\phi\rangle = \prod_{p \leq p_F} d_p^\dagger |0\rangle \quad (2.5)$$

$$= \prod_{p \leq p_F} \sum_x c_x^\dagger U_{xp}^G |0\rangle. \quad (2.6)$$

At time zero the unevolved local fermion density is simply

$$\hat{n}(x) = \langle \phi | c_x^\dagger c_x | \phi \rangle = \sum_{l,k} U_{lx}^{G\dagger} U_{xk}^G \delta_{l,k} \Theta(p_F - k) = \sum_{k \leq p_F} U_{xk}^{G*} U_{xk}^G = \sum_{k \leq p_F} |U_{xk}^G|^2 \quad (2.7)$$

Time evolution

At times $t > 0$, the Gaussian distortion is turned off. Thus, the system evolves with the undistorted Hamiltonian H_0 and the time evolution operator $A = e^{-iH_0 t}$. For our convenience, we do not use the Heisenberg picture, instead, we follow the evolution of the single particle states $|d_p\rangle$, given by $|t\rangle = A |d_p\rangle$. This defines us a basis set of operators t that create the state $|t\rangle$ at time t . In matrix notation the operators transform as

$$\begin{aligned} \mathbf{d} &= A \mathbf{t}, & \mathbf{t} &= A^\dagger \mathbf{d}, \\ \mathbf{d}^\dagger &= \mathbf{t}^\dagger A^\dagger, & \mathbf{t}^\dagger &= \mathbf{d}^\dagger A. \end{aligned}$$

H_0 and thus A are usually given in the space representation basis set $\{|c_x\rangle\}$. However, we need them in $\{|d_p\rangle\}$ basis.

$$A = e^{-iH_0 t} = \sum_{x,x'} [A^{(x)}]_{x,x'} c_x^\dagger c_{x'} = e^{-it \sum_{k,l} [H_0^{(d)}]_{k,l} d_k^\dagger d_l} = \sum_{k,l} [A^{(p)}]_{kl} d_k^\dagger d_l \quad (2.8)$$

where the basis transformations are given by

$$[H_0^{(p)}]_{k,l} = \sum_{x,x'} U_{kx}^{G\dagger} [H_0^{(x)}]_{x,x'} U_{x',l}^G \quad \text{and} \quad [A^{(p)}]_{k,l} = \sum_{x,x'} U_{kx}^{G\dagger} [A^{(x)}]_{x,x'} U_{x',l}^G. \quad (2.9)$$

The matrices $A^{(p)}$ and $A^{(x)}$ are matrix exponentials of the Hamiltonian $-iH_0t$ in the corresponding basis. Additionally, to calculate the matrix exponentials it might be sometimes helpful to go into the diagonal basis of H_0 , exponentiate the diagonal entries and transform back.

At arbitrary times t the time-evolved initial state can now be constructed using the single particle states at that time

$$|\phi(t)\rangle \equiv \prod_{a \leq n_F} t_a^\dagger |0\rangle, \quad (2.10)$$

and since we can express now the old operators in terms of the new $t_a^\dagger = \sum_l d_l^\dagger [e^{-iH_0t}]_{la}$, the local fermion density can now be expressed as

$$\hat{n}(x,t) = \langle n_x \rangle(t) = \langle \phi(t) | c_x^\dagger c_x | \phi(t) \rangle \quad (2.11)$$

$$= \sum_{p,q} U_{px}^{G\dagger} U_{xq}^G \langle \phi(t) | d_p^\dagger d_q | \phi(t) \rangle \quad (2.12)$$

$$= \sum_{l,l'} \sum_p A_{lp}^\dagger U_{px}^{G\dagger} \sum_q U_{xq}^G A_{q'l'} \langle \phi(t) | t_l^\dagger t_{l'} | \phi(t) \rangle \quad (2.13)$$

$$= \delta_{l,l'} \Theta(n_F - l) \cdots = \sum_{l \leq l_F} \tilde{V}_{lx}^\dagger(t) \tilde{V}_{xl}(t) \quad (2.14)$$

with $\tilde{V}_{xl}(t) = \sum_q U_{xq}^G [A^{(p)}]_{ql}$ or equivalently $\tilde{V}_{xl}(t) = \sum_{x'} [A^{(x)}]_{x'x} U_{x'l}^G$.

Real-time simulations We want to estimate the finite-size effects for simulations on a lattice. To compare to systems with interaction later, we will here use (2.14) to calculate the evolution of the velocity of an initial Gaussian density distribution in a non-interacting environment. We use a system of M sites with periodic boundary conditions and choose the centre of the potential $x_0 = M/2$.

When we plot the density at time steps $t = 0$ and $t = 2.5$, we see (Fig. 2.2) that the initial peak has split and symmetrically travelled to the right and left. What happened? Our initial Gaussian potential is small and we expect a Gaussian density distribution in linear response. Further, in momentum space the small perturbation invokes a low-energy response, i.e. only low-lying states of width $\sigma = \frac{1}{2\pi\sigma_x}$ around the Fermi surface points $|k_F|$ are excited. More explicitly, states around $+k_F$ and $-k_F$ are excited on the same footing and lead in turn to Gaussian density distributions travelling in both directions.

The analysis also shows that the broader the peak is in real space, the narrower the excitations will be distributed and the closer they will lie to the Fermi surface points.

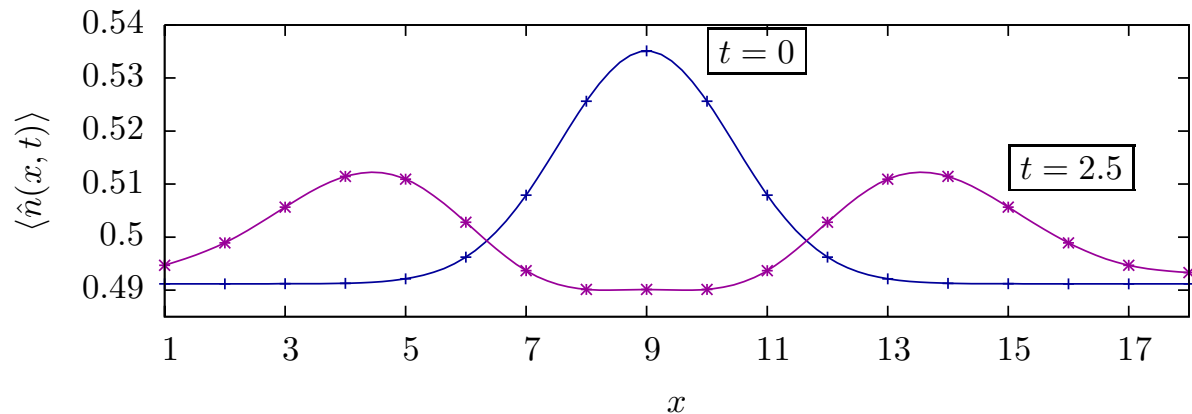


Figure 2.2: Wave packets at initial and a finite time step of a $M = 18$ sized system and an initial Gaussian distortion of width $\sigma_x = 1.5$ around $x_0 = M/2$.

We can visualise this by extracting the velocity of the peak by tracking the maximum of one of the peaks and calculating the difference quotient for each time step

$$v(t) = \frac{\max_x \langle \hat{n}(x, t) \rangle - x_0}{t}. \quad (2.15)$$

We extract the maximum at each time step in two ways: in the first way by resampling the data points using cubic splines and taking the maximum value and second, by fitting two Gaussians over the dataset and taking the centre of the Gaussian as the maximum. The velocity is plotted in figure 2.3 for several system sizes and peak widths σ_x using Gaussian fits. The prefactor of the potential is adjusted to normalise the Gaussian perturbation, which implies a lower height (a smaller displacement) for broader packets.

At first, it takes some time for the two peaks to become clearly separated. Only then the Gaussian fit procedure finds a clear centre. We will take a separation time of $t_i = 2\sigma_x/v$, where we assume $v \approx 2$. After that there is a plateau of constant velocity for as long as the peak is far enough from the boundary, where it meets with the opposite peak when using periodic boundary conditions. Thus, the end of the plateau is given by $t_f = (M - x_0)/v - 2\sigma_x/v$. Clearly, a clean plateau for $t_i \lesssim t \lesssim t_f$ limits the width of the peak for a given system size. Figure 2.3 shows that $\sigma_x = 1.5$ is the maximum sensible width for an $M = 18$ sites system. On the other hand, for a given width the value of the velocity plateau does not change when increasing the system size, c.f. $\sigma_x = 4.0$ for $M = 42, 102$ in figure 2.3. Finally, the inset in figure 2.3 shows how the average velocity, fitted between t_i and t_f , approaches the asymptotic value of 2 (in units of $t_{\text{tb}} = 1$) with increasing widths of the wave packet. This is the expected behaviour for non-interacting fermions on a lattice within a half-filled tight-binding system, where the Fermi velocity at $k_F = \pm\pi/2$ is $v_F = \left. \frac{\partial \varepsilon(k)}{\partial k} \right|_{k_F} = 2t_{\text{tb}} \sin(k_F) = \pm 2t_{\text{tb}}$. The asymptotic velocity will be reached for an infinitely broad peak (infinitely small perturbation). The difference between the spline-fit and the Gaussian fit velocity shows there is some inaccuracy of defining the centre of a peak. For interacting systems, the Fermi velocities for different

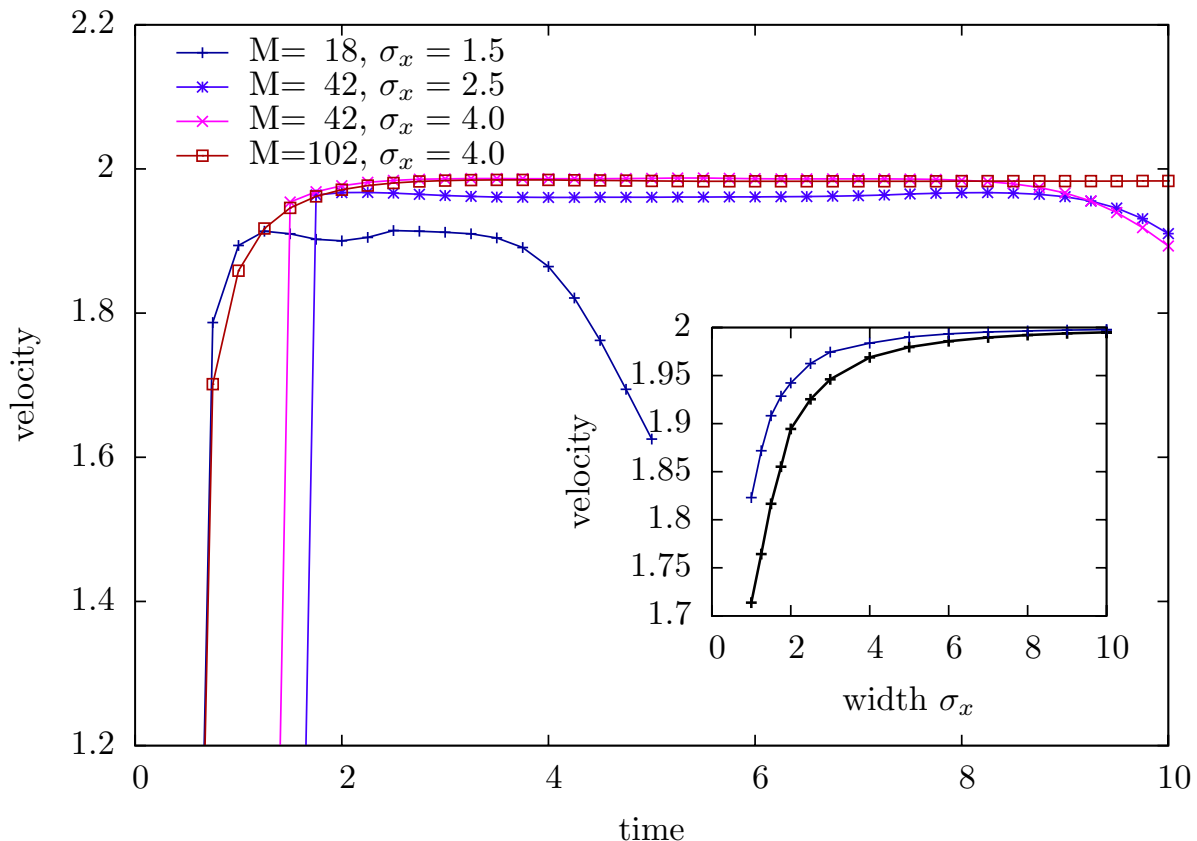


Figure 2.3: Wave packet velocities for different initial Gaussian potential widths and system sizes as a function of time using periodic boundary conditions. The inset shows the extracted velocity averaged over the plateaus as a function of the real-space Gaussian potential width when using splines over the dataset (black curve) and when fitting a Gaussian shape to the datasets (blue curve).

excitations will differ from $|v_F| = 2t_{\text{tb}}$. The main message of figure 2.3 is that for the interacting system one can estimate the deviation of a finite sized excitation from an ideal excitation as one already knows the deviation in the corresponding non-interacting system.

Note that using hard-wall boundary conditions induce Friedel oscillations in the density depending on the filling, which complicates the tracking of the density peak, especially on small systems. The uncertainty in the extraction of a velocity coming with it will add to the deviation from the infinite system.

2.3 Time-evolution of an additional electron

In contrast to the previous section, we want to do time evolution on an excited state, more precisely, on a state, where the ground state has one additional electron (or hole). We take again a lattice with M sites, N spinless fermions, use the free fermion tight-

binding Hamilton operator as H_0 to be able to extract the observables analytically:

$$H_0 = -t_{\text{tb}} \sum_{x=1}^M (c_x^\dagger c_{x-1} + \text{h.c.}) \quad (2.16)$$

The Hamiltonian is again diagonalised by U^0 into the eigenbasis $\{|d\rangle\}$. In matrix notation we have

$$\begin{aligned} \mathbf{c} &= U^0 \mathbf{d}, & \mathbf{d} &= U^{0\dagger} \mathbf{c}, \\ \mathbf{c}^\dagger &= \mathbf{d}^\dagger U^{0\dagger}, & \mathbf{d}^\dagger &= \mathbf{c}^\dagger U^0. \end{aligned}$$

The ground state $|\Psi\rangle$ is given by

$$|\Psi\rangle = \prod_{p \leq p_F} d_p^\dagger |0\rangle \quad (2.17)$$

$$= \prod_{p \leq p_F} \sum_x c_x^\dagger U_{xp}^0 |0\rangle, \quad (2.18)$$

where p enumerates the eigenstates with the energies $\varepsilon(p)$. E.g. for the tight-binding model with periodic boundary conditions, $[U^0]_{xk}$ is the Fourier transformation e^{-ikx} with the eigenstates being Bloch states enumerated by the wave vector k with $\varepsilon(k) = -2t_{\text{tb}} \cos(k)$ and $k \in \{0, \pm\pi/M, \pm2\pi/M, \dots, \pi\}$. For the following discussion, let us assume this situation, although different transformations also occur, e.g. when using different boundary conditions.

Single electron excitation We create a single electron excitation upon the ground state. The simplest case would be to create an excitation using one of the diagonal operators defined by U^0 . Within our example, we take momentum k_0 (only a right or left mover) with $k_0 \in \{0, \pm\pi/M, \pm2\pi/M, \dots, \pi\}$

$$f_{k_0}^\dagger = \frac{1}{\sqrt{M}} \sum_{x=1}^M e^{ik_0 x} c_x^\dagger \quad (2.19)$$

However, creating a state $f_{k_0}^\dagger |\Psi\rangle$ would be another eigenstate of the system and thus static in time evolution. On the other hand, using a local operator c_x^\dagger , the resulting excited state $c_x^\dagger |\Psi\rangle$ cannot be associated with a definite momentum k .

Therefore, let us create one electron using several single level creation operators with momenta k , which are Gaussian centred around a single momentum k_0 . For convenience, we will enumerate the single particle levels $l \in \{0, 1, \dots, M-1\}$. This maps linearly enumerated levels to momenta by $k = \frac{2\pi}{M}(1 - M/2 + l)$, such that the occupied levels are within $(M-N)/2 \leq l < (M+N)/2$. Now we can define the Gaussian wave packet with the operator

$$g^\dagger(k_0) = \sum_l f_l^\dagger e^{-\frac{(l-l_0)^2}{2\sigma^2}} = \sum_{x=1}^M \left(e^{(-2\sigma^2\pi^2 x^2)} \right) \left(e^{\frac{2\pi i x}{M}(1-M/2+l_0)} \right) c_x^\dagger, \quad (2.20)$$

which we will define in matrix and vector notation

$$g^\dagger(k_0) = \mathbf{u}^g \mathbf{c}^\dagger = \mathbf{u}^g (\mathbf{d}^\dagger U^{0\dagger}) \quad (2.21)$$

We still have the freedom in the sum to shift the Gaussian packet to be centred in real space about x_0 , which gives up to a normalisation constant C

$$u_x^g = \frac{1}{\sqrt{C}} \left(e^{(-2\sigma^2\pi^2(x-x_0)^2)} \right) \left(e^{\frac{2\pi i x}{M}(1-M/2+l_0)} \right). \quad (2.22)$$

For a tight-binding model the dispersion relation for the single particle states and the

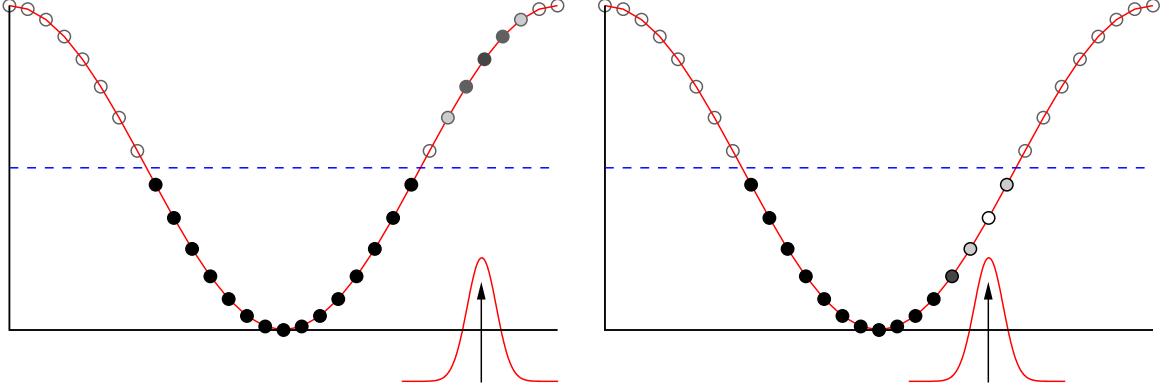


Figure 2.4: Visualisation of the creation of an electron (left) or a hole (right) by indicating the occupation of single particle levels in the dispersion relation of the non-interacting problem. The dashed line represents the Fermi energy.

creation of an excited state using a Gaussian distribution of levels is depicted in figure 2.4.

Excited state We will call the excited state with one additional electron $|\Psi^{+1}\rangle$. With the definition of the transformation matrix U^0 and the vector \mathbf{u}^g and observing that $d_l^\dagger |\Psi\rangle = \Theta(p_F - l) d_l^\dagger |\Psi\rangle$ at zero temperature, we have

$$|\Psi^{+1}\rangle = g^\dagger(k_0) |\Psi\rangle = \sum_{l>p_F} \sum_{x=1}^M u_x^g d_l^\dagger U_{lx}^{0\dagger} |\Psi\rangle \equiv \sum_{l>p_F} d_l^\dagger B_l(k_0) |\Psi\rangle \quad (2.23)$$

with $B_l(k_0) = \sum_x U_{lx}^{0\dagger} u_x^g$. We normalise the state by $\langle \Psi^{+1} | \Psi^{+1} \rangle = \sum_{l>p_F} |B_l(k_0)|^2$, which normalises u^g with $C = \sum_x |u_x^g|^2$.

Real-space density The $t = 0$ local fermion density of the excitation results by plugging in all transformations to

$$n(x) = \langle \Psi^{+1} | c_x^\dagger c_x | \Psi^{+1} \rangle = \left(\sum_{l>p_F} |B_l(k_0)|^2 \right) \left(\sum_{m \leq p_F} |U_{xm}^0|^2 \right) + \left| \sum_{l>p_F} U_{xl}^0 B_l(k_0) \right|^2. \quad (2.24)$$

Note that the creation of a hole state $|\Psi^{-1}\rangle$ is completely analogous, with only the inequality signs swapped.

Time evolution

The time evolution will be defined with operators as in the case of a Gaussian perturbation. The only difference is that here the dynamics does not result from turning off a perturbation at $t > 0$, but starting from an excited system. Note that $|\Psi^{+1}\rangle$ was created using eigenstates of the Hamiltonian, which are on its own static in time evolution. The dynamics results solely from the different phases of the single particle states given by the different weights to form the wave packet.

We define again $A = e^{-iH_0 t}$ and transform the operators as, e.g. $\mathbf{d}^\dagger = \mathbf{t}^\dagger A^\dagger$ and in the diagonal basis of H_0 we have again $t_a^\dagger = \sum_l d_l^\dagger [e^{-iH_0 t}]_{la}$. The new many particle state at time $t > 0$ is constructed from the time evolved single particle states including the time evolved excitation $g^\dagger(k_0)$:

$$|\Psi^{+1}(t)\rangle \equiv \sum_{l>p_F} t_l^\dagger B_l(k_0) |\Psi(t)\rangle = \sum_{l>p_F} t_l^\dagger B_l(k_0) \prod_{p \leq p_F} t_p^\dagger |0\rangle \quad (2.25)$$

Now the local density evolves as

$$\begin{aligned} n(x, t) &= \langle \Psi^{+1}(t) | c_x^\dagger c_x | \Psi^{+1}(t) \rangle \\ &= \sum_{p,q} U_{px}^{0\dagger} U_{xq}^0 \langle \Psi^{+1}(t) | d_p^\dagger d_q | \Psi^{+1}(t) \rangle \\ &= \sum_{m,n} \left(\sum_p A_{mp}^\dagger U_{px}^{0\dagger} \right) \left(\sum_q U_{xq}^0 A_{qn} \right) \langle \Psi^{+1}(t) | t_m^\dagger t_n | \Psi^{+1}(t) \rangle \\ &= \sum_{m,n} V_{mx}^\dagger V_{xn} \sum_{l>p_F} \sum_{l'>p_F} B_l(k_0) B_{l'}(k_0) \langle \Psi(t) | t_l t_m^\dagger t_n t_{l'}^\dagger | \Psi(t) \rangle \\ &= \left(\sum_{l>p_F} |B_l(k_0)|^2 \right) \left(\sum_{m \leq p_F} |V_{xm}|^2 \right) + \left| \sum_{l>p_F} V_{xl} B_l(k_0) \right|^2, \end{aligned}$$

where we have used the intermediate matrices

$$V_{mx}^\dagger = \sum_p A_{mp}^\dagger U_{px}^{0\dagger} \quad \text{and} \quad B_l(k_0) = \sum_x U_{lx}^{0\dagger} u_x^g(k_0) \quad (2.26)$$

and used the fact that in the second last equation the zero temperature expectation value resolves to

$$\begin{aligned} \langle \Psi(t) | t_l t_m^\dagger t_n t_{l'}^\dagger | \Psi(t) \rangle &= \delta_{l,l'} \Theta(l - (p_F + 1)) \delta_{m,n} \Theta(p_F - m) \\ &\quad + \delta_{l',n} \Theta(l' - (p_F + 1)) \delta_{l,m} \Theta(l - (p_F + 1)). \end{aligned} \quad (2.27)$$

In the derivation we assumed to have no degeneracy of the ground state, which can be arranged by the proper choice of boundary conditions.

Generalisation and implementation The above derivation can be implemented for arbitrary shapes of the excitation and arbitrary Hamiltonians. However, one has to be able to

- diagonalise the Hamiltonian to find U^0 ,
- define a useful combination of operators as an excitation to find B_l , e.g. define \mathbf{u} in the real space basis,
- and calculate the matrix exponential in the diagonal basis of the Hamiltonian $e^{-iH_0t} = \sum_{k,l} [A^{(p)}]_{kl} d_k^\dagger d_l$ to find V .

Also, a generalisation to finite temperatures would be straight forward, however, an efficient algorithm within the DMRG framework for small finite temperatures is still lacking.

Real-time simulations As in the case of a Gaussian potential distortion, we simulate non-interacting, small system using as background knowledge for comparison with the interacting cases calculated with the DMRG later. The major differences to a Gaussian potential excitation are that the density $\langle \Psi^{+1} | n | \Psi^{+1} \rangle$ displays a Gaussian peak on top of the homogeneously filled density (in our examples $\langle \Psi | n | \Psi \rangle = 0.5$ in the half-filled system) and that the average momentum k_0 can be freely chosen above the Fermi surface. This also implies that the resulting wave packet only moves in one direction with a velocity corresponding to this momentum k_0 . In figure 2.5 a density peak of

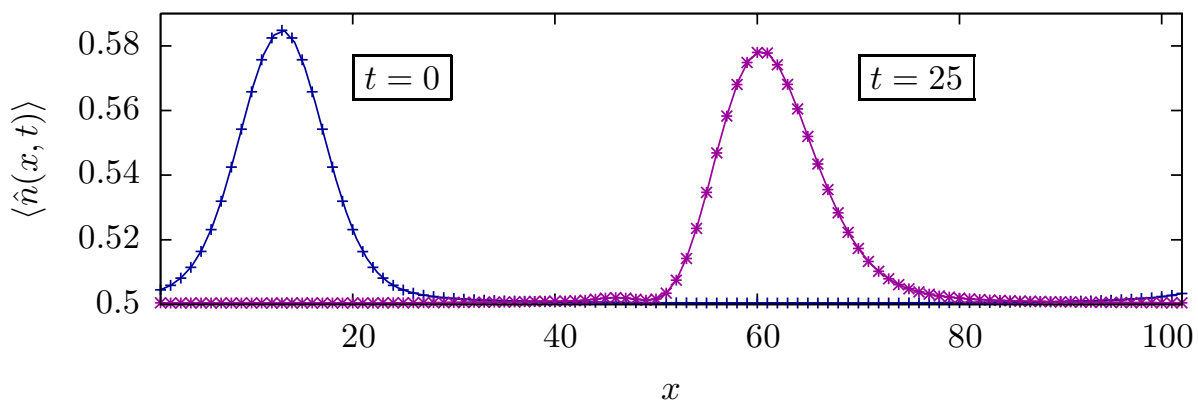


Figure 2.5: Wave packets at initial and a finite time step of a $M = 102$ sized system with width $\sigma_x = 4.0$, with a momentum Gaussian centred around $k_0 = \pi/2 + 0.1$.

width $\sigma_x = 4.0$, centered around $x_0 = 12$ at the beginning has moved to the right. The central momentum in this figure is $k_0 = \pi/2 + 0.1$. Due to the finite width $\sigma \approx 0.04$ of the momentum distribution in reciprocal space, the wave packet has dispersed at the later position. Clearly, an extraction of velocities depends on k_0 directly through the dispersion relation of the single particle states and on the width σ , which smears the ideal δ -like excitation. As can be seen in figure 2.6, instead of a plateau of constant velocity,

a wave packet of one additional electron monotonously increases in velocity over time when measured at the centre of a fitted Gaussian. The main diagram shows the velocity

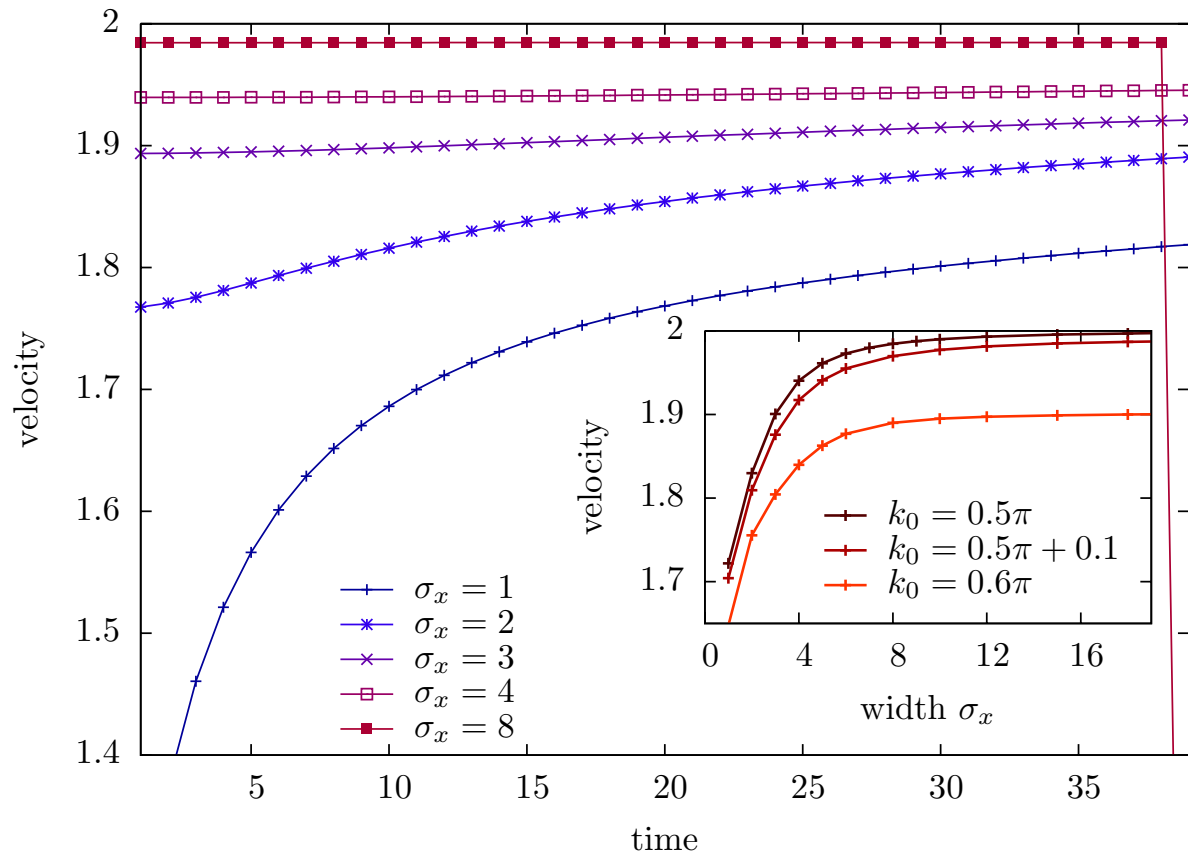


Figure 2.6: Velocities of wave packet of an additional electron with momentum $k_0 = k_F$ on a $M = 102$ lattice with periodic boundary conditions for different widths in real-space σ_x . The inset shows the velocity at $t = 13$ as a function of the width for different momenta of the electron. For widths larger than 10, a system of $M = 302$ sites was used.

development for different widths and accordingly chosen initial positions $x_0 = 3\sigma_x$ on a lattice with $M = 102$ sites, periodic boundary conditions and $k_0 = \pi/2$. While there is almost no irregularity at the start of the simulation, around $t = 25 \approx M/(2v)$ very small oppositely running contributions can interfere with the main peak and degrade a velocity extraction. At this stage, using Gaussian fits at every time step smooths out these irregularities. Since the analytic behaviour of the velocity is unknown in the interacting case, we will choose the velocity at a certain time $t \sim M/(4v)$ and compare it for different widths σ_x and different momenta k_0 . The inset in figure 2.6 shows there is asymptotic behaviour with increasing width. An ideal excitation in an infinite system would have the velocities $v_{k_0} = 2 \sin k_0 = 2.0, \approx 1.990, \approx 1.902$ for excitations with momenta $k_0 = 0.5\pi, 0.5\pi + 0.1, 0.6\pi$.

Note that in finite systems, the distribution of excited levels in momentum space is

cut off by the band edges at $|k| = \pi$ and the Fermi momentum $k = k_F$, since we can only excite unoccupied states above the Fermi points. This implies an inherent skewness of the excitations which has a big influence for small system sizes, e.g. figure 2.6 was calculated for $k_0 = k_F = \pi/2$, but the effect of the skewness is negligible at this system size, at least for the non-interacting system. Again, hard-wall boundary conditions imply Friedel oscillations, which make it much harder to properly extract smooth velocity curves. The result for hard-wall boundary conditions are shown in appendix A.1 and compared to DMRG results, which are used in section 4.4.1.

2.4 Dynamical correlation functions

We define the retarded and advanced Greens function in time domain for the fermionic time dependent operators $A(t)$ and $B(t')$

$$G_{A,B}^r(t, t') = -i\Theta(t - t') \langle \{A(t), B(t')\} \rangle. \quad (2.28)$$

We will assume translational invariance in time and with out loss of generality set $t' = 0$. Furthermore, we will define two helper functions

$$G_{A,B}^+(t) = -i\Theta(t) \langle A(t)B(0) \rangle, \quad (2.29)$$

$$G_{B,A}^-(t) = i\Theta(t) \langle B(0)A(t) \rangle. \quad (2.30)$$

These helper functions differ, beside the minus sign, only in that for G^+ the right operator acts at time $t = 0$, while for G^- the right operator acts at the measurement time t . Now the retarded Greens function can be written as

$$G_{A,B}^r(t) = -i\Theta(t) \langle A(t)B(0) + B(0)A(t) \rangle = G_{A,B}^+(t) - G_{B,A}^-(t). \quad (2.31)$$

Going into frequency domain by Fourier transformation, we derive the helper function $\mathcal{G}_{A,B}^+(\omega)$, using $H|\Psi_0\rangle = E|\Psi_0\rangle$ and the Heisenberg representation of the operator $A(t) = e^{iHt}Ae^{-iHt}$,

$$\begin{aligned} \mathcal{G}_{A,B}^+(\omega) &= \int_{-\infty}^{\infty} dt e^{i\omega t} G_{A,B}^+(t) \\ &= -i \int_0^{\infty} dt e^{i\omega t} \langle \Psi_0 | A(t)B(0) | \Psi_0 \rangle \\ &= -i \int_0^{\infty} dt e^{i\omega t} \langle \Psi_0 | e^{iHt} A e^{-iHt} B | \Psi_0 \rangle \\ &= -i \int_0^{\infty} dt e^{i(\omega+E_0)t} \langle \Psi_0 | A e^{-iHt} B | \Psi_0 \rangle. \end{aligned}$$

Introducing a small imaginary $i\eta$ with $\eta = 0^+$, we have

$$\begin{aligned}
&= -i \int_0^\infty dt \langle \Psi_0 | A e^{i(\omega + E_0 - H + i\eta)t} B | \Psi_0 \rangle \\
&= - \langle \Psi_0 | A \frac{e^{i(\omega + E_0 - H + i\eta)t}}{(\omega + E_0 - H + i\eta)} \Big|_0^\infty B | \Psi_0 \rangle \\
&= \langle \Psi_0 | A \frac{1}{(\omega + E_0 - H + i\eta)} B | \Psi_0 \rangle.
\end{aligned} \tag{2.32}$$

The fraction between the operators A and B is called the *resolvent operator*. Equivalently, with the helper function

$$\begin{aligned}
\mathcal{G}_{B,A}^-(\omega) &= \int_{-\infty}^\infty dt e^{i\omega t} G_{B,A}^-(t) = i \int_0^\infty dt e^{i\omega t} \langle \Psi_0 | B e^{iHt} A e^{-iHt} | \Psi_0 \rangle \\
&= i \int_0^\infty dt e^{i(\omega - E_0 + i\eta)t} \langle \Psi_0 | B e^{iHt} A | \Psi_0 \rangle \\
&= - \langle \Psi_0 | B \frac{1}{(\omega - E_0 + H + i\eta)} A | \Psi_0 \rangle
\end{aligned} \tag{2.33}$$

we find that $\mathcal{G}_{B,A}^-(\omega + i\eta) = \mathcal{G}_{B,A}^+(-\omega - i\eta)$ (dragging the imaginary part $i\eta$ into the argument) and we get the Fourier transformed retarded Greens function

$$\mathcal{G}_{A,B}^r(\omega) = \mathcal{G}_{A,B}^+(\omega) - \mathcal{G}_{B,A}^-(\omega) \tag{2.34}$$

$$\begin{aligned}
&= \langle \Psi_0 | A \frac{1}{(\omega + E_0 - H + i\eta)} B | \Psi_0 \rangle + \langle \Psi_0 | B \frac{1}{(\omega - E_0 + H + i\eta)} A | \Psi_0 \rangle \\
&= \mathcal{G}_{A,B}^+(\omega + i\eta) - \mathcal{G}_{B,A}^+(-\omega - i\eta) \\
&= \langle \Psi_0 | A \frac{1}{(E_0 - H + \omega + i\eta)} B | \Psi_0 \rangle - \langle \Psi_0 | B \frac{1}{(E_0 - H - \omega - i\eta)} A | \Psi_0 \rangle.
\end{aligned} \tag{2.35}$$

Finally, the spectral density function is defined by

$$\mathcal{A}(\omega) = -\frac{1}{\pi} \text{Im}(\mathcal{G}_{A,B}^r(\omega)) \tag{2.36}$$

where $\text{Im}()$ takes the imaginary part of its argument. If $B = c^\dagger$ is a creation and $A = c$ an annihilation operator, the naming of \mathcal{G}^\pm contains a convenient to remember convention: \mathcal{G}^+ is the propagator corresponding to creating a particle (c^\dagger), measuring the response of the system before another one (c) is taken out again. \mathcal{G}^- can be interpreted analogous as the “particle destroyed” response. Note that this convention is not meant in a time-like order as in the definition of $G_{A,B}^r(t, t')$.

We are also interested in the lesser and greater Greens functions, defined by

$$\begin{aligned}
G_{A,B}^>(t) &\equiv -i \langle A(t) B(0) \rangle. \\
G_{B,A}^<(t) &\equiv i \langle B(0) A(t) \rangle
\end{aligned}$$

By analogous Fourier transformation (splitting $\int_{-\infty}^{+\infty} = \int_{-\infty}^0 + \int_0^{+\infty}$) we find

$$\begin{aligned}\mathcal{G}_{B,A}^<(\omega) &= \mathcal{G}_{B,A}^-(\omega) - \mathcal{G}_{B,A}^+(-\omega) \\ &= \mathcal{G}_{B,A}^-(\omega + i\eta) - \mathcal{G}_{B,A}^-(\omega - i\eta)\end{aligned}\quad (2.37)$$

$$\begin{aligned}\mathcal{G}_{A,B}^>(\omega) &= \mathcal{G}_{A,B}^+(\omega) - \mathcal{G}_{A,B}^-(-\omega) \\ &= \mathcal{G}_{A,B}^+(\omega + i\eta) - \mathcal{G}_{A,B}^+(\omega - i\eta)\end{aligned}\quad (2.38)$$

One can see at these expressions that the real part of the lesser and greater Greens function vanish, while the imaginary parts are identical and add up. When defining the lesser and greater spectral functions analogously to be positive quantities, we have

$$\begin{aligned}\pi\mathcal{A}^<(\omega) &\equiv \text{Im}(\mathcal{G}_{B,A}^<(\omega + i\eta)) = 2\text{Im}(\mathcal{G}_{B,A}^-(\omega + i\eta)) \\ -\pi\mathcal{A}^>(\omega) &\equiv \text{Im}(\mathcal{G}_{A,B}^>(\omega + i\eta)) = 2\text{Im}(\mathcal{G}_{A,B}^+(\omega + i\eta)).\end{aligned}\quad (2.39)$$

and finally from (2.36) and (2.34), we find

$$\mathcal{A}(\omega) = \frac{1}{2}(\mathcal{A}^>(\omega) + \mathcal{A}^<(\omega)).$$

Indeed $\mathcal{A}^<(\omega)$ is the response below the Fermi surface, since it is proportional to the removal of a particle with annihilation operator A and $\mathcal{A}^>(\omega)$ is the response from above the Fermi surface, since it is proportional to the addition of a particle. We will use this definition to determine the Fermi surface in interacting many-body ground states.

Example: free fermions

Take $A = c_x$ and $B = c_y^\dagger$, the annihilation and creation operators of a spinless fermion at position x and y in a lattice. The single particle Greens function now reads

$$\mathcal{G}_{c_x, c_y^\dagger}^r(\omega) = \langle \Psi_0 | c_x \frac{1}{(\omega + E_0 - H + i\eta)} c_y^\dagger | \Psi_0 \rangle - \langle \Psi_0 | c_y^\dagger \frac{1}{(\omega - E_0 + H + i\eta)} c_x | \Psi_0 \rangle \quad (2.40)$$

We can diagonalise free fermion Hamiltonian with $U^\dagger H U = \text{diag}$, where the operators transform into the diagonal basis $\{|d\rangle\}$

$$\mathbf{c} = U\mathbf{d}, \quad \mathbf{d} = U^\dagger\mathbf{c}, \quad \mathbf{c}^\dagger = \mathbf{d}^\dagger U^\dagger, \quad \mathbf{d}^\dagger = \mathbf{c}^\dagger U. \quad (2.41)$$

Within the diagonal basis the Hamiltonian in the resolvent of the Greens function can be replaced by its eigenvalues $Hd_l^\dagger |\Psi\rangle = (E_0 + \varepsilon_l) |\Psi\rangle$. For the helper function \mathcal{G}^+ , we

have

$$\begin{aligned}
\mathcal{G}_{c_x, c_y^\dagger}^+(\omega) &= \langle \Psi_0 | c_x \frac{1}{(\omega + E_0 - H + i\eta)} c_y^\dagger | \Psi_0 \rangle \\
&= \sum_{k,l} \langle \Psi_0 | d_k \frac{U_{xk} U_{ly}^\dagger}{(\omega + E_0 - (E_0 + \varepsilon_l) + i\eta)} d_l^\dagger | \Psi_0 \rangle \\
&= \sum_{k,l} (\delta_{l,k} - \langle \Psi_0 | d_l^\dagger d_k | \Psi_0 \rangle) \times \frac{U_{xk} U_{ly}^\dagger}{(\omega - \varepsilon_l + i\eta)} \\
&= \sum_l (1 - \langle \Psi_0 | d_l^\dagger d_l | \Psi_0 \rangle) \times \frac{U_{xl} U_{yl}^*}{(\omega - \varepsilon_l + i\eta)} \tag{2.42}
\end{aligned}$$

For the other helper function, we have, similarly,

$$\begin{aligned}
\mathcal{G}_{c_y^\dagger, c_x}^-(\omega) &= -\langle \Psi_0 | c_y^\dagger \frac{1}{(\omega - E_0 + H + i\eta)} c_x | \Psi_0 \rangle \\
&= -\sum_{k,l} \langle \Psi_0 | d_l^\dagger \frac{U_{ly}^\dagger U_{xk}}{(\omega - E_0 + (E_0 - \varepsilon_l) + i\eta)} d_k | \Psi_0 \rangle \\
&= -\sum_l \langle \Psi_0 | d_l^\dagger d_l | \Psi_0 \rangle \times \frac{U_{xl} U_{yl}^*}{(\omega - \varepsilon_l + i\eta)}. \tag{2.43}
\end{aligned}$$

Our interpretation of the helper Greens function \mathcal{G}^+ is expressed by the weight $(1 - \langle \hat{n}_l \rangle)$, allowing only states above the Fermi surface to contribute to the sum, while the prefactor $\langle \hat{n}_l \rangle$ allows only states below the Fermi surface to contribute to \mathcal{G}^- . The retarded Greens function adds up to

$$\mathcal{G}_{c_x, c_y^\dagger}^r(\omega) = \sum_l \frac{U_{xl} U_{yl}^*}{(\omega - \varepsilon_l + i\eta)} \tag{2.44}$$

This gives us the real-space spectral function $\mathcal{A}(x, y, \omega)$. To get the momentum-resolved spectral function, one further Fourier transformation is necessary

$$\mathcal{A}(k, \omega) = -\frac{1}{\pi} \text{Im} \left(\frac{1}{\sqrt{M}} \int dx e^{-ikx} \mathcal{G}_{c_x, c_y^\dagger}^r(\omega) \right). \tag{2.45}$$

Bloch states However, for the free fermion system, we can also work directly with momentum operators, like the Bloch states on a ring. Let us use the operators, in which the Hamiltonian is diagonal $\{|d\rangle\}$. The corresponding Greens function relaxes to the free fermion propagator

$$\mathcal{G}_{d_k, d_k^\dagger}^r(\omega) = \frac{1}{(\omega - \varepsilon_k + i\eta)}, \tag{2.46}$$

whose spectral function is a Lorentz function with width η centred around ε_k

$$\mathcal{A}(k, \omega) = -\frac{1}{\pi} \text{Im}(\mathcal{G}_{d_k, d_k^\dagger}^r(\omega)) = \frac{1}{\pi} \frac{\eta}{(\omega - \varepsilon_k)^2 + \eta^2}, \tag{2.47}$$

which is correctly always positive. Accordingly, the lesser and greater spectral functions are the spectral function dressed by the weights given by the occupation of states above $1 - \langle n_k \rangle$ and below $\langle n_k \rangle$ the Fermi surface.

Usually, the single particle spectral function in the Lehmann representation is defined by

$$\mathcal{A}(k, \omega) = \sum_f \left| \langle f, N+1 | c_k^\dagger | 0, N \rangle \right|^2 \delta(\omega - E_0^N + E_f^{N+1}), \quad (2.48)$$

where f denotes the final states, the system can be in. This definition is equivalent to (2.47) for $\eta \rightarrow 0$.

Free fermions and general operators The Greens function for a general operator, which can be expressed in terms of local operators involves another transformation. Let us label the operators with m and their representation in real space be $g_m^\dagger = \sum_x c_x^\dagger V_{xm}$, which defines the transformation V , in matrix notation

$$\mathbf{c} = V\mathbf{g}, \quad \mathbf{g} = V^\dagger\mathbf{c}, \quad \mathbf{c}^\dagger = \mathbf{g}^\dagger V^\dagger, \quad \mathbf{g}^\dagger = \mathbf{c}^\dagger V. \quad (2.49)$$

Then

$$\begin{aligned} \mathcal{G}_{g_n, g_m^\dagger}^r(\omega) &= \mathcal{G}_{g_n, g_m^\dagger}^+(\omega) - \mathcal{G}_{g_m^\dagger, g_n}^-(\omega) \\ &= \langle \Psi_0 | \sum_x V_{nx}^\dagger c_x \frac{1}{(\omega + E_0 - H + i\eta)} \sum_y c_y^\dagger V_{ym} | \Psi_0 \rangle - \mathcal{G}^- \\ &= \sum_{x,y} V_{nx}^\dagger V_{ym} \sum_l (1 - \langle \Psi_0 | d_l^\dagger d_l | \Psi_0 \rangle) \times \frac{U_{xl} U_{yl}^*}{(\omega - \varepsilon_l + i\eta)} \\ &\quad + \sum_{x,y} V_{ym} V_{nx}^\dagger \sum_l \langle \Psi_0 | d_l^\dagger d_l | \Psi_0 \rangle \times \frac{U_{xl} U_{yl}^*}{(\omega - \varepsilon_l + i\eta)} \\ &= \sum_l \frac{(\sum_x [V^\dagger]_{nx} U_{xl}) (\sum_y [U^\dagger]_{ly} V_{ym})}{(\omega - \varepsilon_l + i\eta)} \\ &= \sum_l \frac{[V^\dagger U]_{nl} [U^\dagger V]_{lm}}{(\omega - \varepsilon_l + i\eta)} = \sum_l \frac{[U^\dagger V]_{ln}^* [U^\dagger V]_{lm}}{(\omega - \varepsilon_l + i\eta)} \end{aligned} \quad (2.50)$$

and for the case, when $n = m$, we have

$$\mathcal{G}_{g_m, g_m^\dagger}^r(\omega) = \sum_l \frac{|[U^\dagger V]_{lm}|^2}{(\omega - \varepsilon_l + i\eta)}. \quad (2.51)$$

This allows us to choose operators, e.g. $g_m \sim \sum_x \sin(mx) c_x$, where m is in a sense a crystal momentum, even if the underlying model does not obey translational symmetry and the diagonal operators d do not define a crystal momentum.

Finite size effects

Due to finite lattices, the limit of the broadening $\lim_{\eta \rightarrow 0^+} \mathcal{A}(k, \omega)$ can not be achieved. Rather, η has to be larger than the smallest level splitting or the finite size structure can be seen in the spectral response. Dyson's equation for the fully interacting retarded propagator \mathcal{G}^r derived from the bare propagator $\mathcal{G}^{r,0}$ defines the self-energy $\Sigma(k, \omega)$ via

$$\mathcal{G}^r = \mathcal{G}^{r,0} + \mathcal{G}^{r,0} \Sigma \mathcal{G}^r = \frac{1}{(\mathcal{G}^{r,0})^{-1} - \Sigma} \quad (2.52)$$

$$= \frac{1}{\omega - (H - E_0) + i0^+ - \Sigma} = \frac{1}{\omega - (H - E_0) - \Sigma' + i(0^+ - \Sigma'')} \quad (2.53)$$

$$= \frac{\omega - (H - E_0) - \Sigma'}{(\omega - (H - E_0) - \Sigma')^2 - (0^+ - \Sigma'')^2} - \frac{i(0^+ - \Sigma'')}{(\omega - (H - E_0) - \Sigma')^2 - (0^+ - \Sigma'')^2} \quad (2.54)$$

Thus, for an interacting system the imaginary part of the self-energy, Σ'' , gives a broadening in addition 0^+ to the spectral function $\text{Im}\mathcal{G}$, while Σ' only shifts the energy. In the continuum limit 0^+ is sent to zero. For our finite systems, the η remains finite, but one can extract the $\eta \rightarrow 0$ limit. One way is to see that the imaginary part in (2.54) is a convolution of the continuum limit with a Lorentz-function of width η and thus a numerical deconvolution of the data is possible. However, this turns out to be numerically unstable.

Manual deconvolution A more straight forward possibility is to subtract η from the inverse of the Greens function. If we denote the data we get from the numerical calculation with a finite width η with $\mathcal{D} = (\omega - (H - E_0) + i(0^+ + \eta) - \Sigma)^{-1}$ and we aim for \mathcal{G} (dropping the index r), we see from Dyson's equation (2.52) that

$$[\mathcal{G}^{-1}] = [\mathcal{D}^{-1}] - i\eta = \frac{\mathcal{D}'}{|\mathcal{D}|^2} + i \left(\frac{-\mathcal{D}''}{|\mathcal{D}|^2} - \eta \right) \quad (2.55)$$

and

$$\mathcal{G} = \frac{[\mathcal{G}^{-1}]' - i[\mathcal{G}^{-1}]''}{|\mathcal{G}^{-1}|^2} = \frac{\mathcal{D}' + i(\mathcal{D}'' + \eta|\mathcal{D}|^2)}{1 + 2\eta\mathcal{D}'' + \eta^2|\mathcal{D}|^2} \quad (2.56)$$

Since for non-interacting particles the self-energy is zero, $\text{Im}\mathcal{G}^r$ becomes a delta-function. This shows that we can manually deconvolute the data from the Lorentz distribution of width η . To avoid a numerical divergence at the resonance frequency, it makes sense in above procedure to fine-tune the subtracted η and subtract only $(\eta - \eta_{\text{res}})$, especially if the data is near the non-interacting delta-function limit.

2.5 Summary

In this chapter we have exactly derived the time evolution of a perturbation in a spinless fermionic tight-binding chain. Using an exact diagonalisation simulation, we tracked

a density peak formed by a Gaussian excitation in finite systems. We showed how an extracted excitation velocity depends on the width of the initial perturbation and not so much on the system size itself as long as the systems are large compared to the width. The results can be used as a benchmark and for comparison with interacting systems.

Further, we derived the equations for the time evolution of a density excitation, which is caused by an addition or removal of an electron put into the many particle ground state. Analogous to the perturbation, we used exact numerics to show, how real-time variables like the excitation velocity depend on the width and momentum of the injected electron and how small system sizes hamper the analysis.

Finally, we presented the Greens functions that are needed to calculate the spectral function of an electron addition or removal. By writing down explicit expression for a single particle problem, we emphasised the influence of finite systems introducing a non-vanishing broadening η . The broadening can be subtracted from the data using a simpler transformation than a numerically unstable deconvolution, if both real and imaginary part of the Greens function are known.

3 Methods: Simulation

```
Marvin: ‘‘I’ve been talking to the main computer.’’  
Arthur: ‘‘And?’’  
Marvin: ‘‘It hates me.’’  
(Marvin the Paranoid Android and Arthur Dent in The  
Hitchhiker’s Guide to the Galaxy, Douglas Adams)
```

In this chapter we will introduce and motivate the numerical method we use. Since there are already several useful and recent reviews on the subject [5, 6, 7, 8], this chapter will not exhaustively cover all details of the DMRG approach, rather we will try to pedagogically introduce the basic algorithm and the extensions necessary for our calculations.

We are investigating quantum many-body problems. The simplest problems in condensed matter physics are the ones where the problem reduces to a single particle problem or can be described by an effective single particle description as in the Fermi liquid theory. Among others, strong correlation between the particles under investigation usually prohibits this reduction and the full quantum many-body problem has to be solved. Since some of these problems are not fully solvable by analytical means, numerical approaches are justified. However, even numerical simulation quickly meet limitations. The obvious first choice is the exact diagonalisation of the problem.

3.1 Exact diagonalisation

We consider a real-space lattice model of M sites, where each site j can be described by a finite number d of basis states $\{|\alpha_j^d\rangle\}$. We will later look at interacting electrons, where the basis states allowed by the Pauli principle are: empty $|0\rangle$, occupied by either spin orientation $|\uparrow\rangle, |\downarrow\rangle$ or double occupation $|\uparrow\downarrow\rangle$. All combinations of the direct product of such basis states for each site compound a basis for the full system with M lattice sites. Any state can be expressed in that basis,

$$|\Psi\rangle = \sum_{\{\alpha_j^d\}} f(\alpha_1^d, \dots, \alpha_M^d) |\alpha_1^d\rangle \otimes \dots \otimes |\alpha_M^d\rangle. \quad (3.1)$$

Solving the time-independent Schrödinger equation $H|\Psi\rangle = E|\Psi\rangle$ means solving the eigenvalue equation of the Hamiltonian H , which is a matrix in the site-basis representation above with $d^M \times d^M$ entries. This size exponentially increases with system size M , which is the key limitation in computing resources. For comparison, a usual desktop computer of 2009 with a memory of 4 GB = $4 * 2^{30}$ bytes can only hold one vector of (3.1) $|\Psi\rangle$ of a system with $M = 30$ lattice sites, when $d = 2$ (e.g. spinless particles).

In the worst case problem, the Hamiltonian matrix H is full, i.e. all entries are non-zero and one is restricted to small system sizes. However, if the system obeys symmetries, one can write H in a block diagonal structure, grouped by the conserved quantity that correspond to the symmetry. Typical examples are particle number conservation, spin symmetries or lattice symmetries. Each block can then be diagonalised within its own subspace.

Beside the symmetries, entries of the Hamiltonian matrix might be already zero by construction, because the basis states do not get entangled by H , e.g. if there is no hopping between all the sites. This allows for the usage of more efficient diagonalisation techniques, which are adapted to the shape of the matrix, e.g. hermitian matrices, sparse matrices, tridiagonal matrices etc. In the simplest example of non-interacting spinless fermions ($l = 2$) with only nearest neighbour hopping (tight-binding model) and hard-wall boundary conditions, the matrix does not need to be written in the many-body basis and is tridiagonal in the single particle basis.

Iterative algorithms In the up-coming DMRG framework, only a small number of the smallest eigenvalues of H are needed. In this case, there exist specialised iterative algorithms which can then handle larger systems. The two most common algorithms for an iterative solution of the eigenvalue problem should be mentioned. The **Lanczos method** iteratively builds up the *Krylov subspace* onto which the Hamiltonian is projected. The feature is that the smallest (and the largest) eigenvalues converge faster than others, such that the dimension of the subspace is a lot smaller than the original Hilbert space. Within the subspace the Hamiltonian becomes tridiagonal and can be diagonalised quickly. The **Jacobi-Davidson** algorithm similarly features the fastest convergence of the extremal eigenvalues in a linearly growing subspace. Depending on the problem, it converges faster and is more stable than the Lanczos procedure, but has a higher memory footprint. Both algorithms are well described in Ref. [5, 6].

Non-interacting particles In the models we use, the non-interacting system is usually the tight-binding model of spinless fermions. In that case, the Hamiltonian matrix in the single particle picture is only of size $M \times M$. Thus, the problem scales only with some power (M^2 for the matrix size and at most M^3 for the diagonalisation) and we used higher level numerical tools (`octave`, `python + numpy`) or own implementations in `C/C++`, which all use standard linear algebra subroutine implementations (BLAS) for solving the eigenvalue problem.

3.2 The Density Matrix Renormalisation Group

The exponential growth of the size of the Hilbert space with system size M limits exact diagonalisation routines for strongly correlated systems to small system sizes. The only way to proceed is to *truncate* the Hilbert space in some way.

One example: the Numerical Renormalisation Group (NRG) method keeps the size of the Hilbert space constant by using only the N_{cut} smallest eigenvalues and -vectors of the Hamiltonian in its procedure (see [5] for an introduction). Even though the Hilbert space is hugely restricted, the single-impurity Kondo problem was solved by Wilson [9] using this method (especially, due to the clever choice of a logarithmic discretization).

In contrast, in the Density Matrix Renormalisation Group (DMRG) one chooses to truncate the Hilbert space by the N_{cut} highest eigenvalues of the density matrix of the system and uses the corresponding eigenstates as a basis. It turns out that this choice of basis states is *optimal* for a representation of the ground state wave function.

Our approach is to give a short overview that explains the basic algorithm, followed by answering naturally arising questions how the procedure can be extended and errors are controlled. The following sections 3.3 and 3.4 are then simply extensions to this framework. For many optimisation and further extensions, we refer to the reviews.

3.2.1 Infinite lattice algorithm

We outline how the density matrix is constructed, how the truncation of the Hilbert space is performed and how the optimal basis for the ground state is thereby obtained. All of this is embedded in a standard blocking scheme procedure, which iteratively builds up a system in real-space. While the true Hilbert space of this procedure is exponentially growing, the optimised truncated Hilbert space stays manageably small.

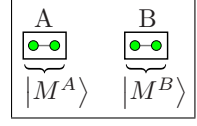
DMRG in words Before sketching the DMRG algorithm, which can be found in any of the mentioned reviews, we find it useful to compress the basic (infinite lattice) algorithm loop in a minimal verbal version.

... we add the degrees of freedom d of one site σ to a system A with m basis states $\{|m\rangle\}$, embedded in a larger (known) system B . The aim is to find the global ground state defined over $A + \sigma + B$, which we find by a Lanczos procedure, but sustainability¹ requires us to get rid of the gained factor of d states. When we ask: What are the best m basis states within $A + \sigma$ to describe the local part of the global ground state? It turns out to be those m basis states with the highest weight in the reduced density matrix, formed in the local basis with B as a statistical bath. Now set $A = A + \sigma$ and ...

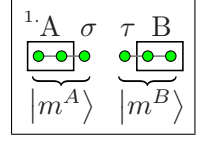
¹We may lend this term from environmental science and socio-economics, meaning not to be able to exceed limiting resources.

DMRG: Infinite lattice algorithm

Initially, we set up block A with $l = a_0$ sites. Since each site-basis is d -dimensional, the product basis $\{|M^A\rangle\}$ of all l sites is $(d)^l$ -dimensional. Analogously, we set up a block B, creating the product basis $\{|M^B\rangle\}$.



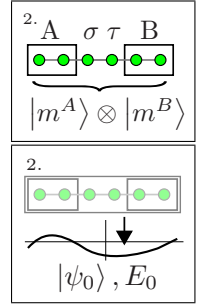
Step 1. To the block A of length l we add one new site by constructing a new basis with the d_σ -dimensional local site-basis $\{|\sigma\rangle\}$, which we call $\{|m^A\rangle\} = \{|M^A\rangle\} \otimes \{|\sigma\rangle\}$. This basis' dimension is $m^A = M^A \cdot d_\sigma$. The Hamilton operator on block $A + \sigma$: $\hat{H}^{A+\sigma}$ is a matrix of dimension $m^A \times m^A$. Analogously, we add to block B of length l the site τ and create a new basis with $\dim \{|m^B\rangle\} = M^B \cdot d_\tau$.



Step 2. We form a superblock of length $L = 2l + 2$ by joining blocks $A + \sigma$ and $\tau + B$,

$$\begin{aligned} \{|D\rangle\} &= \{|M^A\rangle\} \otimes \{|\sigma\rangle\} \otimes \{|\tau\rangle\} \otimes \{|M^B\rangle\} \\ \dim \{|D\rangle\} &= M^A \cdot d_\sigma \cdot d_\tau \cdot M^B = D \end{aligned}$$

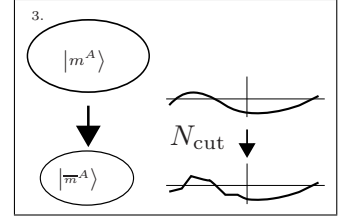
The full Hamiltonian of the superblock \hat{H}_L is a $D \times D$ sized matrix and its smallest eigenvalues are determined using the Lanczos or Davidson algorithm. This leads to the ground state via $\hat{H}_L |\psi_0\rangle = E_0 |\psi_0\rangle$. The ground state has the representation



$$|\psi_0\rangle = \sum_{i=1}^{m^A} \sum_{j=1}^{m^B} c_{ij} |m_i^A\rangle \otimes |m_j^B\rangle$$

Step 3. Instead of the full density matrix $\rho = |\psi_0\rangle \langle \psi_0|$, we form the *reduced density matrix* of block $A + \sigma$ by tracing over all states of the $B + \tau$ block

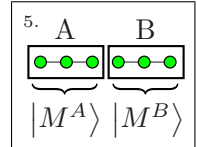
$$\rho^{A+\sigma} = \text{Tr} [\rho]_{B+\tau} = \sum_j \sum_{i,i'} c_{ij} c_{i'j}^* |m_i^A\rangle \langle m_{i'}^A|.$$



This matrix is of size $m^A \times m^A$. We fully diagonalise $\rho^{A+\sigma}$ and keep the $\bar{m}^A = N_{\text{cut}}$ highest eigenvalues and the corresponding eigenvectors $\{|\bar{m}^A\rangle\}$, which form the $(m^A \times \bar{m}^A)$ sized transformation matrix U .

Analogously, the block $A + \sigma$ is traced out for $\rho^{B+\tau}$, which is diagonalised keeping also N_{cut} DMRG states.

Step 4. Now we transform the Hamiltonian on block $A + \sigma$ to this new basis $\hat{H}^{\bar{m}^A} = U^\dagger \hat{H}^{A+\sigma} U$ and on block $B + \tau$ respectively using the corresponding transformation matrix.



Step 5. Finally, we set $\{|M^A\rangle\} = \{|\bar{m}^A\rangle\}$ (so that $M^A = \bar{m}^A$), $\{|M^B\rangle\} = \{|\bar{m}^B\rangle\}$, set $l = l + 1$, view block $A + \sigma$ as the new block A and $B + \tau$ as the new block B. Now one “DMRG step” is finished and we continue with step 1.

Numerical effort The most time-consuming computation is in the iterative diagonalisation of the superblock Hamiltonian in step 2. However, symmetries obeyed by the superblock Hamiltonian H_L can be used to simplify the book-keeping and to choose only the necessary calculations. For example, given particle number conservation in the Hamiltonian and given a fixed number of N particles in the system, we only need to search for the ground state of \hat{H}_L within those product states $\{|m^A\rangle\} \otimes \{|m^B\rangle\}$ which are restricted to N total particles.

Furthermore, the reduced density matrix becomes block-diagonal and these internal blocks are labelled by the conserved quantity. Thus, the dense ($m^A \times m^A$) diagonalisation simplifies to several smaller matrix sizes, provided the book-keeping of which basis state maps to which quantum number is ensured during the cutoff procedure in step 3. Following above example, the density matrix for block $A + \sigma$ decomposes into internal blocks of with particle number $N_i = 0, 1, 2, 3, \dots, N$. Each internal block N_i is constructed from those basis states $|m_i^A\rangle, |\bar{m}_i^A\rangle$, which carry all exactly N_i particles. Of the then newly diagonalised basis states $|\bar{m}_i^A\rangle$, the corresponding particle number has to be remembered, when after truncating only N_{cut} of *all* basis states are selected.

Whenever we truncate in our numerics to “ N_{cut} DMRG states”, this means, the number of basis states kept when summed over all internal density matrix blocks will not exceed N_{cut} .

There are several more standard optimisations to be considered for an implementation, which we will not elaborate on here [5].

Observables At the end of step 2, the ground state $|\psi_0\rangle$ is available. A physical observable can now be measured as the expectation value in the ground state. Therefore, a local operator, e.g. the local particle density $c_y^\dagger c_y$ should be expressed in the correct basis. If the added site σ is at position y , the local density operator can immediately be formed in the basis of the block $A + \sigma$, $\langle m^A | \hat{n}(y) | m^A \rangle$. However, at step 4 the basis transformation $|m^A\rangle \rightarrow |\bar{m}^A\rangle$ has to be done for all operators, such that a measurement can be done at any DMRG step. Operators on different sites (for equal-time correlation functions) have to be treated with more care and require a better book-keeping, but can be evaluated just as well.

All other observables, like time-, energy- or momentum-dependent correlation functions or temperature dependent quantities are possible to evaluate in principle within the DMRG framework. They require extensions or reformulations of the DMRG procedure and will not be presented here [5, 7], except for the time evolution and the dynamical correlation function approach.

Optimally projected Hilbert space It can be argued [8] that choosing to reduce and project the Hilbert space by the N_{cut} most important eigenstates of the density matrix is an “optimal [approximation] in the sense of a least-squares minimisation of the differences between the exact $|\Psi\rangle$ and the approximate one” ([5, 10]). Less formally, one understands that the eigenstates of the density matrix, formed by the ground state are the *weight* for the system to be in the corresponding eigenstate. Therefore, using these

eigenstates as a basis to express the ground state (and expectation values in the ground state) ought to be a good approximation.

As will be essential in the time evolution algorithm, one can form a density matrix of a mixed state, if one wants to optimise the Hilbert space for more than one state simultaneously. In general, the mixed ensemble density matrix is composed of a sum of states,

$$\rho = \sum_{\alpha} |\Psi_{\alpha}\rangle \langle \Psi_{\alpha}|. \quad (3.2)$$

For example, if the time evolution requires the state $|\Psi(t_i)\rangle$ at time t_i , then the appropriate density matrix will be $\rho = |\psi_0\rangle \langle \psi_0| + |\Psi(t_i)\rangle \langle \Psi(t_i)|$. Of course, the accuracy or the rate of convergence to the individual state will suffer and it might be necessary to increase N_{cut} , but it also enables us to calculate non-ground state expectation values of observables.

Truncation error In step 4 of the procedure, the $\overline{m}^A = N_{\text{cut}}$ highest eigenvalues of the reduced density matrix $\rho^{A+\sigma}$ are kept, while $(m^A - \overline{m}^A)$ eigenvalues and -states are discarded at this truncation. If we label the ordered eigenvalues (weights) w_{α} , the sum over all weights, the *discarded weight*

$$\varepsilon_{\text{disc}} = \sum_{\overline{m}^A}^{m^A} w_{\alpha} \quad (3.3)$$

is a measure for the error of the truncation. If the weight distribution falls off quickly with increasing α , DMRG is a very good approximation. In the worst case, all weights are equal ($\frac{1}{m^A}$). This represents a maximally entangled state and the DMRG truncation scheme is useless.

Another commonly defined measure of the error of the truncation procedure is the discarded entropy, defined by

$$S_{\text{disc}} = - \sum_{\overline{m}^A}^{m^A} w_{\alpha} \log w_{\alpha} \quad (3.4)$$

The complete truncation error involves the error of the discarded weights of block $A + \sigma$, but also the error made by having only a finite environment block $B + \tau$ to trace out.

Cutoff schemes There are other cutoff schemes imaginable. While in the canonical procedure the system is projected onto a Hilbert subspace of constant size N_{cut} (“fixed-size cutoff”), this is not the only and best solution for every problem.

Another possibility is to keep the discarded weight $\varepsilon_{\text{disc}}$ below a constant cutoff and to include as many eigenstates of the reduced density matrix as necessary to reach that. This procedure has many disadvantages, e.g. the number of necessary states can unpredictably vary from DMRG step to DMRG step leading to an unpredictably or unfeasible large memory consumption. However, if the system is known to behave well

and is known to require only a few states to converge sufficiently for *some* DMRG steps, one can combine both cutoff schemes and considerably reduce computational resources without losing accuracy. We will call it the “fixed-discarded-entropy” cutoff scheme.

3.2.2 Finite lattice algorithm

The infinite lattice algorithm works well for some systems, especially if the true ground state wave function is so well-behaved in the real-space lattice that a iterative build-up of the approximate ground state wave function from few sites can succeed in converging to the true ground state. However, for other systems, the infinite lattice algorithm is not enough and is only used as a *warm-up* cycle followed by the finite lattice algorithm.

The finite lattice algorithm is not fundamentally different in terms of forming a superblock, tracing to a reduced density matrix, and transforming to the newly reduced basis states. But instead of increasing both blocks A and B , in the DMRG sweep from left to right, the block A is increased at the expense of block B , which is decreased. Since there is fundamentally [11] no obvious procedure how to remove a site from block B (the reverse operation of the tensor product for all operators and the Hamiltonian), one uses the basis states of an earlier step from the infinite lattice sweep to construct the superblock. This requires all operators and wave functions representations in each basis states at the corresponding DMRG step to be saved to disk.

When one repeats this procedure, one will end up with a minimal block B and a large block A , where the size of the superblock is kept constant at all steps. At this point the direction is switched and one sweeps from the right to the left, by increasing block B and reusing a decreased block A from the hard disk. After two full sweeps one returns to a balanced system with equal-sized blocks A and B . All measurements and optimisation apply identically as in the infinite lattice algorithm, except that an efficient book-keeping of basis states is necessary.

3.3 Time development DMRG

The formal solution of the time dependent Schrödinger equation

$$\left(i\hbar \frac{\partial}{\partial t} - H \right) |\psi_0\rangle = 0 \quad (3.5)$$

for a time-independent Hamilton-operator H is $|\Psi(t)\rangle = e^{-iHt} |\psi_0\rangle$. Numerically, the exponentiation of the Hamiltonian matrix is the key difficulty. While there are several methods to tackle the problem of a matrix exponential [12], their success heavily depend on the type of the matrix and if the exponentiation of the matrix $e^H = ?$ or only the matrix exponential operating on a state vector $e^H |\cdot\rangle = ?$ is needed. If the appropriate method is used, this enables us to calculate the time evolution of observables, like the local density $n(x, t) = \langle \Psi(t) | \hat{n} | \Psi(t) \rangle$, or in general any correlation function $C(t) = \langle \Psi | O_1(t') O_2(t) | \Psi \rangle$ (in the Heisenberg picture).

We present two methods that we use to obtain the results in this thesis. Both are defined as extensions to the standard DMRG procedure and referred to as time development DMRG (td-DMRG).

3.3.1 Full td-DMRG

This extension to the DMRG framework as introduced in 2004 [13] divides the time into discrete time steps $0 = t_0 < t_1 < t_2 \dots < T$. For each time step t_i , the matrix exponential operating on the state at the previous time t_{i-1} is explicitly calculated using

$$|\Psi(t_i)\rangle = e^{-iH(t_i-t_{i-1})} |\Psi(t_{i-1})\rangle, \quad (3.6)$$

starting with the action on the ground state at step 2 of the algorithm in 3.2.1. The reduced density matrix in step 3 of the infinite lattice procedure is constructed using all these state vectors, $\rho^{A+\sigma} = \text{Tr} [\sum_i |\Psi(t_i)\rangle \langle \Psi(t_i)|]_{B+\tau}$. As discussed previously, this means that the basis states selected from the reduced density matrix try to optimise all time evolution states (including the $t = 0$ ground state) *simultaneously*. The method is called “full” td-DMRG, since in every DMRG step the full time evolution is calculated (in discrete steps) up to the time T . The procedure carries over to the finite lattice algorithm without modification.

This method is computational intensive, since a.) the more time steps are wanted, the larger the reduced Hilbert space has to be chosen, such that the approximation to the individual state vectors maintains its accuracy and b.) the additional matrix exponential calculation (3.6) scales with the number of time steps wanted. The full td-DMRG also allows to add more time steps during the procedure and in our actual implementation, we first calculate the ground state using the infinite lattice algorithm and add time steps only in the finite lattice sweeps.

The matrix exponential on a state vector (3.6) is efficiently [14, 12, 13] calculated by creating a Krylov space, expressing the exponent $(-iH\Delta t)$ in this subspace and using a Padé-approximation [15, 12] to calculate the full matrix exponentiation for this smaller matrix.

3.3.2 Adaptive td-DMRG

An alternative approach, also developed in 2004 [16, 17, 18], is based on a Suzuki-Trotter decomposition of the time evolution exponential and leaves the usual DMRG framework by introducing approximations that cannot be controlled only by N_{cut} .

One starts with an infinite lattice algorithm, creating a highly accurate ground state $|\Psi(t=0)\rangle = |\psi_0\rangle$. The main idea is to decompose the exponential into terms adjusted to the DMRG sweeping procedure of the finite lattice algorithm. At each DMRG step the (infinitesimal) time evolution at the sites σ and τ can be applied exactly. Instead of a sparse matrix diagonalisation of H_L to determine $|\psi_0\rangle$, a wave function prediction for the blocks A and B and the local time evolution at σ and τ is used to create the wave function at the current time step $|\Psi(t+\delta t)\rangle$. An extra error is introduced by the

decomposition of the order of $(\delta t)^2$ for each DMRG sweep. To keep this Trotter-error small, the time has to be divided into many small steps n of size δt . As a downside, the DMRG truncation error accumulates with every DMRG step D and every sweep S as $(1 - \varepsilon_{\text{disc}})^{DSn} \sim e^n$ for large n , giving rise to an exponential runaway-time, after which the results of the procedure become unreliable.

3.4 Dynamical correlation functions: DMRG

Many dynamical quantities are expressed as functions of energy/frequency and sometimes also resolved in momentum space. In principle, switching to the frequency domain can be done using numerical Fourier transformation on the td-DMRG results.

However, two finite size limits prohibit accurate results in practice for certain frequency domains. On the one hand, the chosen finite time step size Δt bounds the accessible frequency range $\omega \lesssim \Omega \sim 1/\Delta t$ from above, due to the Nyquist sampling theorem. Therefore, the calculation of quantities in the high-energy range requires a high resolution in the time domain. On the other hand, the long term limit of time evolution is bounded to some time T . The range $[0, T]$ restricts the Fourier frequencies to $\omega > \omega_T \sim 1/T$. Or, in other words, any frequency $\omega < \omega_T$ corresponds to a mode with a wave length of the order $\gtrsim T$. Thus, e.g. a correlation function $C(t)$ that does not fall off quickly to 0 within $[0, T]$, will have some weight at $t > T$, which is then wrongly represented in the low-energy range of the corresponding frequency-dependent correlation function $C(\omega)$.

As shown in section 2.4, correlation functions defined in the frequency domain allow for a direct calculation of frequency-dependent quantities

$$C(\omega) = \langle \psi_0 | \hat{O}_1^\dagger \frac{1}{(E_0 - \hat{H}_L - \omega + i\eta)} \hat{O}_2 | \psi_0 \rangle. \quad (3.7)$$

At step 2 of the infinite lattice algorithm and equivalently in the finite lattice algorithm, the operator \hat{O}_1 and the resolvent acting with \hat{O}_2 on the ground state have to be calculated and the following states are included into the density matrix

$$|\psi_0\rangle, \hat{O}_1 |\psi_0\rangle, \frac{1}{E_0 - \hat{H}_L - \omega + i\eta} \hat{O}_2 |\psi_0\rangle, \quad (3.8)$$

which yields a truncated Hilbert space that simultaneously optimises the representation of these target states within the block $A + \sigma$. We calculate the vector $|\xi\rangle = \frac{1}{(E_0 - \hat{H}_L - \omega + i\eta)} \hat{O}_2 |\psi_0\rangle$ by solving the equivalent linear system of equations

$$(E_0 - \hat{H}_L - \omega + i\eta) |\xi\rangle = \hat{O}_2 |\psi_0\rangle \quad (3.9)$$

for the so-called *correction vector* $|\xi\rangle$. In our implementation a Krylov subspace based solver is used, which is pre-conditioned by a solution of some simplified set of equations. Depending on the observable calculated, one needs only the real or the imaginary part of $|\xi\rangle$ and this fact can be exploited in the method. The correction vector method, as

well as two additional methods, the continued-fraction method and the so-call “dynamical DMRG” (DDMRG) [19] are discussed in the reviews about DMRG. Especially the DDMRG, a variational approach to calculate the correction vector, is well described in [20].

The correction vector method directly evaluates $C(\omega)$ and gives an estimate for only one energy ω and the DMRG has to be done for each wanted frequency. Momentum-dependent quantities can also be handled by choosing the correct operators \hat{O}_n in momentum space. In section 4.5 we will show and use examples of such operators for hardwall or periodic boundary conditions and even for non-homogeneous systems.

3.5 Summary

This chapter introduced into the numerical tools that are common in handling quantum many-body problems, especially when modelling one-dimensional strongly correlated systems. While exact diagonalisation quickly reaches a limit in the size of the system, it is invaluable for benchmarking further, approximative tools. We introduced the basic density matrix renormalisation group algorithm that allows to comprehend in what sense it is optimal for the calculation of the ground state. Further, we presented how the DMRG can be extended to calculate arbitrary observables, especially as a function of time and sketched the two most common variants of time development DMRG. Exploiting the knowledge of chapter 2, we finally outline the algorithm to calculate correlation functions within the DMRG framework.

4 Spin-charge separation

Mhmm. Crucifixion party. 'Morning. Now, we will be on a show as we go through the town, so let's not let the side down. Keep in a good, straight line, three lengths between you and the man in front, and a good, steady pace.

(Nexus Wettus in *Life of Brian*, Monty Python)

The experimental observation of spin-charge separation is on the verge of success. We propose a real-time transport setup as being another possibility for experimental verification. Furthermore, calculating the spectral function of an electronic excitation, we investigate the dynamics of various Hubbard model setups.

In one dimension the low energy picture of a Fermi liquid is not appropriate. Fermi liquid theory with its quasi-particle description gets replaced by Luttinger liquid theory whose elementary excitations are collective ones and are bosonic in nature. Especially, there are excitations that carry spin $\pm 1/2$ and no charge (spinon) and ones that carry charge with spin 0 (holon). Within exactly solvable models like the Hubbard model, the splitting of electronic degrees of freedom is explicit. We first try to sketch some of the theoretical concepts but the Luttinger liquid theory [21, 22], the bosonisation technique [23] and the Hubbard model in one dimension [4] are complex topics covered with in textbooks of their own.

4.1 Luttinger liquid

Breakdown of Fermi liquid theory The screening of long-range Coulomb interaction is an essential ingredient for the success of a Fermi liquid as a low-energy effective theory for interacting electrons. In 1D, this screening is greatly reduced to a screening cloud from the right and the left. Thus, the Coulomb interaction is more effective here. Furthermore, rearrangement is completely suppressed in 1D. In a classical picture, electrons can not pass each other, so that individual motion is gone and only collective excitations are possible. Taken both together, one dimension prevents a quasi-particle as an electron moving in a surrounding screening cloud, which has electronic properties, except for renormalised mass and energy.

More formally, a one dimensional system has only two Fermi 'points' $\pm k_F$ and this is the root of the Peierls instability, namely a singular response in a particle-hole perturbation at the wave vector $2k_F$. In other words, unlike in higher dimensions, there is no continuous spectrum at low energy which would allow particle-hole excitations to decay. Due to this singularity, a quasi-particle with electronic quantum numbers is impossible.

As it turns out, the jump of Z in the momentum distribution function n_k when $k \rightarrow k_F$, associated with the weight of a quasi-particle peak in the spectral function, goes to zero in one dimensional systems.

Bosonisation It was found that in one dimension fermions can be represented by bosonic degrees of freedom. The bosonic fields that are related to fluctuations of the *density*, allow an (almost) completely general interacting Hamiltonian to be written down quadratic in the bosons. The paradigmatic Tomonaga-Luttinger model [24, 25] only requires a strictly linear dispersion which extends to $\pm\infty$. The continuum version of the Luttinger model Hamiltonian for one fermionic degree of freedom (spin-less) is then given by [21]

$$H_{LL} = \frac{1}{2\pi} \int dx \left(uK\pi^2(\Pi(x))^2 + \frac{u}{K}(\nabla_{\mathbf{r}}\phi(x))^2 \right), \quad (4.1)$$

where $\pi\Pi(x) = \nabla_{\mathbf{r}}\theta(x)$ and $\theta(x)$ and $\phi(x)$ are the bosonic fields, u has the dimensions of a velocity and K is a dimensionless parameter which incorporates all interactions of the original Hamiltonian. When introducing spin, it turns out in the bosonisation procedure that the bosonic field combinations $\phi_{\rho,\sigma}(x) \sim \phi_{\uparrow}(x) \pm \phi_{\downarrow}(x)$ lead to a Hamiltonian which splits into a charge and a spin sector, each with a Luttinger model type structure.

$$H = H_{LL,\rho} + H_{LL,\sigma} + O(\cos(\sqrt{8}\phi_{\sigma})) \quad (4.2)$$

This is called the spin-charge separation. The Hamiltonian describes collective bosonic charge and spin excitations instead of a fermionic quasi-single-particle picture as in the Fermi liquid theory. See [26], [21] and [23] for details.

Haldane’s conjecture: Luttinger liquid Haldane’s conjecture denotes that for each gap-less degree of freedom, there is an asymptotic low-energy mapping to an effective Luttinger model with only renormalised coupling constant K and renormalised velocity v . Thus, even if the prerequisites of a Luttinger model are not strictly fulfilled and one has a non-linear dispersion, a finite band width, but the excitation spectrum is still gap-less, the low-energy properties of such a system are universal and can be described by an effective Luttinger model.

This universal behaviour was called “Luttinger liquid” by Haldane [27] and the term indicates that in the low-energy and long-wavelength description of certain models it refers to a renormalised Luttinger model in analogy to “Fermi liquids” being two- and three-dimensional models which refer to a renormalised free Fermi gas.

Haldane’s conjecture has been shown to be correct for many models, including the Hubbard model away from half-filling. This will be relevant in the following, when we measure spin and charge velocities. These velocities can be determined for a “bosonised” Hubbard model and even compared to the exact solution of the Hubbard model of the following section.

4.2 Hubbard model in one dimension

In the Hubbard model the kinetic part, i.e. the hopping terms on their own would describe delocalised states but the Hubbard interaction term between spins of opposite orientation tends to localise the systems eigenstates. This leads to a manifold of ground states and phases depending on occupation numbers and interaction strengths. For small interaction around the half-filled system the ground state is a Luttinger liquid for the charge and the spin sector, since linear dispersion is approximately given and a finite band width can be neglected. We will compare our numerical results to the exact results provided by the Bethe ansatz, which we sketch roughly in the following.

Exact solution

The Schrödinger equation of the one-dimensional Hubbard model can be solved analytically by the (nested) Bethe ansatz. The resulting Lieb-Wu equations [28] (notation following [4])

$$\begin{aligned}
 e^{ik_j L} &= \prod_{l=1}^M \frac{\lambda_l - \sin k_j - iu}{\lambda_l - \sin k_j + iu}, & j = 1, \dots, N, \\
 \prod_{j=1}^N \frac{\lambda_l - \sin k_j - iu}{\lambda_l - \sin k_j + iu} &= \prod_{\substack{m=1 \\ m \neq l}}^M \frac{\lambda_l - \lambda_m - 2iu}{\lambda_l - \lambda_m + 2iu}, & l = 1, \dots, M,
 \end{aligned} \tag{4.3}$$

are the focal point for analytic treatments. Here N is the number of electrons (particles), M the number of down spins and L the size of the lattice. The solutions to these equations, the complex roots $\{k_j\}$ and $\{\lambda_l\}$ are called spectral parameters. Many physical quantities, like energy and momenta (and thus dispersion and velocities) of elementary excitations of the many-body system are given in terms of them. In the continuum limit, these roots arrange in a regular pattern (“string hypothesis”) in the complex plane. This allows to classify the solutions into three sets $\{k_j\}$, $\{\Lambda_\alpha\}$, $\{\Lambda'_\alpha\}$, which lie dense in the large L limit and one defines root densities. Analogous to non-interacting electrons, certain combinations of solutions define particle densities or hole densities for each class of solution. These characterise the elementary excitations of the many-body system. The so-called Thermodynamic Bethe Ansatz (TBA) equations for these root distribution functions can be derived and they give rise to the state of thermodynamic equilibrium [29]. Dressed energies and dressed momenta of the elementary excitations follow directly from the TBA equations. The complete, quite complex derivation can be followed in the book by F. Essler *et al.*[4].

For zero magnetic field, the exact solutions show that there are two different types of elementary excitations: gapped or gap-less *holons* (antiholons) with quantum numbers charge $\pm e$ and spin $S = 0$, corresponding to solutions of the spectral parameter k_j and gap-less *spinons* with spin $S = \pm \frac{1}{2}$ and charge 0, corresponding to Λ -solutions. The holons and antiholons are gapped in the special case of half-filling, where the Hubbard model is a so-called Mott-Hubbard insulator, otherwise the holons are gap-less and the

system is metallic. The physical excitations, however, like the removal or addition of an electron or the flip of a spin decompose in combinations of above elementary excitations and are the *permitted combinations* of them.

Weak coupling

In the weak coupling limit away from half-filling, the Hubbard model can be mapped onto a Luttinger liquid in the spin and the charge sector. The explicit expressions for the interaction parameters K_σ and K_ρ of the spin and charge sector are given in terms of the Hubbard interaction U by

$$\begin{aligned} K_\sigma &= \left(1 - \frac{U}{\pi v_F}\right)^{-\frac{1}{2}}, \\ K_\rho &= \left(1 + \frac{U}{\pi v_F}\right)^{-\frac{1}{2}}, \end{aligned} \tag{4.4}$$

while the corresponding velocities are given by

$$\begin{aligned} v_\sigma &= v_F \left(1 - \frac{U}{\pi v_F}\right)^{\frac{1}{2}}, \\ v_\rho &= v_F \left(1 + \frac{U}{\pi v_F}\right)^{\frac{1}{2}}. \end{aligned}$$

In contrast to the non-interacting system, where $K = 1$, for repulsive interaction $U > 0$ the spin velocity decreases while the charge velocity increases. We will use these results in the transport setup later in this chapter and recapitulate them in chapter 6 in the context of the SU(3) Hubbard model.

4.3 Observation of spin-charge separation

From the previous two sections, we see that spin-charge separation is manifest from various points of view or theoretical descriptions. We will now summarise these.

Manifestations of spin-charge separation

- On the level of a cartoon picture Fig. 4.1, the mechanism of spin-charge separation is explained the easiest. In a Néel ordered half-filled chain of electrons, we take out one electron. The created hole can be viewed as a charge excitation, which hops from site to site with energy t (first to second chain in Fig. 4.1). Once the hole is gone, the remaining misaligned spins can be interpreted as a spin excitation. Such a local spin deformation (compared to the antiferromagnetic background) can travel completely independent of the movement of the hole via spin-flips between neighbouring electrons, since the spin-flip process occurs with exchange energy J

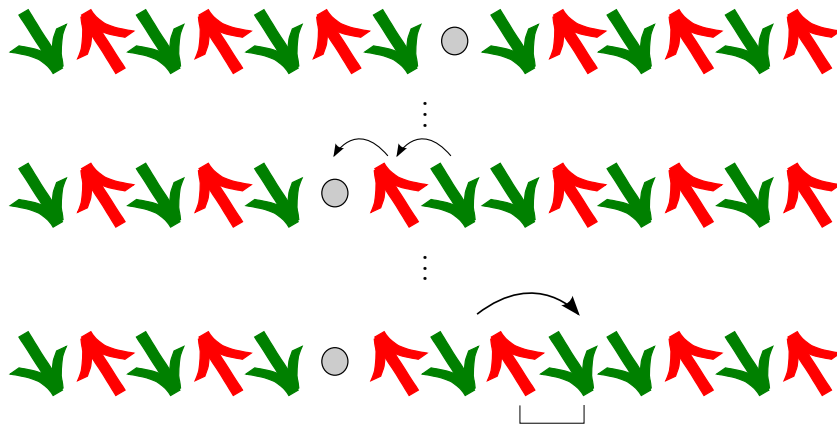


Figure 4.1: Cartoon picture of the mechanism of spin-charge separation. In the second spin chain the hole hopped two sites, while in the third chain the neighbouring down spins hopped two sites via one spin flip.

(second to third chain). Thus, spin and charge move with separate velocities due to separate energy scales on which movements occur. This picture is too simplified, since the real elementary excitations are collective, non-local ones, e.g. as described by Luttinger liquid theory or microscopic models. Also, the effect of spin-charge separation does not depend on a specific ordering, like the antiferromagnet shown in the cartoon.

- For the Luttinger model as well as in the framework of a Luttinger liquid the spin-charge separation occurs already on the level of the Hamiltonian. Spin and charge velocities are generic independent parameters of the spinful theory. The single particle spectral function displays instabilities at the energies of the corresponding spinon or holon excitation, but not at the energies and momenta of a single hole or single electron. Also, transport experiments have been considered in this theory. However, we need to go to a semi-classical description of the bosonic fields in terms of density distributions to identify a particle creation or annihilation in the framework.
- In exactly solvable microscopic models, like the Hubbard model, spin and charge degrees of freedom decouple on the level of elementary excitations. The cartoon picture of local electron or spin-flip excitations translates directly to holons and spinons despite the fact that the latter are collective non-local excitations. When looking at the single particle spectral function or the spin or charge susceptibilities, one can directly identify holon and spinon excitations, the holon-spinon excitation continuum and their spectrum. One defines spin and charge velocities as the group velocities of wave packets in the low-energy limit close to the Fermi surface. Therefore, the density distribution of a fermionic wave packet should split up into a charge density and a spin density and a transport setup could be realized.

No spin-charge separation The counterintuitive fractionalisation of the electronic degrees of freedom in one dimension leads sometimes to views that deserve closer attention.

- One can manage to have excitations moving with two different speeds in a non-interacting system. For example, if a magnetic field is applied to a system with spinful non-interacting fermions, up and down spins display different dispersion curvatures at their shifted Fermi surfaces. This is not a sign of spin-charge separation.
- One can also achieve density and spin excitations moving with different velocities in a non-interacting system, if one superimposes the right combination of several electron excitations, e.g. if one excites several eigenstates with different momenta and energies. Instead, it is crucial that spin-charge separation occurs already at the level of a single electronic excitation.

4.3.1 Experimental evidence

Halperin [30] summarises the experimental systems that might exhibit physics peculiar to one dimension and, in particular, spin-charge separation.

Certain organic and inorganic *bulk materials* are said to be quasi-one-dimensional in a certain temperature window. Lorenz *et al.*[31] deduced separate charge and spin velocities from thermal conductance measurements in the organic crystal $(\text{TMTTF})_2\text{PF}_6$. However, since the publication was retracted later, it shows how far experiments are still from a clear signature of spin-charge separation. Other techniques use ARPES on the organic conductor **TTF-TCNQ** [32] or on **SrCuO₂** [33] to find evidence of spinon and holon resonances in the spectral function.

On the contrary, **single-wall carbon nano-tubes** in their metallic configuration are examples of *isolated wires*. Most promising results come from single point tunnelling experiments [34], while other techniques try to measure spin accumulation in non-local geometries on single wall nano-tubes [35]. Furthermore, **quantum wires** can be constructed from cleaved-edge overgrown two-dimensional electron gases as in GaAs/AlGaAs. Here momentum-conserved tunnelling between parallel nano-tubes by Auslaender *et al.*[36] seems to allow the extraction of spin and charge velocities. But also here, Halperin states [30] that earlier results, using Raman spectroscopy on similar systems and claiming to see different spin and charge velocities (Ref. 7,8 in [30]), are doubted to be reliably explainable by the Luttinger liquid theory. Then there are metallic **atom chains**, like e.g. gold deposited on the edges of suitable crystallographic directions, e.g. on Si(111) [37] or more recently on Ge(001) [38]. These objects are very close to strict one dimension and ARPES as well as scanning tunnelling microscopy is used to find one-dimensional physics. Finally, where **edge states** of fractional quantised Hall systems can be found in nature, a chiral version of Luttinger liquid is used in the description. However, spin does not play a significant role and it is thus unsuitable for detecting spin-charge separation.

It is notable that even in two dimensions, especially for **high-temperature superconductors**, one-dimensional physics is probed for and believed to exist [39].

This list is not comprehensive and beside the experimental realisations, there are also propositions to find signatures of spin-charge separation, which are likely to be experimentally realized in the near future. For example, reaching the low dimensionality in cold bosonic atomic gases [40, 41]. Further, there is a proposition to use magnetotunnelling [42] on a quantum wire. Also, we left out any works on pure spin-systems. As we show in the following section, we add a proposal to measure spin-charge separation in a transport setup [1] similar to a sketch within Luttinger liquid description earlier by Safi and Schulz [43].

4.3.2 Numerical simulation evidence

Approaching spin-charge separation by looking at the dynamics of wave packets, the first numerical simulations were performed by Jagla *et al.*[44] using exact diagonalisation for 16 sites. They constructed an additional electron with a Gaussian distribution of crystal momenta, identically to our setup in section 2.3. Preuss *et al.*[45] and Zacher *et al.*[46] used various methods in Quantum Monte Carlo simulations to study the spin and charge susceptibilities of the Hubbard model with varying resulting accuracies.

Kollath *et al.*[40, 41] presented the first spin-charge separation calculations in the framework of adaptive time dependent DMRG (td-DMRG). This calculation was redone by Schmitteckert [47], keeping up to 5000 states per DMRG block showing that the adaptive time evolution scheme in [40] suffered a large numerical error. Additionally Schmitteckert and Schneider [48] used at least 10,000 states per DMRG block to show spin-charge separation in a 33 site system with periodic boundary conditions. Both Kollath and Schmitteckert followed the time evolution of a Gaussian potential switched off at $T = 0$, identically to the setup in chapter 2.2. The following section 4.4 of this thesis will treat the case of a transport setup with two non-interacting leads, where the system was prepared with an additional electron as in the work of Jagla *et al.*[44]. In order to avoid the numerical problem associated with the adaptive time evolution scheme as discussed above and to avoid the numerical costs of a pure full td-DMRG we apply a hybrid of both methods, see [47, 49]. To a large extend this is published in [1].

4.4 Spin-charge separation of one electron in the Hubbard model

We want to illustrate the spin-charge separation at first qualitatively by looking at density distributions evolving over time. The complete simulation described in this section is encoded in a video under <http://www.tkm.uni-karlsruhe.de/~ulbricht/scs> which allows to have a real experience of the time dimensionality of the setup.

We use the particle-hole symmetric repulsive Hubbard model on a lattice of size M for spin- $\frac{1}{2}$ fermions, given by

$$H_{\text{bulk}} = \sum_{\sigma=\uparrow,\downarrow} H_{\text{tb},\sigma} + U \sum_{x=1}^M \left(n_{x,\uparrow} - \frac{1}{2} \right) \left(n_{x,\downarrow} - \frac{1}{2} \right) \quad (4.5)$$

where the Hubbard interaction strength U is positive. Since we set the hopping matrix element between neighbouring sites to 1, we are free to denote the time variable by t . If we put N_\uparrow up-spin electrons and N_\downarrow down-spin electrons into the system, we have a filling of

$$n = \frac{N_\uparrow + N_\downarrow}{2M} \quad (4.6)$$

and a spin polarisation of

$$p = \frac{|N_\uparrow - N_\downarrow|}{N_\uparrow + N_\downarrow} \quad (4.7)$$

in favour of one spin species or the other.

Using DMRG (chapter 3) we aim for the calculation of the ground state $|\Psi^0\rangle$. Additionally, we construct the normalised state $|\Psi^{+1}\rangle$ where we have added one electron (or hole) in the ground state. This excited state is created using the creation (or annihilation) operators in momentum space with a Gaussian distribution around some k_0 as described in detail in section 2.3. Time evolution on these states with $\exp(-iH_{\text{bulk}}t)$ will finally allow us to calculate observables at any simulated time step t . We will look at the density of each spin type σ

$$n_\sigma(x, t) = \langle \Psi^{+1}(t) | c_{x,\sigma}^\dagger c_{x,\sigma} | \Psi^{+1}(t) \rangle \quad (4.8)$$

The sum of both $n_c(x, t) = n_\uparrow(x, t) + n_\downarrow(x, t)$ is the local particle (or charge) density, while the difference gives us the local spin density $n_s(x, t) = \frac{1}{2}(n_\uparrow(x, t) - n_\downarrow(x, t))$. We also calculate the static ground state density in the original ground state $n_\sigma^0(x) = \langle \Psi^0 | c_{x,\sigma}^\dagger c_{x,\sigma} | \Psi^0 \rangle$ at time $t = 0$ and form the corresponding charge and spin densities n_c^0, n_s^0 . $|\Psi^0\rangle$ is in all cases we consider an eigenstate of the Hamilton operator so that it is invariant under time evolution and the time index can be dropped. Then we will plot the quantities $n_s(x, t) - n_s^0(x)$ and $n_c(x, t) - n_c^0(x)$. This trick evens out all stationary oscillations already present in the ground state, like the Friedel oscillations resulting from using hard-wall boundary conditions.

4.4.1 Non-interacting case

In the case $U = 0$ the Hamiltonian (4.5) reduces to one tight-binding Hamiltonian for the dynamics of each spin orientation. There is no spin-flip possible and the only implicit interaction is the Pauli principle. Nevertheless, this is the reference system for all following simulations.

Our example is a system of size $M = 102$, which is at half-filling plus one electronic excitation, so $N_\uparrow = 51 + 1$. The $N_\downarrow = 51$ down-spins are irrelevant in the non-interacting case and constant in the time evolution. The additional up-spin electron is created at the real space position $x_0 = 15$ (Fig. 4.2, upper diagram). The excitation's momentum is centred around $k_0 = \pi/2 + 0.1$ and thus the packet travels to the right. With the width of $\sigma_0 = 0.03$ we ensure that the momentum distribution is far away (compared to the width) from the Fermi surface $k_0 \sim k_F + 3\sigma_0$ but still as close as possible to the linear regime of the cosine band at k_F . Fig. 4.2 shows snapshots of the spin density $n_s - n_s^0$ (solid,

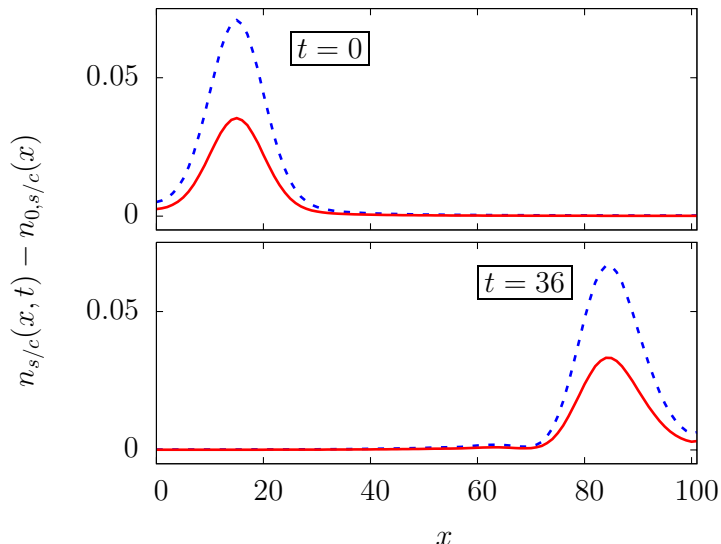


Figure 4.2: (Colour online) Spin (solid, red) and charge (dashed, blue) densities of a td-DMRG simulation of one additional up-electron over the background of a half-filled tight-binding model for each spin species. The Gaussian excitation on the left at time $t = 0$ (upper diagram) moving to the right at $t = 36$ (lower diagram) retains its shape. Averaging is described in the text.

red lines) and the particle (charge) density $n_c - n_c^0$ at $t = 0$ and $t = 36$ subtracted from the corresponding original ground state density (at half-filling). Additionally, to even out Friedel oscillations with wave vector $2k_F = \pi$ resulting from the density distortion, a three-point average of the data was performed. This system was calculated using constant $N_{\text{cut}} = 1000$ states per DMRG block, applying 10 time steps in the full td-DMRG and also keeping 1000 states for the consecutive adaptive T-DMRG.

Analysis In the non-interacting case, the densities of the original ground state $|\Psi^0\rangle$ are constants $n_c^0 = 1$, $n_s^0 = 0.5$ in space and time. This we find also numerically. Since we created a spin-up excitation, the spin-down channel is, as expected, completely uncoupled from the spin-up channel and we find numerically $n_\downarrow = 0.5$ being independent of x and t . Although spin and charge densities now basically reduce to the data coming from the dynamics of the spin-up channel only $n_c = 2n_s = n_\uparrow$, we analyse the Gaussian charge density profile $n_c(x, t)$ for direct comparison with the following sections. Further, it is instructive to note that although $|\Psi^{+1}\rangle$ is not an eigenstate of the Hamiltonian, it was constructed from the ground state only with single particle operators which alone create eigenstates of the Hamiltonian.

The accuracy of our calculation can be checked against an exact diagonalisation, which implements the time evolution matrix exponential function in the diagonal basis. We define the peak relative error between DMRG and exact diagonalisation results (ED) in the densities by

$$\delta n_p(t) \equiv \max_x \left| \frac{n_{\text{ED}}(x, t) - n_{\text{DMRG}}(x, t)}{n_{\text{DMRG}}(x, t)} \right| \quad (4.9)$$

This quantity reaches from initial $\delta n_p(0) = 7 \cdot 10^{-5}$ to $\delta n_p(36) = 7 \cdot 10^{-3}$ peak relative error at $t = 36$, see appendix A.1. This striking accuracy of DMRG is achieved with the discarded entropy never exceeding 10^{-5} during the simulation.

Finally the group velocity of the packet as the velocity of the peak maximum can be extracted from the simulation. In appendix A.1, we show that the extracted velocity

of the DMRG calculation is about 0.3 % slower than an exact calculation. Comparing to the excellent accuracy in the density, the velocity is a much more sensitive quantity. The expected group velocity for the momentum $k_0 = \pi/2 + 0.1$ is about $v_c \sim 1.990$. And, as indicated in section 2.3 and Fig. 2.6, finite size scaling suggests this value is reached asymptotically. Here we find, for systems of about 100 sites, the finite size effect is such that both DMRG and exact calculation are about 2-3 % slower than the expected group velocity. In principle both the DMRG error and the finite size error can be made arbitrarily small by increasing the number of DMRG states and by increasing the system size, respectively, with computing resources being the only restriction.

4.4.2 Strongly interacting case

In the case $U \neq 0$, the dynamics of both spin species are interwoven and spin-flip processes completely destroy a single particle description. We repeat the previous setup and simulation now for $U = 4$ (in units of the hopping energy $t_{\text{tb}} = 1$). While the previous excitation was a superposition of well-defined eigenstates in the tight-binding model, it is not clear which eigenmodes are excited by adding/removing an electron from an interacting system. Nevertheless, using the same $c_{\sigma x}^{(\dagger)}$ in equation 2.23 to create an excited state $|\Psi^{+1}\rangle$ still results in a Gaussian shape in spin and charge densities (see Fig. 4.3), although the corresponding Fourier transformed operators $c_{\sigma k}^{(\dagger)}$ no longer create an eigenstate of the system.

This time we insert an excitation corresponding to one (up-spin) hole into the ground state of a repulsive particle-hole symmetric Hubbard model (4.5) with $U = 4$ at a filling of $\frac{41}{90} \approx 0.46$ with a central momentum $k_0 = \pi/2 - 0.5 \sim k_F - 7\sigma_0$ and a width of $\sigma_0 \sim 0.053$. The calculations were carried out with $N_{\text{cut}} = 2500$ states kept per DMRG block in the full and adaptive td-DMRG. Fig. 4.3 clearly shows that during time evolution between $t = 0$ (upper diagram) and $t = 25$ (lower diagram) the peaks split up, basically retain Gaussian shape but broaden and melt down. In this respect, the spin peak changes less than the charge peak. There is also a distinct second charge peak running in the opposite direction, being reflected on the right wall, located at around $x = 60$ at $t = 25$.

Analysis The splitting of the charge and density peaks shows genuine SCS, driven by the Hubbard interaction. Accounting for the slow-down resulting from the finite size discussed in the previous section of about 3%, we can estimate a systematic error to the extracted group velocities from the main peaks: $v_S = 1.12 + 0.03$ and $v_C = 2.02 + 0.06$. The one dimensional Hubbard model can be solved exactly [28]. From the analytic expression by Coll [50], the spin and charge velocity of the low energy spinons and holons can be derived as done, e.g. by Schulz [26] and [51]. Surprisingly, we can compare to the thermodynamic limit exact result of charge and spin velocities, which are taken from the long wavelength limit $k \rightarrow 0$. In Fig. 4.4, the charge and spin velocities for the filling corresponding to the central momentum $n_c = k_0/\frac{\pi}{2} \approx 0.68$ are about $v_{\text{one holon}} = 2.05$ and $v_{\text{one spinon}} = 1.15$ as can be read off from the figure from Schulz. Although we

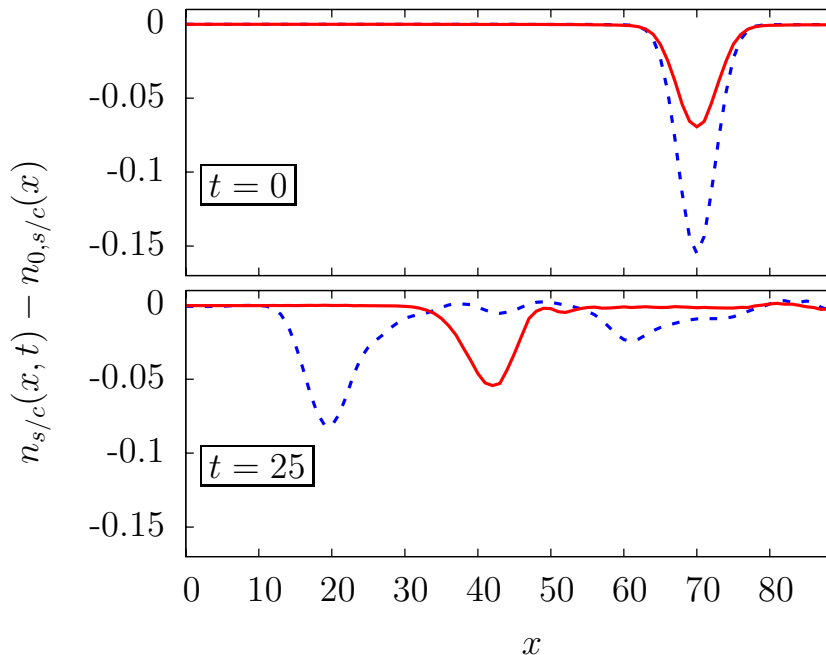


Figure 4.3: (Colour online) Spin and charge density (see legend of fig. Fig. 4.2) in a Hubbard model at time $t = 0$ (upper diagram) and $t = 25$ (lower diagram) show spin-charge separation. This is data from a td-DMRG simulation on 90 sites system with $N_{\uparrow} = 41 - 1$, $N_{\downarrow} = 41$ electrons and a Hubbard interaction of $U = 4$.

are with 90 sites far from simulating the thermodynamic limit and despite our finite excitation width, the group velocities of our spin and charge density fit remarkably well to the Bethe ansatz results for the velocity of one spinon and one holon. A similar good agreement was found for a spinless Luttinger liquid simulation [13] using a perturbing potential as excitation.

The second charge peak with opposite momentum can be traced back to interaction effects of the underlying elementary excitations. First of all, we cannot claim to excite one holon and one spinon of a Luttinger liquid, since we are on a lattice of finite bandwidth, have a finite initial electronic momentum width, and use single particle states for our initial excitation. Nonetheless, in the Luttinger framework it is known that interaction mixes left and right moving elementary excitations in the charge sector but not in the spin sector. Therefore, we deduce that our excitation using c_{k_0} on the ground state creates right and left moving parts only in the charge sector.

The broadening and decrease in height of peaks has two sources. One is the finite size of the system (including the non-linear band). Comparing to the $U = 0$ case, we can estimate the decrease and broadening from the finiteness of our system to be small. Instead, we expect that our initial configuration excites complicated many particle states in the system which all might interact, especially as long as the densities are not completely spatially separated. Finally, there is charge density accumulation trailing the main charge peak and at the location of the spin peak. These might be more complicated

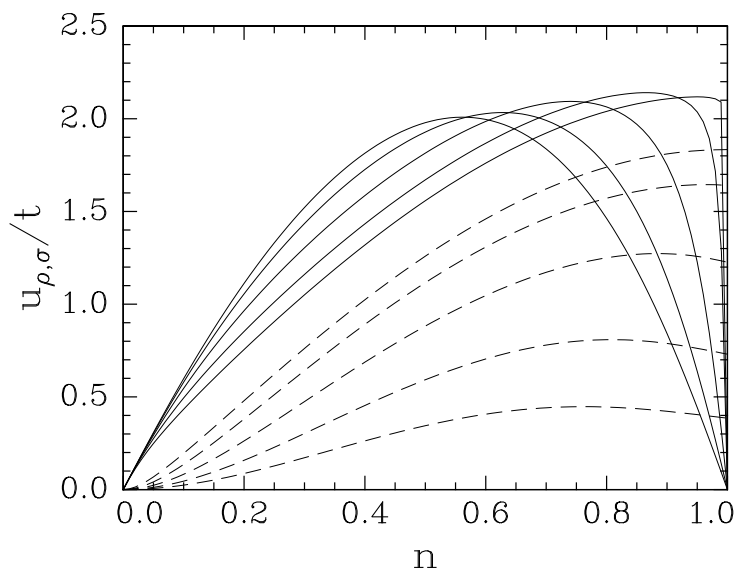


Figure 4.4: Spinon and holon velocities of the exactly solvable Hubbard model for different electron densities. $n = 1.0$ corresponds to half-filling. The solid lines correspond to the charge velocity u_ρ for interaction $U = 16, 8, 4, 2, 1$ from top to bottom in the left part, the dashed lines correspond to the spin velocity u_σ for interactions $U = 1, 2, 4, 8, 16$ from top to bottom. Reprinted with permission from Int J. Mod. Phys. B, 5 (1-2), 57-74, 1991, World Scientific Publishing [51, 26].

features of the interaction or result from the finite size effects that are more pronounced than in the non-interacting example.

4.4.3 Spin-charge separation in a transport setup

A transport setup is a setup where a probe is connected to two or more leads so that applying a voltage (sometimes called source-drain voltage V_{SD}) results in a possible measurement of transport properties like the current, the full or differential conductance or stochastic features like shot noise. For the purpose of spin-charge separation, we model a transport setup with a one-dimensional interacting region, which is connected to non-interacting leads on both sides each by a single contact. The underlying exemplary microscopic models for electrons on a lattice are the tight-binding model for the leads and the Hubbard model for the structure. The main idea is to prepare a groundstate where an additional electron with an average momentum k_0 is placed into one of the leads. The excitation passes through the interacting region, where it undergoes the spin-charge separation and ends up in the other non-interacting lead, where a spin-resolved and time-resolved measurement of charge density is carried out.

This setup poses the following questions: If one injects an electron with definite momentum at some time t_0 into an interacting system, where the separation of spin and charge is known to happen. What happens to the electronic excitation within the inter-

acting region? And what kind of excitation emerges from the interacting area at a later time? Will we see distinct excitations in spin and charge density, will we find spin and charge density to be recombined to one full electronic excitation, or will we obtain an incoherent superposition of many excitations?

The complete Hamiltonian for SU(2)-fermions (like electrons) with total spin $s = \frac{1}{2}$ used for our setup is

$$H_{\text{transport}} = \sum_{\sigma=\uparrow,\downarrow} H_{\text{tb},\sigma} + U \sum_{x=x_1..x_2} \left(n_{x,\uparrow} - \frac{1}{2} \right) \left(n_{x,\downarrow} - \frac{1}{2} \right) + V_{\text{gate}} \sum_{x=x_1..x_2} (n_{x,\uparrow} + n_{x,\downarrow}) \quad (4.10)$$

where $H_{\text{tb},\sigma}$ is the nearest neighbour hopping tight-binding operator discussed in section 2.1 for each spin species. U is the Hubbard interaction strength and V_{gate} the strength of an additional chemical potential, both acting only on the central region enclosed by the sites x_1 and x_2 . Since the repulsive Hubbard interaction tries to avoid double occupation in the system, the average particle density (the filling) will be different on the central region than in the leads. The gate voltage thus serves two purposes. It is used to tune the local average density on the central region to a value less than half-filling. We also choose it to level the Fermi surface to a half-integer number of up and down electrons on the structure. This minimises reflections into and out of the area (see Fig. 4.5). This local chemical potential was pre-calculated in a self-consistent way.

We use a system of $M = 100$ sites, split into 41, 29 and 30 sites for the different areas ($x_1 = 41, x_2 = 70$) and a total of $N_{\uparrow} = 48 - 1, N_{\downarrow} = 48$ electrons. The gate voltage levels the Fermi surface on the interacting structure is such that we have $N_{\uparrow} = N_{\downarrow} = 12.5$ electrons there, leaving $N_{\uparrow} = 35.5 - 1, N_{\downarrow} = 35.5$ electrons for remaining 71 lead sites. Thus, we have a Hubbard model at ~ 0.43 -filling in the central (black bar) area and half-filled tight-binding leads. We also choose parameters $k_0 = 0.43\pi - 2\sigma_0, \sigma_0 = 0.03$ to maximise tunnelling while staying as close as possible to a quasi-linear dispersion. The number of DMRG states kept was $N_{\text{cut}} = 2500$.

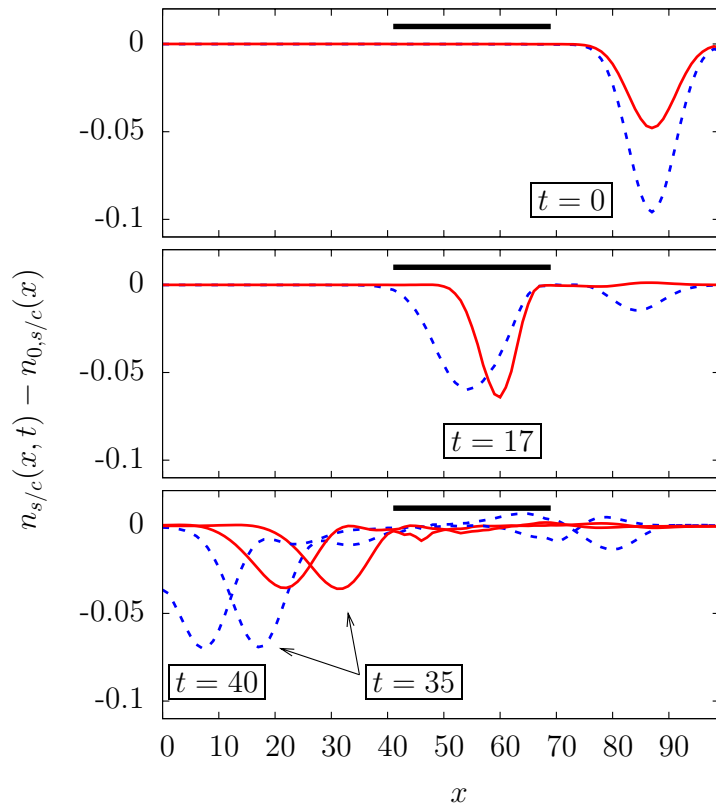
Fig. 4.5 shows the time evolution of spin and charge densities for several times. The majority of spin and charge density transmits through the nano-structure. SCS clearly happens inside the interacting region (central diagram at $t = 17$) and SCS remains intact after leaving the interacting area into the opposite lead (lower diagram at $t = 35$ and $t = 40$). Here spin and charge now travel along separately but again with identical constant velocity.

There are also reflections of charge and spin density at both edges of the structure. They are suppressed by the choice of the chemical potential as discussed above, however, these reflections are no artefact and understood in a Luttinger liquid descripton [43]. Safi and Schulz sketch such a transport setup and give a reflection coefficient of two Luttinger liquids with K_1 and K_2 at an interface of

$$\gamma = \frac{K_1 - K_2}{K_1 + K_2}$$

The reflection coefficient can become negative for $K_2 > K_1$, leading to an enhanced transmission while the reflected wave is of opposite amplitude. Since we are close to the

Figure 4.5: (Colour online) Excitation in a transport experiment: a created hole in the right lead (upper diagram, at $t = 0$) passes the interacting nano-structure (black bar) undergoing SCS (central diagram, at $t = 17$). At $t = 35, 40$ (lower diagram) spin and charge densities travel independently with equal velocity in the left lead.



Fermi surface, our interaction is not too strong, we can relate to that work. Indeed, following the complete time evolution (e.g. the video¹), one identifies the several reflections. First of all, $K_\sigma = K_\rho = 1$ in the non-interacting leads, while $K_\sigma > 1$ and $K_\rho < 1$ in the interacting region following (4.4) in section 4.2. Correspondingly, at the first interface the spin packet has a negative back-reflection ($\gamma < 0$, slightly visible at $t = 17$), while the charge peak gets positively reflected ($\gamma > 0$, well visible at $t = 17$). The transmitted excitations now change roles at the second interface, going from $K_\sigma > 1, K_\rho < 1$ into $K_{\rho,\sigma} = 1$ with a positive reflection of the spin wave ($\gamma > 0$, barely visible peak at $x \approx 50$ for $t = 35$) and a negative reflection of the charge wave ($\gamma > 0$, well visible as a peak at $x \approx 63$ for $t = 35$).

Analysis In our simulation of a microscopic experiment on an interacting nano-structure we see that the spin and charge excitation of an injected electron can be separated as it is known to happen in one-dimensional interacting systems. We confirm for the Hubbard model, what Safi and Schulz [43] sketched for a low-energy Luttinger liquid transport setup with restricted interaction: The spin and charge separation can be directly observed by a time-resolved measurement of the spin-polarised density. There is no need for spin and charge to recombine to a complete electron (hole) for a measurement of a single electron (hole). Note that the charge and spin excitations in the non-interacting leads are valid excitations of the Fermi liquid. They are not *elementary* excitations

¹<http://www.tkm.uni-karlsruhe.de/~ulbricht/scs>

of the Fermi liquid, instead they are a composition of (at least) two excitations of the Fermi liquid. However, the resulting distribution of separated densities originated from a single particle injection into the Fermi sea.

One may ask, how the electrons travel from a battery through this system and end up again in a battery or pass a voltmeter, where only unfractioalised electrons are counted. A simple answer is that as in the case of Andreev reflection of electrons and holes on the boundary to superconducting material, a single electron in the proper energy level can always be created by also creating an antiparticle (hole) that propagates in the different direction or in our case, by creating the appropriate composition of elementary excitations and their counterpart that add up to a single electron or hole.

Outlook Experimentally, the measurement of the densities would have to happen on a time scale which is set by the Fermi velocity and the length of the interacting system. For nano-scale systems and metallic excitation velocities tens of Terahertz resolution would be required, which might be achieved using optical techniques. It is of general interest to know whether a series of quantum dots or any other strongly correlated system with a much smaller Fermi velocity can provide the ingredients for the realisation of such a transport setup. Lowering the Fermi, holon and spinon velocities would enhance the detection possibilities. It is interesting that our small system already shows the fingerprint of Luttinger liquid description expected in the thermodynamic limit. Also note that even for highly energetic incoming electrons we find the spin-charge separation, albeit obscured by band effects. With the td-DMRG method even more realistic models, like the extended Hubbard model with a finite next-nearest neighbour interaction could be investigated.

4.5 Spectral function in the Hubbard model

In this section we investigate spectral functions for various setups within the Hubbard model. Since the single particle spectral density function $\mathcal{A}(k, \omega)$ reveals important properties of the elementary excitation spectrum, we can identify the separated spin and charge sector's excitations of the underlying microscopic model. A major advantage is the fact that with photoelectron spectroscopy there is also an experimental tool available which allows for comparison between experiment, model and numerical simulation.

4.5.1 Spectral function

Our starting point is the single particle spectral function being the imaginary part of the single particle propagator (as in section 2.4, equation (2.36))

$$\mathcal{A}(\omega) = -\frac{1}{\pi} \text{Im}(\mathcal{G}_{A,B}^r(\omega)).$$

Taking the operators $B = A^\dagger = c_{x\sigma}, \mathcal{G}_{c_{x\sigma}^\dagger, c_{x\sigma}}(\omega)$ corresponds to the annihilation of an electronic state localised at position x with spin σ and the spectral function tells us how the system reacts on that perturbation.

More generally, we will take $B = A^\dagger = c_{k,\sigma}$, where k denotes a state, e.g. a Bloch state. The actual sensible choice of operators $c_{k,\sigma}$ depends on the system under investigation. For lattices with periodic or anti-periodic boundary conditions and translationally invariant Hamiltonians, like the tight-binding model, we can choose the Bloch states

$$c_{k,\sigma} = \frac{1}{\sqrt{M}} \sum_{x=1}^M e^{-ikx} c_{x,\sigma}, \quad (4.11)$$

with $k = 2\pi l/M - \pi$ for $l \in \{1, \dots, M\}$. This allows us to calculate momentum dependent correlation and spectral functions. In the following sections on the Hubbard model on a lattice, we use hard-wall boundary conditions. Under these conditions, the better choice of operators are given by the solution of the particle in a box problem

$$c_{k,\sigma} = \sqrt{\frac{2}{M+1}} \sum_{x=1}^M \sin(kx) c_{x,\sigma}, \quad (4.12)$$

where $k = \pi l/(M+1)$ for $l \in \{1, \dots, M\}$. Note that the M different solutions of ks are defined in the halved Brillouin zone, due to the symmetry restrictions on the solutions. It was numerically verified by Benthien, Gebhard and Jeckelmann [52, 53] that in the thermodynamic limit $M \rightarrow \infty$ both expansions are equivalent. We verify this equivalence very easily for the case of non-interacting fermions. Furthermore, we will find in section 4.5.4 that the Hermite polynomials are a sufficiently good choice of operators to calculate single particle correlation functions in a low-filled Hubbard model with a quadratic trap potential.

A good recent overview for using DMRG to calculate correlation functions is given by Jeckelmann [20]. We use the correction vector method embedded in the DMRG framework as described in section 3.4 to calculate the resolvent for the spectral function in the interacting systems or when recovering the non-interacting case of (2.47).

The non-interacting case Let us look at the single particle spectral function of the tight-binding chain. With hard-wall boundary conditions, we know the creation operators equivalent to (4.12) to be the exact single particle states that build up the ground state $|\Psi_0\rangle = \prod c_{k,\sigma}^\dagger |0\rangle$. The momentum-resolved spectral function, broadened by the imaginary shift η , is a Lorentz function given by (2.47). We check our numerical approach using operators (4.12) in the expression of the Greens function for a general pair of operators (2.51). Fig. 4.6 shows that this works for a system of $M = 30$ sites, a broadening of $\eta = 0.1$ and a resolution of $\Delta\omega = 0.1$, since for each quasi-momentum k , we get a perfect Lorentz function (colour coded) with an intensity maximum of η . While the left panel shows $\pi\mathcal{A}(k, \omega)$ obtained from the retarded Greens function, on the right panel we plot only $\pi\mathcal{A}^<(k, \omega)$ (see (2.39)), showing that we only have a response below the Fermi surface, which was here defined by putting only $N = 13$ fermions into the system. Fig. 4.6 depicts the one-particle excitation spectrum which results from the removal of one electron below the Fermi surface or the addition of one electron above

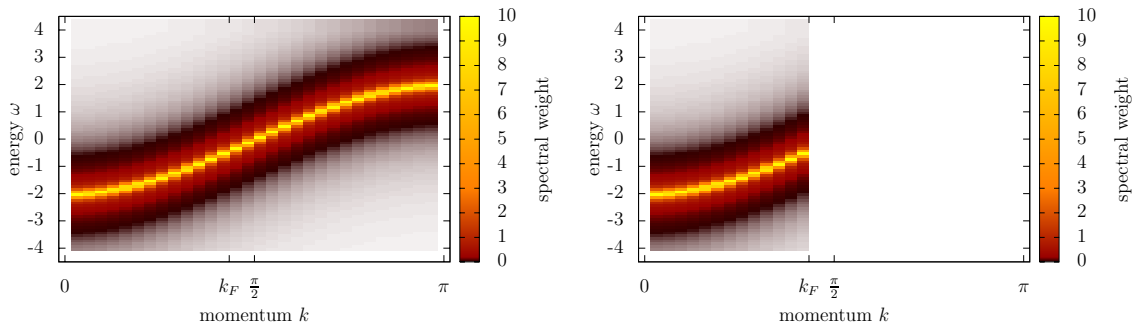


Figure 4.6: Spectral function of the tight-binding chain with hard-wall boundary conditions, lattice size $M = 30$ and $N = 13$ fermions and a broadening $\eta = 0.1$. Left plot shows $\pi\mathcal{A}^r$ and the right plot shows $\pi\mathcal{A}^<$. Note that the white area (above the Fermi momentum) is numerically 0.

the Fermi surface with the excitation energy

$$\left. \begin{aligned} \varepsilon_{N-1}(k \leq k_F) &= E(N) - E(N-1) \\ \varepsilon_{N+1}(k > k_F) &= E(N+1) - E(N) \end{aligned} \right\} = -2t \cos(kx). \quad (4.13)$$

The same result can be found for the periodic boundary condition system using the Bloch plane wave solutions, albeit now with k extending over the full Brillouin zone.

We repeat a few textbook results about the spectral function in finite systems:

- In general, many features of elementary excitations can be read off the single particle spectral function. An η -broadened peak indicates a particle/hole excitation and an additional finite width (beside the η) indicates a finite lifetime of a quasi-particle.
- In higher dimensions, where Fermi liquid behaviour is appropriate, the picture remains still valid for short range interaction and η -broadened peaks indicate quasi-particles. Furthermore, a continuum of excitations will manifest itself in continuous, incoherent structures in the spectral function.
- In the thermodynamic limit $M, N \rightarrow \infty, n = N/M = \text{const.}$ the Lorentz function becomes a δ -function. Since we are restricted to finite systems and therefore require a finite broadening, a deconvolution of the underlying Lorentz-function is sometimes useful in our simulations.

In the exact diagonalisation of the non-interacting system, we can, of course, make η arbitrarily small from the beginning, or check that our manual deconvolution of this finite size effect described in section 2.4 works.

The interacting case Let us come back to the Hubbard model. Correlation functions of the Hubbard model can not directly be derived from the Bethe ansatz solutions as

one can for the ground state [28] or excited state energies [54, 50]. Conformal field theory (CFT) provides a relation between finite-size corrections of the spectrum and the critical exponents governing the power-law decay of correlation functions. Since the Hubbard model away from half-filling is conformally invariant in the low energy limit (excitations close to k_F and the long-range behaviour), correlation functions can be derived in this regime for all values of U . At half-filling, where the conformal approach is not applicable, only in the weak coupling limit $U/t \ll 1$ and in the scaling limit of infinite system size, correlation functions could be analysed. Only recent developments using a pseudofermion dynamical theory (PDT, see Ref. [55] and references therein) facilitate the calculation of the spectral function in the Hubbard model [56] without the limitation of being perturbative in large or small interaction or the restriction to a low energy effective theory. There is a wide regime of the parameter space, which is explored only very recently or not yet at all by analytical means.

Therefore, numerical methods have been used a lot to examine correlation functions. Beside exact diagonalisation on small systems, Quantum Monte Carlo methods [45, 46] have been applied on Hubbard models. However, especially DMRG has become the most successful tool to investigate correlation functions for such interacting systems. Even within the DMRG, there are several approaches for different problems concerning correlations [57].

In the following subsections, we examine the Hubbard model in some known and some yet unexplored configurations.

4.5.2 Half-filled band

The half-filled Hubbard model $n = N_\uparrow/M = N_\downarrow/M = 1$ was analysed, e.g. using DMRG by Jeckelmann *et al.*[52] (and Benthien *et al.*[57] in the limit of $V = 0$). For a lattice with $M = 30$ sites, a Hubbard interaction of $U = 2.5$ and a broadening of $\eta = 0.1$, we calculate the momentum and frequency resolved spectral function in a frequency resolution of $\Delta\omega = 0.1$. We kept 400 states DMRG in the density matrix using the constant matrix size cut-off scheme, described in section 3.2.1. For about 2400 data points, about 4000 CPU hours were used. The numerical accuracy depends strongly on the Greens function ($\mathcal{A}^>$ or $\mathcal{A}^<$) and the frequency. We employed our manual deconvolution of section 2.4 and subtracted $\eta = 0.1$ from the data. Fig. 4.7 shows the positive k Brillouin zone. Instead of a one particle excitation response, we have weight distributed over a wide range in the diagram. The main features can be explained by a spinon-holon excitation from Bethe ansatz.

The excitation spectrum in the right panel of Fig. 4.7 is the one of a removal of an electron from the system ($\mathcal{A}^<$). Within the Bethe ansatz this is the so-called *spin-charge scattering state* [4], which breaks up into excitations of spinon-holon pairs. While the elementary holon and spinon dispersions (Fig. 4.8) and the combined spinon-holon excitation continuum (Fig. 4.9) are known exactly in the thermodynamic limit, the spectral weight is only known in limiting cases or numerically.

However, the elementary holon and elementary spinon spectra sketched in Fig. 4.8 re-emerge in the scattering state as depicted in Fig. 4.9. Firstly, the spinon lives in half

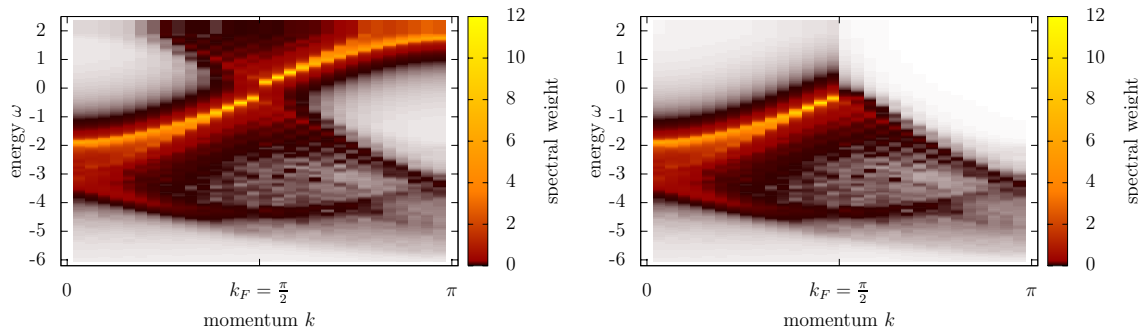


Figure 4.7: Spectral function of the Hubbard chain with $U = 2.5$ and hard-wall boundary conditions. Lattice size $M = 30$ and broadening $\eta = 0.1$. Zero spectral weight is white, while the onset of dark colouring is at about 0.5 % of the maximum. Left plot shows $\pi\mathcal{A}^r$ and the right plot shows $\pi\mathcal{A}^<$.

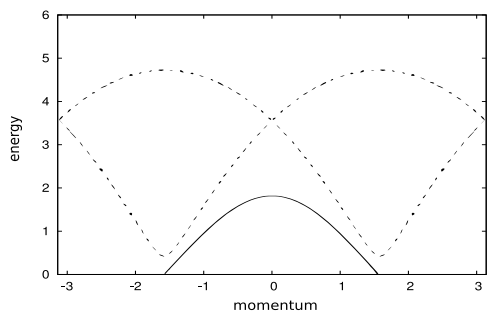


Figure 4.8: Sketched spectrum of spinon (solid) and holon (dashed) dressed energy as a function of their dressed momenta as can be calculated from Bethe ansatz.

of the Brillouin zone with a range of $2k_F$ in $[-k_F, k_F]$ with $k_F = \pi/2$ and contributes to the highest weighted feature in Fig. 4.7 for $[0, \pi]$. Secondly, the holon lives on the full Brillouin zone with a range of $4k_F$ in $[-k_F, 3k_F(\text{mod } 2\pi)]$ and $[-3k_F, k_F]$ for the anti-holon. This contributes in weights from $-k_F$ to $3k_F$ as well as weight from k_F to $5k_F$. When this is folded back into the frame we are looking at in Fig. 4.7, we recover the holon and anti-holon spectra to contribute the second highest weighted feature in the spectral function. All other weight thus stems from spinon-holon continuum excitations. Especially the lower onset of the spectrum below $-5t$ in $[k_F, \pi]$ is given by the spinon-holon continuum. To make the very weak weight visible, the onset of the dark colouring is chosen at about 0.5 % of the maximum.

The Bethe ansatz also reveals that due to a gap in the holon dispersion, the spin-charge scattering state has also a gap at $\pm k_F = \pm\pi/2$. The existence of the gap is better seen in the left panel of Fig. 4.7, where the high weight feature at $\pi/2$ of $\mathcal{A}^<$ displays a gap to the high weight feature of $\mathcal{A}^>$. This is the qualitative difference between this Mott insulator and the metallic state off half-filling.

4.5.3 Below half-filling

The Hubbard model off half-filling $n = \frac{N_\uparrow + N_\downarrow}{2M} \neq 1$ is completely different from the half-filled case. The ground state is now a conductor in that the charge excitations are now

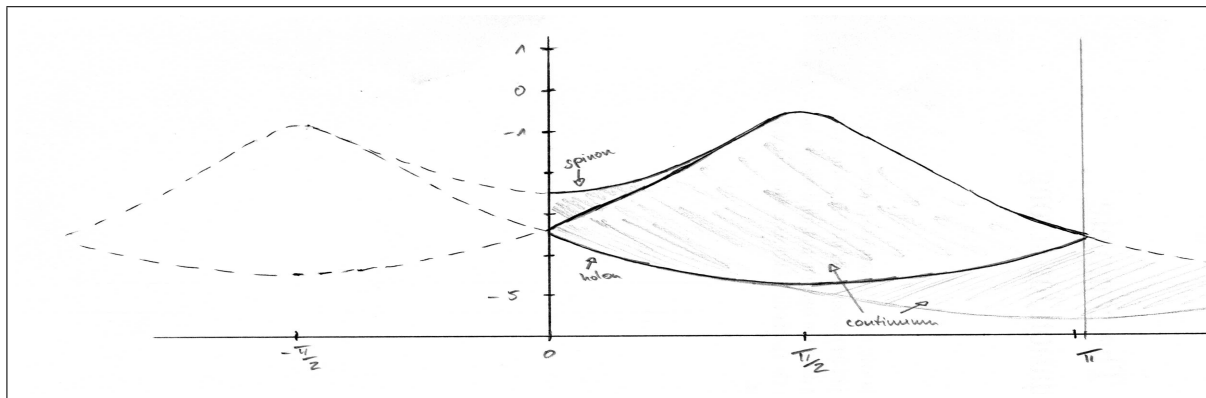


Figure 4.9: Sketch of the spin-charge scattering state excitation spectrum. Compare with Fig. 4.7.

gap-less as well as the spin excitations. This case was extensively dealt with by Benthien *et al.*[53] for $n = 0.6$ and a Hubbard interaction of $U = 4.9t$ using dynamical DMRG keeping up to 400 DMRG states.

Nevertheless, to have direct comparison to the Mott insulator at half-filling of the previous section, we calculate the spectral function for $U = 2.5$ at a filling of $n = 26/30 = 0.8\bar{6}$, using $N_\uparrow = N_\downarrow = 13$ electrons on $M = 30$ sites. Once more, the broadening is $\eta = 0.1$, the resolution $\Delta\omega = 0.1$ and we keep also up to 400 DMRG states of the density matrix blocks with a similar numerical effort (3400 CPU hours) and accuracy.

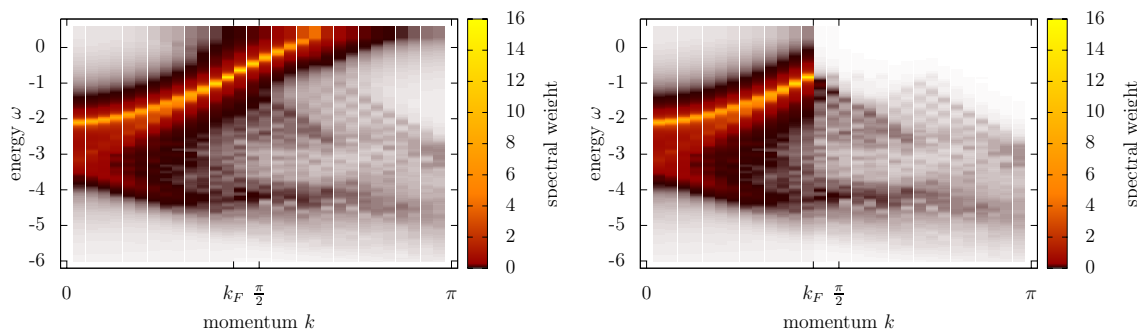


Figure 4.10: Spectral function of the Hubbard chain as in Fig. 4.7 except for the filling of $n = 0.8\bar{6}$. Striking differences are the missing gap at k_F and the incommensurability effects, e.g. the so-called “shadow bands”.

Again, the origin of the most prominent features in the spectral function can be found in the elementary excitations of holon and spinon and the sketch of Fig. 4.8 is still qualitatively valid, except that the holon mode is now gap-less at $\pm k_F$, too. Thus, also the gap in sketch of Fig. 4.9 vanishes, which is one striking difference in Fig. 4.10 compared to the Mott insulator case. The description of the sketches in the last section also applies here with the modification that now $k_F = n\pi/2$. This has the effect for the observables being incommensurate with the lattice. In the spectral function this appears

as another zero mode identical to the one at k_F . This is just the mode at $3k_F$ in the extended Brillouin zone, which lies at $\pi - (3n\pi/2 - \pi) \approx 2.18$ when one folds $3k_F$ back into the first zone. These features are usually called “shadow bands” in the literature. Similarly, the remaining spectrum outside of the first Brillouin zone should be folded back into the first. However, due to the very small weight, most of it is overshadowed by the features original to the first zone.

Note that we have used the particle-hole symmetric version of the Hubbard model for the half-filling case and thus the Fermi energy is shifted by the extra terms by at least $MU(n - 0.5)^2 \approx 0.34$.

4.5.4 Trapped Hubbard model

The recent success with cold atomic gases that can be directly manipulated into forming those microscopic models which we use to describe condensed matter, leads us to examine a typical optical setup: a harmonic trap potential additional to our interacting system. We newly introduce a certain choice of operators that allow a partial evaluation of single particle correlation functions.

We use the bulk Hubbard model and add a harmonic potential $V_{\text{pot}} > 0$

$$H = \sum_{\sigma} H_{\text{tb},\sigma} + U \sum_i n_{i,\uparrow} n_{i,\downarrow} + V_{\text{pot}} \sum_{i,\sigma} n_{i,\sigma} (x_i - x_0)^2, \quad (4.14)$$

which traps the electrons around x_0 . We will choose $x_0 = M/2$ to be in the centre of the system. The density of the ground state will be distributed with a maximum at x_0 and, for a strong enough potential, fall off to zero at some finite value $|x_v - x_0|$. In Fig. 4.11 we plot the density distribution for $V_{\text{pot}} = 0.01$, $M = 50$, $U = 0$ and $N = 11$ together with the interacting density distribution described below.

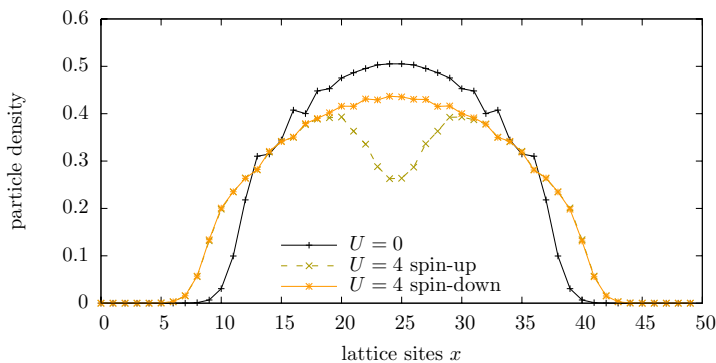


Figure 4.11: Density distribution in a trapped Hubbard model for $M = 50$, $N = 11$ for the non-interacting $U = 0$ case and $N_{\uparrow} = 11$ and $N_{\downarrow} = 11$ in $M = 50$ in the interacting case $U = 4$. The curve showing the dip is where the lowest energy \uparrow -spin state was removed from the $N_{\uparrow} = 11$ ground state.

For the calculation of the single particle spectral function, neither the Bloch states (4.11) nor the solution of the hard wall problem (4.12) are appropriate single particle operators. This is obvious, since the system lacks now the corresponding symmetries. The true analytic solution of (4.14) will not be considered. However, a self-evident and convenient choice is a construction from the solutions of the harmonic oscillator. The

(infinite) quantum harmonic oscillator problem is solved by the Hermite functions, which are Hermite polynomials normed with a Gaussian

$$\psi_m(x - x_0) = \pi^{-\frac{1}{4}} \sqrt{\frac{c}{2^m m!}} H_m(c(x - x_0)) e^{-\frac{1}{2}c^2(x - x_0)^2} \quad (4.15)$$

where c is an arbitrary constant, $m \in \mathbb{Z}^+$, and $H_m(x)$ in the recursive formulation is

$$H_{m+1}(x) = 2xH_m(x) - 2mH_{m-1}(x) \quad \text{with} \quad H_0(x) = 1, H_1(x) = 2x. \quad (4.16)$$

We know that (4.15) will not be exact in some limits due to the lattice and its finite extent. However, we will find a range of validity for these functions to be a very good approximation for the true wave functions.

Non-interacting case

We need to take a closer look on the $U = 0$ (numerically easily accessible) eigenstates of (4.14) to determine the range of validity of (4.15) as trial wave functions. The reason is a competition between the delocalised solution of the (hard-wall) tight-binding chain and the localised Hermite function solutions of a harmonic potential. Comparing the maximal energy of the potential (at the boundary) $V_{\max} = V_{\text{pot}} * (M/2)^2$ to the kinetic energy t gives an estimate for what solutions dominate.

If the trap potential is small ($V_{\max} \ll t$), the wave functions are quasi the sinusoidal solutions of the hard-wall tight-binding chain H_{tb} . Then the Hermite functions are not a good approximation at the boundaries, since they do not fall off to zero within the system size, while the sinus solutions linearly go to zero at the boundary.

If the trap is larger, $V_{\max} \gtrsim t$, the m th wave function (m small) is localised to a small area (depending on V_{pot} and m) within the system and a Hermite function of grade m is the best approximation to the wave function. For these m the spectrum is linear and resembles the quantum harmonic oscillator energy levels. With increasing wave number m the confining area increases and when this reaches the boundary, Hermite functions are again a bad approximation, since the wave function has to be strictly 0 at the boundary. The solutions “see” the finiteness of the system. This defines an upper bound on the number of Hermite functions m that can be used for a single particle description.

One might want to increase the trap strength $V_{\max} \gg t$ such that all M wave functions are well localised in a smaller region $M' < M$, i.e. fall off to zero well before the boundary. However, the m th Hermite function has $m + 1$ nodes and m lobes. Since we are now restricted to M' sites, the sampling resolution is far too small to represent the higher Hermite functions. The solutions “feel” the lattice spacing. This defines another upper bound on the number of Hermite functions m that can be fitted and used for a single particle description. Thus, it depends on the trap potential strength which m is the upper bound on the number of usable Hermite functions.

We use the following scheme: we fix the system size and the trap potential, solve the non-interacting Hamiltonian exactly and fit the first few eigenfunctions to the corresponding Hermite function, with fit parameter c which depends on the trap potential.

From the fit of a Lorentz function with width η on the calculated spectral function for the excited states, we extract the range of valid Hermite function operators. We find empirically that for $V_{\max} \gtrsim t$ only the $\sim M/4$ lowest lying states can be acceptably represented by Hermite functions of degree m .

Interacting case

Turning to the $U \neq 0$ case, we use the restriction on the number of usable Hermite functions as single particle operators which we get from the $U = 0$ comparison above. However, if we assume the lowest numbers of Hermite functions to be exact for our purpose, we can calculate the spectral response as a function of the energy ω and those levels m . The density distribution for $U = 4$ is shown in Fig. 4.11, where we plot for $M = 50, N_{\uparrow} = 11, N_{\downarrow} = 11$ the ground state density and the excited state density, where the lowest energy \uparrow -spin state was removed from the ground state. This corresponds to the action of the operator in $\mathcal{A}^{\leftarrow}(m = 0, \omega)$ on the ground state. The only effect of a finite interaction here is the broadening of the density distribution due to the repulsive nature of $U > 0$.

In the spectral function, however, we expect the single particle excitation response to give way for a more complicated response. The fundamental difference to the Hubbard model is the lack of translational invariance. Therefore, no quasi-momentum exists and the typical terminology of holons and spinon as collective excitations must be redefined, if at all possible. Also, we have no one particle spectrum from a Bethe ansatz solution for the trapped case. Nevertheless, we have a one-dimensional interacting system with linearly dispersing levels. We assume Haldane's conjecture to hold for the trapped system as well and thus interpret the spectral function $\mathcal{A}(m, \omega)$ as we did before for the usual Hubbard model. We can then assume to have separate underlying Luttinger liquids for the charge and the spin sector.

At first, we compare the effect of U on the spectral function $\mathcal{A}(m, \omega)$ in the long wavelength limit, i.e. for the excitation with the smallest quasi-momentum $m = 0$ in a system of $M = 50$ sites, a potential of $V = 0.01$ and a broadening of $\eta = 0.1$. In Fig. 4.12, the broadening for the case $U = 0$ was retained but manually deconvoluted for the other two cases. We see a distinct peak at high energies which broadens with increasing interaction. This would correspond to the spinon excitation in the usual

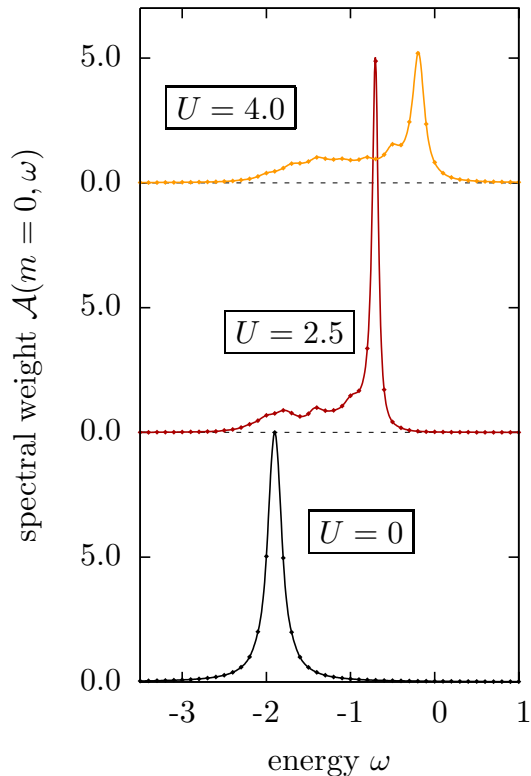


Figure 4.12: Spectral function of a Hubbard model in a trap for different values of the interaction.

Hubbard model away from half-filling. In the range between the energy of the non-interacting delta-response and the high energy peak, there is significant weight, but this is too unspecific. The systems are still too small to determine whether this weight corresponds to an incoherent continuum or if single elementary excitations, similar to the holon, can be identified.

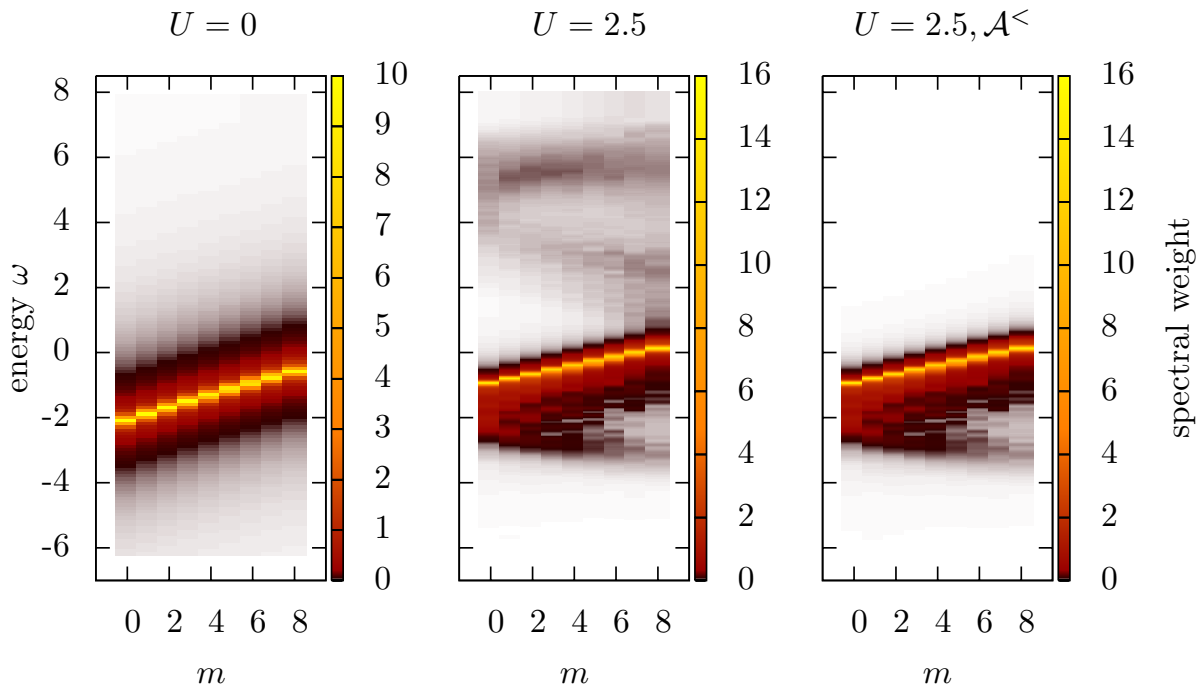


Figure 4.13: Spectral function of the single particle propagator of the Hubbard model in a trap of $V = 0.01$. We compare the $U = 0$ case (left) with a broadening of $\eta = 0.1$ with the $U = 2.5$ case (centre). The right panel shows only $\pi\mathcal{A}^<$ of the $U = 2.5$ case.

Higher momenta For the system of $M = 50$ sites, an interaction of $U = 2.5$ and a potential $V = 0.01$, we calculated for the first 9 levels m the spectral function $\mathcal{A}(m, \omega)$ with a broadening of $\eta = 0.1$, which was removed using manual deconvolution of section 2.4. $N_{\text{cut}} = 700$ DMRG states were kept and about 10,000 CPU hours were consumed. In Fig. 4.13 we compare the non-interacting response in the left panel (with remaining broadening of $\eta = 0.1$ with the interacting response for $U = 2.5$ in the centre and right panel. The centre panel shows $\pi\mathcal{A}$ while the right panel shows only $\pi\mathcal{A}^<$.

Three prominent features occur in the interacting system. The single particle response gets replaced by a shifted sharp response at higher energies with an additional weight at lower energies with a broad energy range. Secondly, within this continuum there are dispersive features not dissimilar to the holon-like dispersion found in other Hubbard models. Finally, there are some dispersive features for higher energies, coming only from the contribution of $\mathcal{A}^>$, when comparing the centre and right panel.

The main spectral weight is on a feature that clearly is not only the shifted single

electron response of the non-interacting system. It displays a dispersion with a different slope and has less weight and what's more, in the next section the spin polarisation will show this feature disappearing with increasing dispersion, just as the spinon response of the plain Hubbard model does. Even if the terminology of spinons and holons are inappropriate in the trapped Hubbard model, there are clear indications of a separation of scales that can, when compared to the Hubbard model, be interpreted as spin and charge sectors.

4.6 Summary

The spin-charge separation is a phenomenon manifest in the Luttinger liquid description as well as in explicit exact solutions of e.g. the Hubbard model. After giving a short introduction to these theoretical approaches, we summarised the experiments on quasi-one dimensional materials. None of the many different experimental projects may claim to see clearly the spin-charge separation.

We added another proposal to directly measure spin and charge wave packets in a *transport setup* as they emerge from an interacting nano-structure, fed by an incident electron wave packet. Current materials and detectors do not allow a direct observation. Thus, while awaiting a feasible experimental realisation, e.g. a chain of quantum dots, our calculations may serve three purposes. Firstly, they answer our question, what happens to an electron in one dimension, in a very didactical manner. We could also reproduce spin and charge velocities of the analytical Bethe ansatz results in a time domain calculation. Finally, our calculations are a vantage point for the exploration of non-equilibrium transport properties, either in the time or the energy domain. Like all numerical tools, time development DMRG is restricted by finite computing resources. Depending on the problem, up to several hundred sites and up to one hundred time steps are the order of magnitude that is realistic in future calculations of this kind.

In the frequency domain, we calculated the single particle *spectral function* $\mathcal{A}(k, \omega)$ in the full energy and momentum range. Using the correction vector method to target the appropriate states in the density matrix, we were able to determine this quantity for the Hubbard model at and off half-filling and extract information about the major responses, which can be related to the holon and spinon spectra available exactly through the Bethe ansatz. Encouraged by the recent rise of cold atom experiments, we checked that the *Hubbard model in a harmonic trap* possesses similar spinon-holon properties in the spectral response. To this end, we newly proposed to use Hermite polynomials in the single particle propagator and investigated their range of validity. This turns out to work well for a few lowest “momenta”. At least the spinon-like peak can be clearly identified and anticipating the results of the next chapter, we can conclude that even in the Hubbard model with a trap, typical one-dimensional physics can be found.

5 Spin polarisation

‘‘Oh no! Not the magnet!’’
(Bender in *Futurama*, Matt Groening)

We find the magnetic field to be a valuable tool for the identification and classification of spin-charge separation when calculating the spectral function, which is experimentally provided by ARPES measurements. There is signature for new physical modes at energies and momenta unexplored by analytical or numerical approaches.

In the spectral function of a one particle (hole) excitation the constituent elementary excitations can be identified in the special case of exactly soluble models. For the SU(2) Hubbard model, this is the spin-charge scattering state of one holon and one spinon as was shown in the previous sections. The identification is possible because the elementary spinon and holon excitation dispersions are represented with a pronounced spectral weight within $\mathcal{A}(k, \omega)$, at least within the range of the spinon spectrum $[-k_F, k_F]$, while the spinon-holon continuum only contributes as a weak background. We have seen that even in the Hubbard model with a confining trap this notion of spin-charge separation is present.

When comparing the spectral function of the non-interacting and the interacting Hubbard model, as e.g. comparing Fig. 4.6 with Fig. 4.7 or within Fig. 4.13 the left and centre panel, the spin and charge features can be quickly identified. However, for more complicated models and for ARPES experiments on yet poorly understood materials this identification is impossible or at least debatable. Models may have no analytic solution that would give a meaning to spin and charge excitation and experiments usually can not turn off the electron-electron interaction to distinguish interacting and non-interacting 1d physics, especially, if there is spin-charge separation or not. This motivates us to investigate the effect of an additional homogeneous magnetic field, which can be (usually very simply) tuned experimentally.

Effect of a magnetic field We assume to have a (quasi-)one-dimensional system with predominant antiferromagnetic, finite-ranged, exchange interaction of the spin degrees of freedom. A homogeneous magnetic field will influence only the spin degrees of freedom and favour ferromagnetic correlations via spin flips. For such a system, there is a saturating ‘‘critical’’ field B_{cr} , above which only one spin kind remains — all spins are aligned. In this ferromagnetic state, the spin-independent dynamics can be represented by a spinless non-interacting fermion model (not considering collective magnon excitations). Then we are able to distinguish two phases: one that has spin-correlations and

might exhibit spin-charge separation and one that is a Fermi liquid. This represents an experimentally easily accessible way to examine a transition from a Luttinger liquid to a Fermi liquid behaviour without deeper knowledge — except for above stated assumptions — of the underlying interactions or models that represent the system.

Method We will turn back to Hubbard models on a finite lattice, to learn more about this transition. Usually, a magnetic field is incorporated as a spin-dependent chemical potential. Since a static magnetic field does not change the total particle number, we will instead look at spin-polarised systems, where the spin-imbalance is explicitly given by integer numbers, such that $N_\uparrow + N_\downarrow = \text{const}$. Thus, exact knowledge of the magnetic field is not necessary. This shifts the Fermi surface of each spin type differently. The polarisation (4.7) can be varied from $p = 0$ (corresponding to $N_\uparrow = N_\downarrow$ and $B = 0$) to $p = 1$, where the system is fully polarised and the field exceeds a critical value B_{cr} , e.g. $N_\downarrow = 0, N_\uparrow = 2N$.

We know the spectral function for both limits. Perfectly balanced systems ($B \rightarrow 0$) show the distinct holon and spinon features of section 4.5.2 and 4.5.3. Fully polarised systems ($B > B_{\text{cr}}$), however, behave like (spinless) non-interacting fermions and show a single particle response (in the majority spins) as shown in section 4.5.1. The intermediate regime has not been looked at to our knowledge. We are curious to know, how the transition from strongly non-interacting spectral features will occur. Somehow, smooth or abrupt, the holon and spinon peaks will have to vanish and the single-electron-peak will have to appear.

We note that a photo-emitted electron could be of either spin orientation in the time-reversal invariant case of $B = 0$. Now, with $B \neq 0$ we need to distinguish two cases of spin orientation, if the electron measurement can be done spin-polarised. However, we assume that measurements that can not determine the emitted electron's spin and calculate the full spectral function from the superposition of the polarised spectral functions

$$\mathcal{A}(k, \omega) = \frac{1}{2}\mathcal{A}_\uparrow(k, \omega) + \frac{1}{2}\mathcal{A}_\downarrow(k, \omega) \quad (5.1)$$

where $\mathcal{A}_\sigma(k, \omega) = -\frac{1}{\pi}\text{Im}[\mathcal{G}_{c_{k\sigma}, c_{k\sigma}}^\dagger(k, \omega)]$ from (2.36).

From the ground state energy for each polarisation we can derive the magnetic field energy contribution $\gamma S_z B_z = E_{\text{GS}}(p) - E_{\text{GS}}(p = 0)$. Using $S_z = \frac{1}{2}pN$, we show the dependence of B_z on the polarisation in Fig. 5.1 as a step function indicating the range of possible magnetic field strengths for each polarisation.

Works in literature The Hubbard model in a magnetic field was analysed in 1990 by Frahm and Korepin [58, 59] with the focus on the asymptotics of the Greens functions in time and space. We know of no exhaustive treatment for $\mathcal{A}(k, \omega)$ for the polarised Hubbard model, but there are theories for the low-energy behaviour, examining various limits [60] and the Mott metal-insulator transition [61]. Also in the low-energy regime Carmelo *et al.* [62, 63] use a pseudofermion formulation to access all momenta (basically corresponding to a momentum distribution curve), and Ref. [59] estimated the behaviour

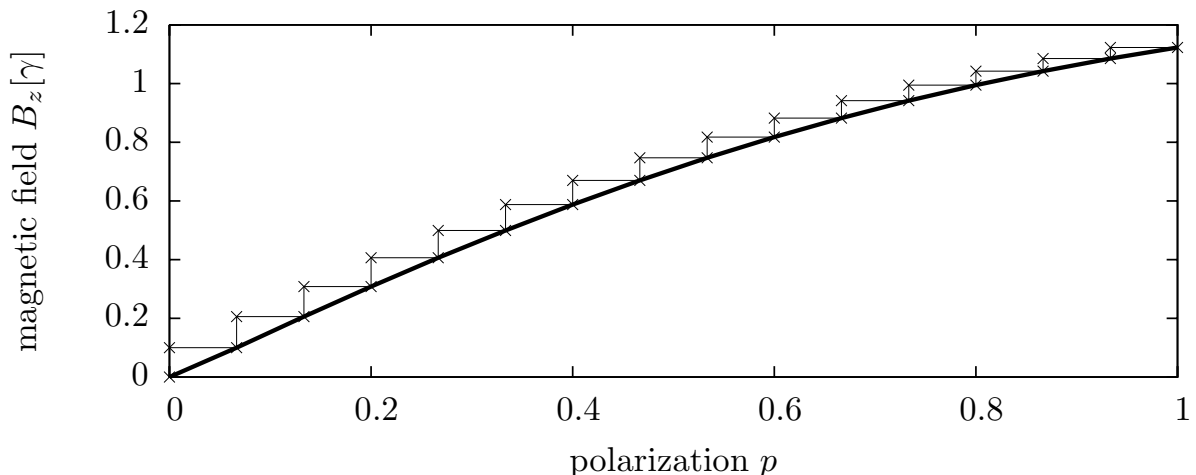


Figure 5.1: Dependence of B_z in units of the gyromagnetic ratio γ on the polarization in the $U = 4$ Hubbard model for density $n = 1.0$.

in the large U limit for special values of ω and k . They find an additional singularity at finite B , which they argue survives for all finite U .

The idea of detecting spin-charge separation by splitting the spectral response with a magnetic field was also formulated by Rabello and Si [64]. However, being restricted to low-lying excitations, their proposal requires an extreme resolution to resolve the splitting of spectral features.

5.1 Tracking spin and charge

In the following paragraphs, we use a Hubbard chain with $U = 4$ without particle-hole symmetry $U \sum_x \hat{n}_{x\uparrow} \hat{n}_{x\downarrow}$. All energies are in units of hopping element $t_{\text{tb}} = 1$.

Below half-filling In the case away from half-filling, we choose a lattice with $M = 32$ sites and $N = N_{\uparrow} + N_{\downarrow} = 26$ electrons. Keeping the filling of $n = 26/32 = 0.8125$ constant, the polarisation (4.7) is therefore varied in steps of $2/26$ by increasing the number of up-spins.

$$p = \frac{N_{\uparrow} - N_{\downarrow}}{N_{\uparrow} + N_{\downarrow}} \in \left\{ \frac{13 - 13}{26}, \frac{14 - 12}{26}, \dots, \frac{26 - 0}{26} \right\} \quad (5.2)$$

The spin and charge identification is very easy for $k \rightarrow 0$, since here the gap between holon and spinon excitation energy is sufficiently large for sufficiently large interaction U and the right choice of band filling, while the spectral weight has also a high contrast. For each polarisation we calculate the spectral function $\mathcal{A}(k_0, \omega)$ with a broadening of $\eta = 0.1$ and with the sinusoidal operators (4.12), since we use hard-wall boundary conditions. Since all coefficients in the sinus series would be zero for $k_0 = 0$, we choose the smallest possible momentum in this discretization $k_0 = \pi/(M + 1) \approx 0.095$. We

employ the fixed-discarded-entropy cutoff scheme of section 3.2.1 aiming for a discarded entropy of 10^{-3} and using up to $N_{\text{cut}} = 1400$ states in the DMRG truncation. The

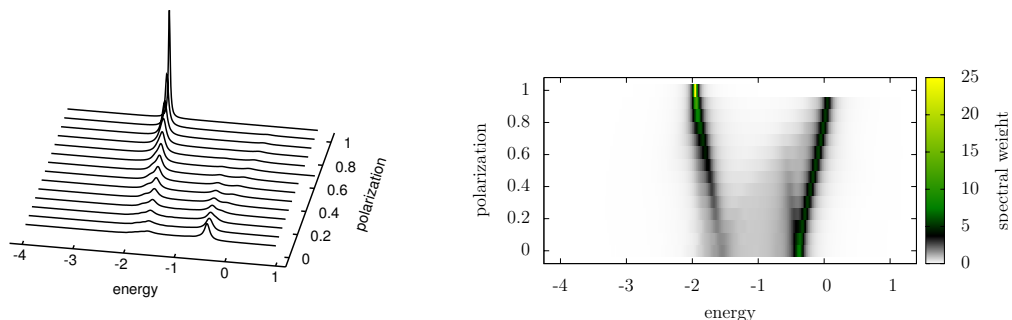


Figure 5.2: Single particle spectral function in the $U = 4$ Hubbard model for $n = 26/32$ for different polarisations as a profile plot (left) and an intensity plot (right).

results in Fig. 5.2 show 100 data points for each of the 14 values of polarisation which consumed about 12,000 CPU hours. The finite size broadening η can be deconvoluted from the data using the technique presented in 2.4. However, since in the limit $p \rightarrow 1$ the spectral function is a pure Lorentz function, broadened by η , a removal would result in a delta-function. Thus, in the data the broadening is reduced from $\eta = 0.1$ to only 0.02, sharpening the Lorentz-peak to a maximum of $1/(2\eta)$ in the fully polarised limit, where the factor of 2 stems from the average in eq. (5.1).

We summarise the important features of the results shown in Fig. 5.2.

- For $p = 0$, we see the *spinon peak* at about $\omega = -0.3$ and the *holon peak* at about $\omega = -1.7$. To higher negative energies, one finds a shoulder to the holon peak. This corresponds to the holon-spinon continuum, which defines the onset of the spectral response. (If we could evaluate $\mathcal{A}(k_0 = 0, \omega)$, there would be no shoulder). There is also finite spectral weight coming from the spinon-holon continuum for $-2 \lesssim \omega \lesssim -0.5$
- Along the polarisation, the holon peak gradually moves to $\omega \rightarrow -2.0$ (precisely, $\omega = -2 \cos(\frac{\pi}{M+1})$). Along this trajectory, it gains weight and transforms into the *electron-hole peak* at $p = 1$, where it has all the weight.
- The spinon peak loses gradually all its weight going to full polarisation. Note that at $p = 1$ there is no weight left. There are, however, two spectral features bifurcating from the spinon peak.

One feature, with less spectral weight, shifts to about $\omega = -0.7$ with a roughly constant distance (“parallel”) to the holon-like peak. It vanishes faster than the second spectral feature, which is another peak with higher amplitude. This peak moves from $\omega = -0.3$ to $\omega \sim 0$ for $p \rightarrow 1$.

Before drawing conclusions, we repeat the procedure for the half-filled case and the Hubbard model in a trap.

At half-filling Analogously, for the half-filled we choose a system with the parameters $M = 30, N_{\uparrow} = N_{\downarrow} = 15$. The filling $n = n_{\uparrow} + n_{\downarrow} = 1$ will be kept constant while increasing the polarisation by increasing the spin-up density. Note that for the $B = 0$ Hubbard model $n = 1$ corresponds to half-filling, while for full polarisation this corresponds to a completely filled non-interacting band. Again, we calculate for each polarisation the spectral function $\mathcal{A}(k_0, \omega)$ with a broadening of $\eta = 0.1$ and with the sinusoidal operators (4.12) and we choose the smallest possible momentum in this discretization $k_0 = \pi/(M+1) \approx 0.101$. We employ the fixed-discarded-entropy cut-off scheme with the same parameters and the broadening was also reduced from $\eta = 0.1$ to 0.02. Although

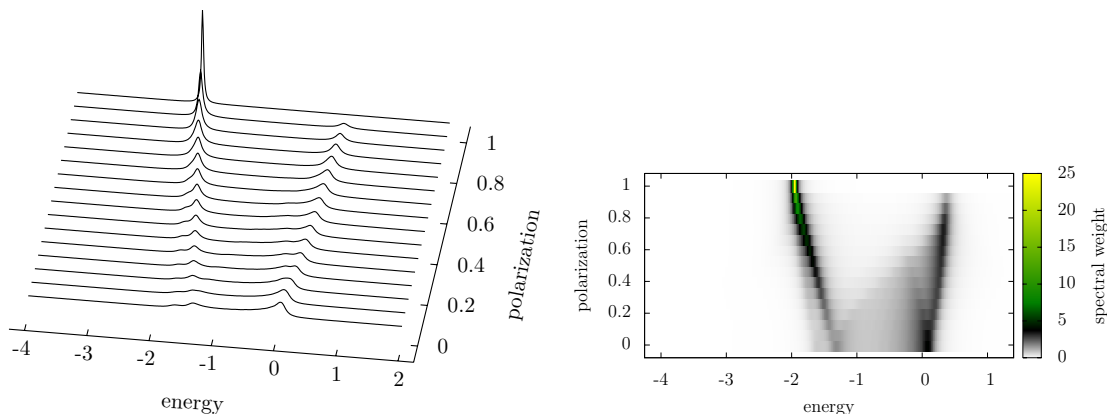


Figure 5.3: Single particle spectral function in the $U = 4$ Hubbard model for $n = 15/30$ for different polarisations as a profile plot (left) and an intensity plot (right).

the half-filled Hubbard model being a Mott insulator is qualitatively completely different from the Hubbard model off of half-filling, we see in Fig. 5.3 a qualitatively analogous behaviour of the spectral function. We identify the same holon-like and spinon-like features which go to the $\omega = -2.0$ single particle peak or vanish, respectively.

Results for a trapped Hubbard model Without prior knowledge of the underlying elementary excitations, we can also extract spectral information for the trapped Hubbard model, described earlier in section 4.5.4. We use a similar system with $M = 50, N_{\uparrow} = N_{\downarrow} = 11, V_{\text{pot}} = 0.01$ and now $U = 4.0$. We employ the cut-off scheme using up to $N_{\text{cut}} = 1400$ states in the DMRG truncation and aim for a discarded entropy of 10^{-3} . The results in Fig. 5.4 were obtained with the fixed-discarded-entropy cut-off scheme using up to $N_{\text{cut}} = 1300$ DMRG states and about 3000 CPU hours were consumed. The four calculated polarisations indicate that there is a low-lying excitation or excitation continuum which transforms into the single particle excitation at full polarisation. And there is an excitation at higher energies, which splits up and loses weight in the full

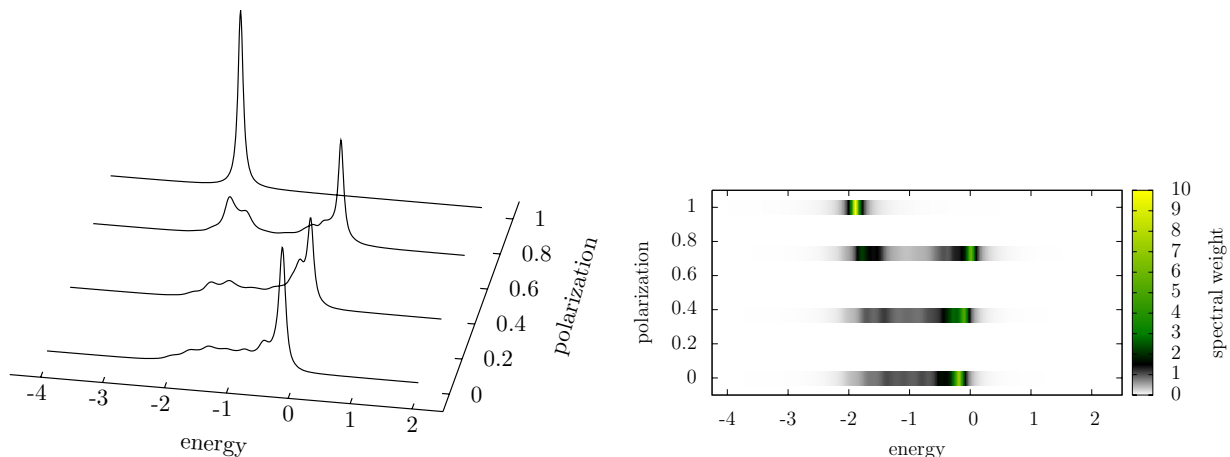


Figure 5.4: Single particle spectral function in the $U = 4$ Hubbard model in a trap for strength $V_{\text{pot}} = 0.01$ for density $n = 11/50$ for different polarisations as a profile plot (left) and an intensity plot (right).

polarised medium. The single particle excitation which is reached at full polarisation is the lowest energy single particle state, whose wave function corresponds to very good approximation to the first Hermite function and the response is again a Lorentzian with width $\eta = 0.1$, sharpened to 0.05. Note that indeed the lowest energy single particle state has an energy of ~ -1.90 and not -2.0 as in the case without a trap.

Discussion First of all, the fact that the basic spinon and holon structure stays intact at finite magnetic field is known [62, 63]. The transition from the one-dimensional interacting physics to the non-interacting physics occurs only trivially at the critical field when no particles are left to interact. This means we do not generally destroy the ability to detect separate spin and charge degrees of freedom at a finite magnetic field.

Secondly, it seems more surprising *how* the single holon and spinon features develop in a magnetic field. One might have expected that the spinon and holon excitation energies would merge at some polarisation value and together form the electronic response or that even more complicated scattering states with several spinons and holons would smear out the picture. This behaviour would make it less favourable to distinguish and detect the peaks experimentally. Looking at the bare energy scales t and $J = -\frac{t^2}{4U}$ of the charge and spin sector, respectively, there is no reason, why these should merge at the long wave limit point $k \rightarrow 0$. Indeed, we find that the effective scales stay clearly separate. Our *main statement* is that the holon peak develops into the electronic charge excitation, while the spinon peak vanishes.

Is there an intuitive way to understand the many-particle behaviour? The holon peak, interpreted in the cartoon picture as a vacancy moving in a background of antiferromagnetically ordered spins, transforms into the hole moving in the background of a fully polarised ensemble of electrons (upon applying a uniform magnetic field). This simple picture suggests that a holon is unimpressed about what background it is moving in and

one accepts this part of the trajectory easily.

For the spinon peak, the cartoon picture suggests that fewer and fewer neighbouring spins can flip (since most are aligned), when turning up the magnetic field. At some point, spin flips are rare, just because there are less spins to flip with. The phase space for spinon-like excitations vanishes and so does the spectral weight of this branch. However, we have no simple cartoon pictured explanation for the shift in energies of the responses nor for the bifurcation of the spinon-like feature. The bifurcation of the spinon-like spectral response warrants a closer look into the full momentum and energy dependency of the spectral function and we will continue the discussion at the end of the next section.

5.2 Spin imbalance: A closer look

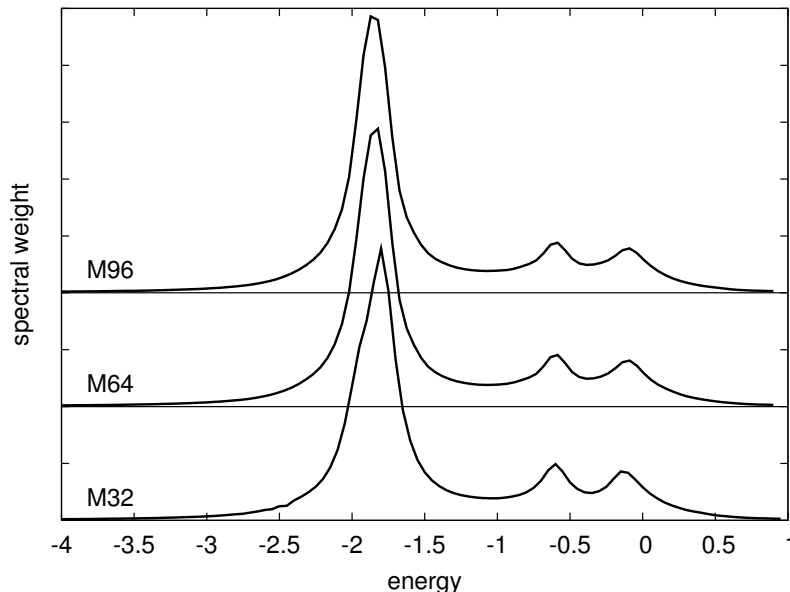
In this section, we first rule out finite size effects of the most interesting features, then we calculate the spectral function in the full spectral range, broken down into contributions from up and down spin channels and from above and below the individual Fermi momenta. Finally, the combination that mimicks an ARPES measurement is presented.

Finite size check To check, whether the main features outlined above do not originate from subtle finite-size effects, we double and triple the system size for the system away from half-filling. Thus, we calculate the spectral function for $M = 64, N = 52$ and $M = 96, N = 78$ for one polarisation only: $p = 14/26$. As will later become more evident, the up-channel spectral function $\mathcal{A}_\uparrow(k_0, \omega)$ shows a pronounced double peak spinon-like structure and is more suitable for a finite size check. The larger systems are computationally harder to calculate. Therefore, we allow to aim for a higher discarded entropy of 0.01, instead of 0.001 for $M = 32$ and allow up to $N_{\text{cut}} = 1200$ states to be kept in one DMRG block. With the resolution of $\omega = 0.1$ in Fig. 5.5 and within the expected accuracy of the procedure, we find no dependence of the general features on the system size.

Polarised spectra In this chapter we calculated up to now the spectral function of the one-electron removal, which is measured by photoelectron spectroscopy (PES). The reverse measurement, the inverse photoelectron spectroscopy (IPES) corresponds to the switching of annihilation and creation operators in the Greens function, which leads to a different spectral function $\mathcal{A}_\sigma^>(k, \omega)$. Thus, $\mathcal{A}^>$ measures the one-electron creation and the analytic behaviour of $\mathcal{A}_\sigma^<(\omega)$ and $\mathcal{A}_\sigma^>(\omega)$ defines the Fermi energy. In a spin-imbalanced system, the spin orientations have different Fermi energies.

We investigate now the system away from half-filling with $M = 32, N = 26$ for the two polarisations $p_1 = 8/26 \approx 0.31$ and $p_2 = 16/26 \approx 0.62$. Fig. 5.6 and Fig. 5.7 show the separate components of $\mathcal{A}_\sigma^\tau(k, \omega)$ for $\tau = <, >$, $\sigma = \uparrow, \downarrow$ for each polarisation, respectively. Between the upper $\mathcal{A}^>$ and lower $\mathcal{A}^<$ panels the Fermi energy can be identified at the momenta $k_{F\sigma}$. For example, for the polarisation $p = (17 - 9)/26$, $k_{F\uparrow} = (17/32)\pi, k_{F\downarrow} = (9/32)\pi$, etc. The calculation with varying resolution down to

Figure 5.5: Finite size check: The spectral function $\mathcal{A}_\uparrow(k_0, \omega)$ for the polarisation $p \approx 0.54$ does not change significantly with $M = 32, 64, 96$ sized systems.



$\Delta\omega = 0.05$ consumed about 10,000 CPU hours for each polarisation. All parameters (accuracy, cutoff scheme) are identical to the corresponding $k_0 \approx 0$ calculations. Note that due to the non-symmetric Hubbard interaction we used, the Fermi energy is not at $\omega = 0$. But, we reproduce the fact that the excitation spectrum is gap-less in the system away from half-filling, even in a magnetic field. This gives a good guide to the eye to locate the Fermi energy for each spin channel separately.

Beside the apparent separated “Fermi surfaces”, the response is asymmetric between the majority and the minority spin channel (compare, e.g. the lower left and right panel of Fig. 5.7). First, we identify a major spinon-like contribution and no holon-like contribution in the spectral response of the down-channel. In contrast, there is the holon-like branch and some weight at the spinon-like branches in the spectral response of the up-channel. This asymmetry, originating in the breaking of time-reversal symmetry, should be noted, since it is inconsistent with the naive cartoon picture where, e.g., the removal of either spin type creates a charge excitation without spin, i.e. the holon branch at zero field is symmetric with respect to the spin quantisation but the holon-like branch at finite field only emanates from the majority spin response.

The spinon-like modes are also unequally distributed. The higher energetic mode results primarily from the down-channel, but there is also some weight from the up-channel yielding an upper branch in the total response (Fig. 5.8). The additional unexpected branch, giving rise to the bifurcation, appears only in the up-channel. More details thereof will be discussed below.

ARPES measurement To complete the picture simulating an ARPES measurement, we plot the spin-averaged $\mathcal{A}^<$ -component for both polarisations in Fig. 5.8 and Fig. 5.9, i.e. we plot $\frac{1}{2}(\mathcal{A}_\uparrow^< + \mathcal{A}_\downarrow^<)$. This corresponds to unpolarised light shining on a sample and measuring the energy of an electron leaving the sample. Fig. 5.8 and Fig. 5.9 compare

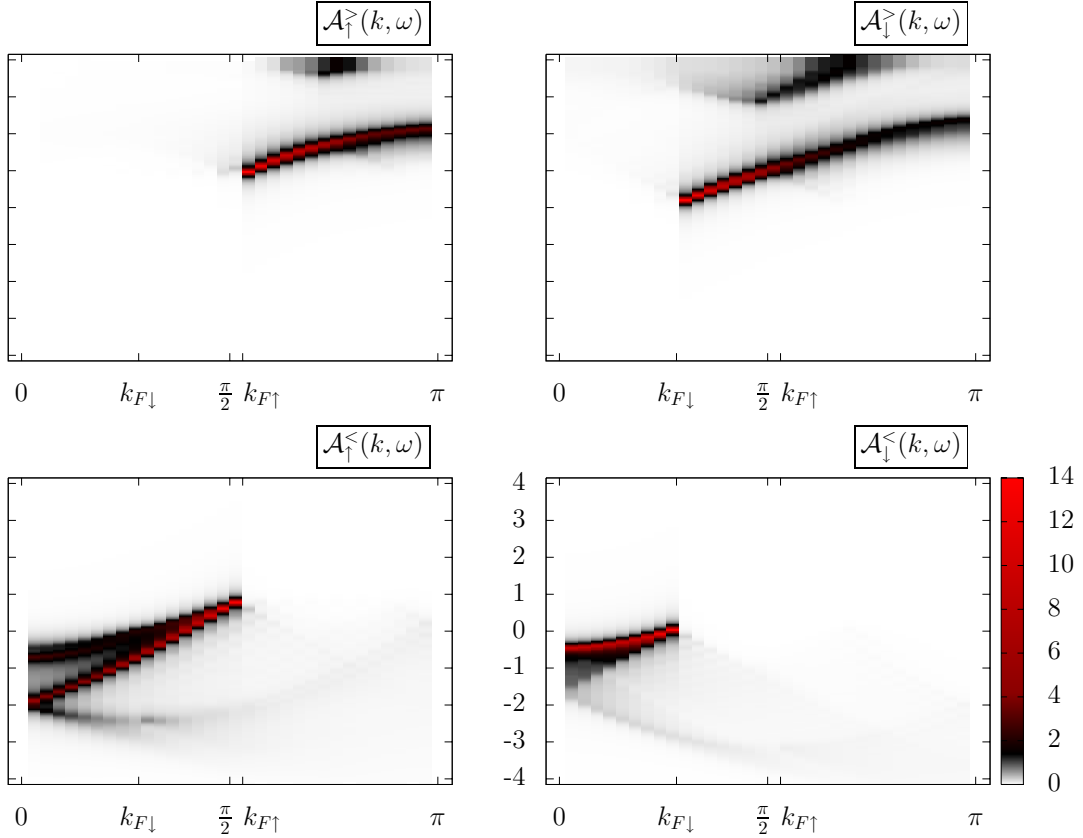


Figure 5.6: Spectral function separated in the different up and down spin and $\mathcal{A}^<$ and $\mathcal{A}^>$ components for the polarisation $p = 8/26$.

directly to the limiting cases at zero magnetic field (right panel of Fig. 4.10, albeit for $U = 2.5$) and the non-interacting limit above full polarisation (right panel of Fig. 4.6). The main effects of the magnetic field show up again in comparison of all four figures.

- When the magnetic field is increased from 0 to full polarisation, the separated Fermi surfaces for each spin orientation become visible.
- Also, an overall redistribution of weight from the spinon-like branch at 0 magnetic field to the holon-like branch and finally into the single-particle branch is observed.

Discussion Extending the discussion of the last section, we recover the bifurcation seen at $k \approx 0$ now in the whole Brillouin zone. It manifests as an **additional spinon-like mode** at energies lower than the spinon-like mode that evolved from the spinon mode at zero field. This additional mode is best visible at the polarisation $p = 16/26$ in Fig. 5.7 in the up-channel spectral function (indicated by a small arrow in the lower left panel), and just noticeable at the polarisation $p = 8/26$ when looking at the combined function in Fig. 5.8. In Fig. 5.6 and Fig. 5.7 we also notice four facts: the additional mode appears *only* in the majority spin channel, it is stronger for smaller polarisation

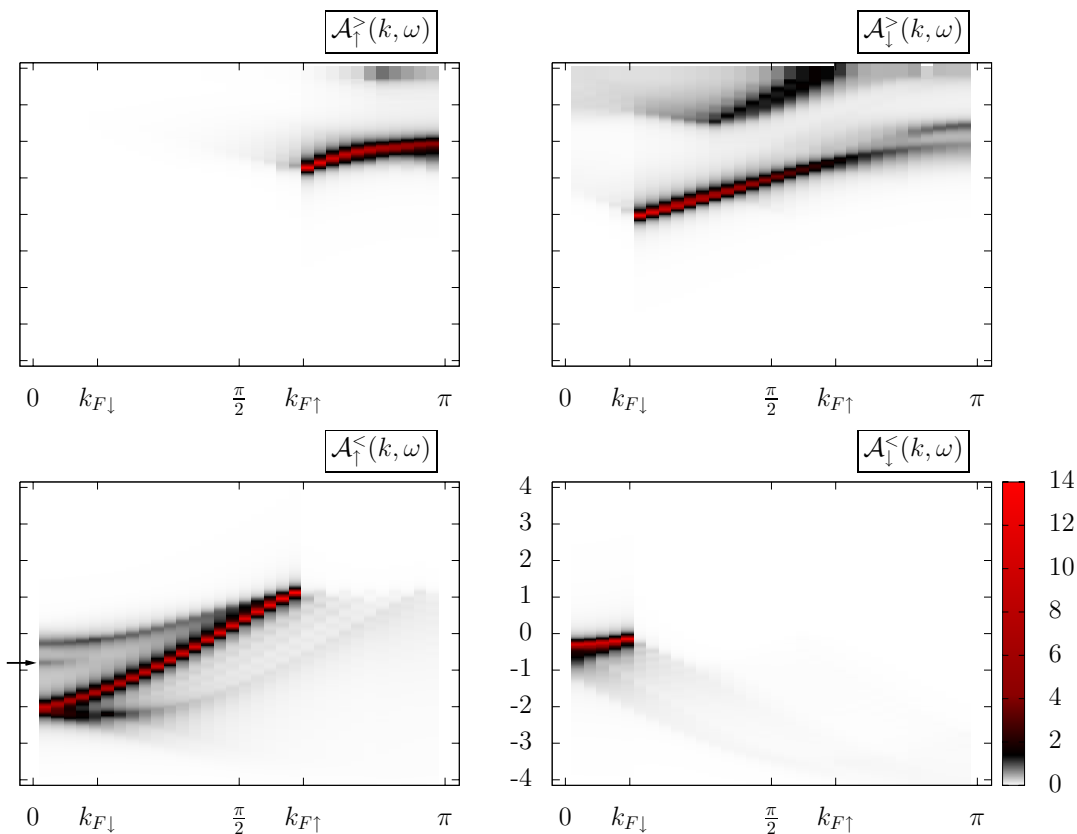


Figure 5.7: Spectral function separated in the different up and down spin and $\mathcal{A}^<$ and $\mathcal{A}^>$ components for the polarisation $p = 16/26$. The small arrow in the lower left panel indicates the unexpected second spinon-like branch.

but less well separated from the upper spinon-like mode and it disperses only up to a momentum, identified as the Fermi momentum of the minority spin channel.

Taking an even closer look, there is a minor **redistribution of weight** from the spinon-like energy region to the holon-like (shadow band) energy region. This feature occurs solely in the spectral response of the majority spin, but it occurs at the Fermi energy of the minority spin $k_{F\downarrow}$. It can best be seen in Fig. 5.7 in the lower left panel, but it also carries through to the total spectral function in Fig. 5.9. Note that it is a high energy effect and thus may not be in the reach of Luttinger liquid description.

These two features are genuinely unexpected results and suggest so far unseen physical excitations, especially since they are closely connected to the symmetry breaking by the magnetic field.

5.3 Summary

Extending the previous research into the spectral function, we looked at the effect of spin-polarisation, which is easily tuned by an external magnetic field. This turned out

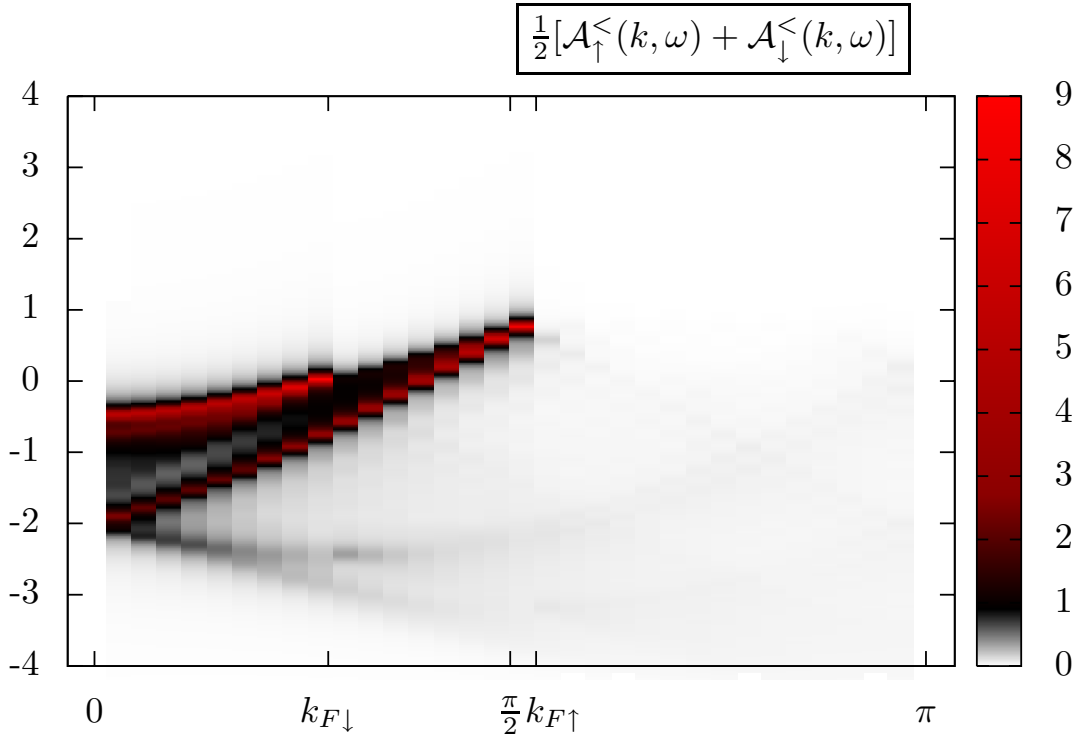


Figure 5.8: Spectral function $\frac{1}{2}(\mathcal{A}_\uparrow^< + \mathcal{A}_\downarrow^<)$ for the polarisation $p = (17 - 9)/26 = 8/26$.

to be a tool that can map out the separated spin and charge sectors over the full range of polarisation. We first investigated the spectral function at $k = 0$ and we found that the separated response peaks do not merge at any polarisation value, rather what is the holon at zero magnetic field becomes the electronic charge peak at the critical magnetic field, while the spinon feature disappears along the way. This was shown for the commensurate and the incommensurate case of the Hubbard model and for the Hubbard model in a trap. While it is possible to tackle the bare Hubbard model analytically with the Bethe ansatz, our findings for a trapped system and early tests on an extended Hubbard model (not presented) indicate that this behaviour extends to non-solvable models and is general for one-dimensional electron systems with a finite-range interaction.

We imagine magnetic fields to be valuable in ARPES studies, where the nature of spectral features are controversial. In cases where it is argued to have one-dimensional physics and spin-charge separation, using the spin polarisation to track the claimed spinon and holon responses will help to justify these claims.

We exploited the advantage over analytical approaches to be unrestricted in energy, momentum and interaction strength and took a closer look on intermediate polarisations. To this end, we computed the separate spectral functions of up and down spin, corresponding to removal or addition of an $S_z = \pm\frac{1}{2}$ electron in the full Brillouin zone. The spectral weight distribution found in this set of quantities would be reproduced by spin-polarised (inverse) photoelectron spectroscopy.

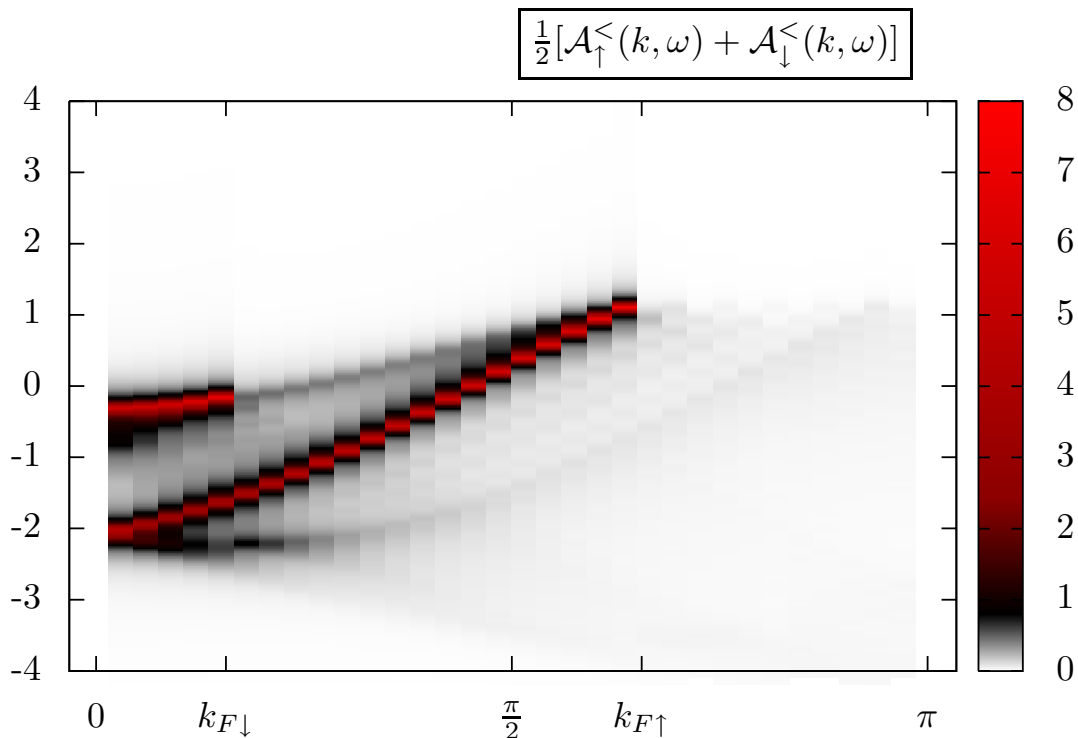


Figure 5.9: Spectral function $\frac{1}{2}(\mathcal{A}_\uparrow^< + \mathcal{A}_\downarrow^<)$ for the polarisation $p = (21 - 5)/26 = 16/26$.

We found that the response of the minority spin orientation does not contribute to the holon-like branch in a finite magnetic field. Furthermore, we identified the previously detected bifurcation at $k \approx 0$ in the full Brillouin zone where it corresponds to two spinon-like branches rooted in the majority spin response albeit entangled to the minority spin. There was an unexpected redistribution of weight which occurred in the majority spin channel but at the Fermi momentum of the minority spin channel.

This asymmetry of the excitation spectrum between majority and minority spin channel suggests a different underlying microscopic picture than the spinon-holon picture of the spin-charge scattering state in the half-filled Hubbard model at zero field. The spin-charge scattering state from Bethe ansatz is spin-rotation invariant in that the spinon and holon description treats spin-up and spin-down on the same footing. Although the spectrum gradually evolves from that spinon and holon description at finite magnetic field, our results clearly verify the symmetry-breaking nature of the elementary excitations. Further insight into the nature and the microscopic picture of the elementary excitations might be gained by finite-field Bethe ansatz calculations.

6 SU(3) colour-charge separation



Flag of Eritrea

There are recent experiments in ultra-cold atomic gases that resemble one-dimensional, strongly correlated SU(3) particles and warrant a numerical investigation of their dynamics.

Motivation So far, we have analysed the spin-charge separation of electronic one-dimensional systems where the electron carries a spin. The corresponding symmetry group is SU(2) and the electron's spin- $\frac{1}{2}$ is its fundamental representation. The next higher dimensional group SU(3) is also common in physics, especially for the global (approximate) symmetry for quark flavours where up, down and strange quarks constitute a triplet of the SU(3) and for the local gauge symmetry of quantum chromodynamics (QCD). In the latter, quarks carry beside the SU(2)-spin and the electric charge a so-called SU(3) colour¹. The fundamental representation of quarks under latter symmetry is the triplet (red, green, blue).

In condensed matter physics, there are no elementary SU(3) particles, like electrons for SU(2). Nevertheless, if one has three energy levels and direct transitions between these levels one may artificially create a particle in the fundamental representation of SU(3). This can be done in ultra-cold atomic gases. Although again not strictly condensed matter, ultra-cold gases present a highly flexible playground [65, 66]. One can restrict the dimensionality and create a crystal structure by trapping atoms in optical lattices, where they form a tight-binding chain. Additionally, an effective interaction can be tuned by the optical lattice and by the means of an atomic Feshbach resonance and finally, temperatures down to 5% of the Fermi temperature can be achieved.

At least the two alkali atoms ${}^6\text{Li}$ and ${}^{40}\text{K}$ seem to be possible candidates for the experimental realisation of an SU(3) fermionic lattice with attractive interactions [67]. In the case of ${}^6\text{Li}$ the scattering lengths for the three possible channels of the three lowest lying hyperfine levels ($|F, m\rangle = |1/2, 1/2\rangle, |1/2, -1/2\rangle, \text{ and } |3/2, -3/2\rangle$) at large magnetic fields become similar for the three of them $a_s \approx -2500a_0$ [68]. The realisation of a stable and balanced three-component Fermi gas has been recently reported [69]. The scattering lengths of the different channels for the three lowest hyperfine states of ${}^{40}\text{K}$ near the Feshbach resonance was also measured and the possibility of trapping them optically was demonstrated [66].

¹Confusingly the quantum number is sometimes called “colour charge”.

We will explore the phenomenology of colour-charge separation in lattice systems with three different kinds of fermions.

6.1 Colour-charge separation in the Hubbard model

Analogous to the $SU(2)$ spin-charge separation, we will analyse an additional $SU(3)$ particle in a partially filled $SU(3)$ Hubbard model, after introducing the basics of $SU(3)$, but we also explore the dynamics of a Gaussian distortion.

6.1.1 Introduction to $SU(3)$

In the following table 6.1.1, we summarise the major properties of the $SU(n)$ symmetry group and their corresponding usage in the physical context of the $SU(2)$ spin symmetry and the $SU(3)$ colour (gauge) symmetry. Note that for the *flavour* $SU(3)$ quark

	$SU(n)$	physical correspondence	$SU(2)$ -spin	$SU(3)$ -colour
number of generators	$n^2 - 1$	generators in fundamental representation operators	3 Pauli matrices \hat{S}^z, \hat{S}^\pm	8 Gell-Mann matrices $\hat{J}^3, \hat{J}^8, \hat{I}^\pm, \hat{U}^\pm, \hat{V}^\pm$
rank	$n - 1$	characterising operators	\hat{S}^z	\hat{J}^3, \hat{J}^8
dimension	n	fundamental representation	spin-up : $S^z = \frac{1}{2}$ spin-down: $S^z = -\frac{1}{2}$	red : $J^3 = \frac{1}{2} \quad J^8 = \frac{1}{3}$ green: $J^3 = 0 \quad J^8 = -\frac{2}{3}$ blue : $J^3 = -\frac{1}{2} \quad J^8 = \frac{1}{3}$

Table 6.1: Table of properties of the $SU(n)$ symmetry groups for $n = 2, 3$

symmetry, the characterising operator \hat{J}^3 is identified with the isospin I and \hat{J}^8 has the meaning of the hypercharge Y . There is no such identification for the QCD colour symmetry, however the notation I, Y is sometimes kept. The major difference to $SU(2)$ is the appearance of a second quantum number for each object. Conveniently one draws a two-dimensional diagram spanned by the quantum number operators J^3, J^8 . Then the red, green and blue particle lie on a triangle whose connections are the ladder operators I^\pm, U^\pm, V^\pm transforming each of the colour particles into the another (see Fig. 6.1).²

²Even if a $SU(2)$ spin $S=1$ object is a completely different object, it has also three different states and the most obvious difference to a $SU(3)$ fundamental particle is that there is no direct operation between the $S^z = 1$ and the $S^z = -1$ quantum number.

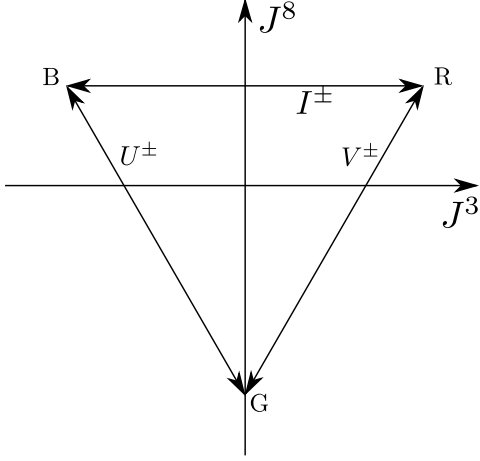


Figure 6.1: Diagram for the fundamental representation of $SU(3)$. Possible states are labelled red (R), green (G) and blue (B) fixed by two quantum numbers J^3 and J^8 . The arrow-headed sides of the triangle represent the ladder operators between the states.

6.1.2 Hubbard model

We setup the $SU(3)$ symmetric one-dimensional Hubbard model with three types of particles with operators $c_{\sigma,x}^{(\dagger)}$ ($\sigma = r, g, b$) and corresponding densities $n_\sigma = c_{\sigma,x}^\dagger c_{\sigma,x}$

$$H = \sum_{x,\sigma=r,g,b} \left(c_{\sigma,x-1}^\dagger c_{\sigma,x} + \text{h.c.} \right) + \sum_x (U_{rg} n_r n_g + U_{gb} n_g n_b + U_{br} n_b n_r), \quad (6.1)$$

where we will distinguish the isotropic case $U_{rg} = U_{gb} = U_{br} = U$ and the anisotropic case of on-site interaction. In the thermodynamic limit the $SU(3)$ Hubbard model has similar phases as the $SU(2)$ Hubbard model. We will consider isotropic interaction for now and identical particle number for all colour degrees of freedom.

While the $SU(2)$ Hubbard model has two phases at $U > 0$, a metallic phase with gap-less charge excitations and a Mott-insulator phase in the commensurate half-filled band with a gap in the charge excitations, the $SU(3)$ Hubbard model is different. For small interactions $0 \leq U < U_{\text{cr}}$ the system is metallic, regardless of the filling [70]. But above a finite U_{cr} there is a phase transition to a Mott-insulator state for commensurate fillings, i.e. $\nu = 1/3$ (or $\nu = 2/3$), when there is one (or two) particle on each site on average. In terms of electron-electron interaction the umklapp-processes lead to a gap in the charge excitations. However, bosonisation shows [70] that umklapp-processes are irrelevant for $U < U_{\text{cr}}$. The critical value was estimated to $U_{\text{cr}} \sim 2.2$ in Quantum Monte-Carlo simulations.

6.1.3 Additional fermion

Completely analogous to the $SU(2)$, we perform time evolution using the full td-DMRG extension on an excited state, in which one (green) fermion was added to the ground state.

Again, a Gaussian distribution of quasi-momenta centred around $k_0 = 0.55\pi$ with width 4.0 in real space ensures a wave packet with energy close to the Fermi surface. The ground state of the system with $M = 42$ sites and $N = 42 * 3/2$ fermions is half-filled

($\nu = 0.5$), i.e. the average particle density is $n = 1.5$. The charge density is given by

$$n_{\text{ch}}(x, t) = n_r(x, t) + n_g(x, t) + n_b(x, t) \quad (6.2)$$

while the density for the two colour quantum numbers are given by

$$\begin{aligned} n_{j^3} &= \frac{1}{2}(n_b - n_r), \\ n_{j^8} &= \frac{1}{3}(n_b + n_r - 2n_g). \end{aligned} \quad (6.3)$$

We employ a three-point average to even Friedel oscillations occurring at this filling due to the hard-wall conditions. We keep up to $N_{\text{cut}} = 4000$ states in the density matrix and let the time evolve 32 time steps of step size $\Delta t = 0.25$. Further we extract the velocity at each time step by fitting one or two Gaussian distribution on the separating peaks. The result is summarised in Fig. 6.2. The density of J^3 is not plotted, since we added

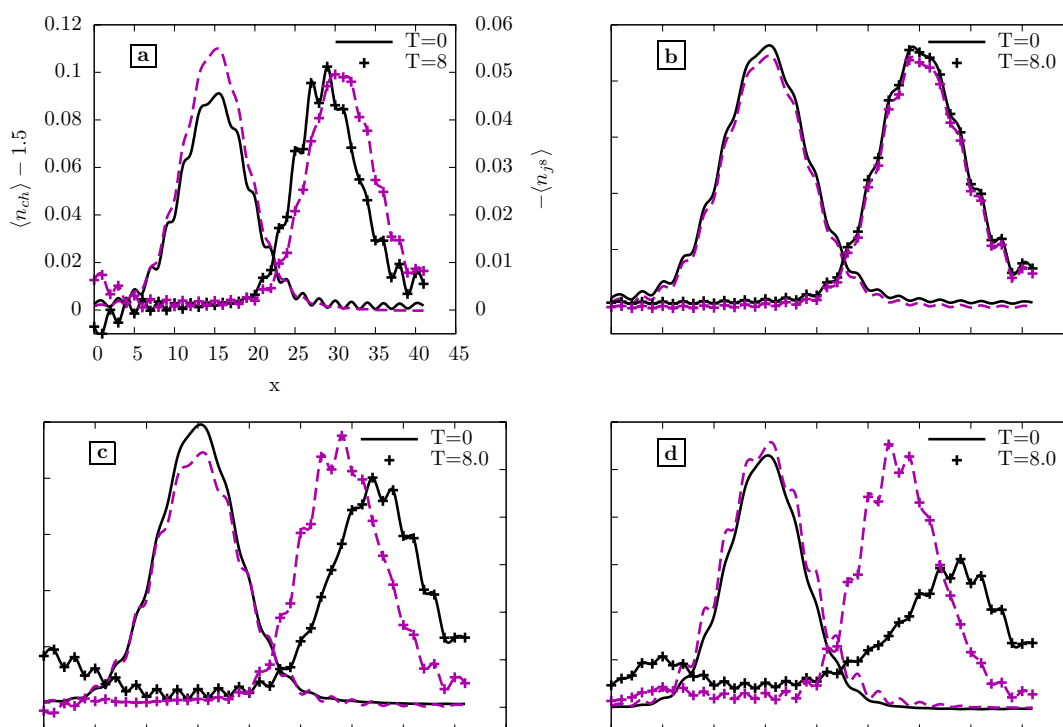


Figure 6.2: Propagation of an added green fermion for the Hubbard interactions $U = -0.5$ (a), $U = 0$ (b), $U = 0.5$ (c) and $U = 2.0$ (d) with hard-wall boundary conditions. The charge density (black) and the density of \hat{J}^8 (purple, dashed) is plotted for times $T = 0$ (lines) and $T = 8.0$ (lines+points).

a green particle, which has the quantum numbers $j^3 = 0, j^8 = -2/3$ and the density n_{j^3} is constant in time. The analogon to spin-charge separation is detected: the colour density is faster for attractive U and slower for repulsive Hubbard U .

We checked if the commensurate case of $1/3$ filling has a qualitative influence on the wave packet propagation, but the systems are too small to be able to see the Mott-insulator-metal phase transition in density propagation or in the bond entropy.

6.1.4 Gaussian perturbation

Despite the enormous resource utilisation of up to 64 GB RAM and months of CPU hours, the inaccuracy of an additional fermion propagation can be seen in the figures. Thus, we choose take a different path and evaluate the propagation of a Gaussian perturbation. With similar parameters, $M = 48$, half-filling $n = 1.5$ but with more than 7000 states in the density matrix, we measure the propagation induced by a distortion with the shape of the derivative of a Gaussian present only at time $T = 0$, see section 2.2. Using this method, a much smoother velocity extraction is possible. To minimise the inaccuracy of fitting and extracting the maximum at each time step, we first look at the function $v(x_{\max})$ instead of $v(T)$. Due to the different velocities of the colour and the charge, we extract a velocity around a site that every density peak has passed (at different times). Finally, the velocity is determined as a Gaussian weighted average around this position.

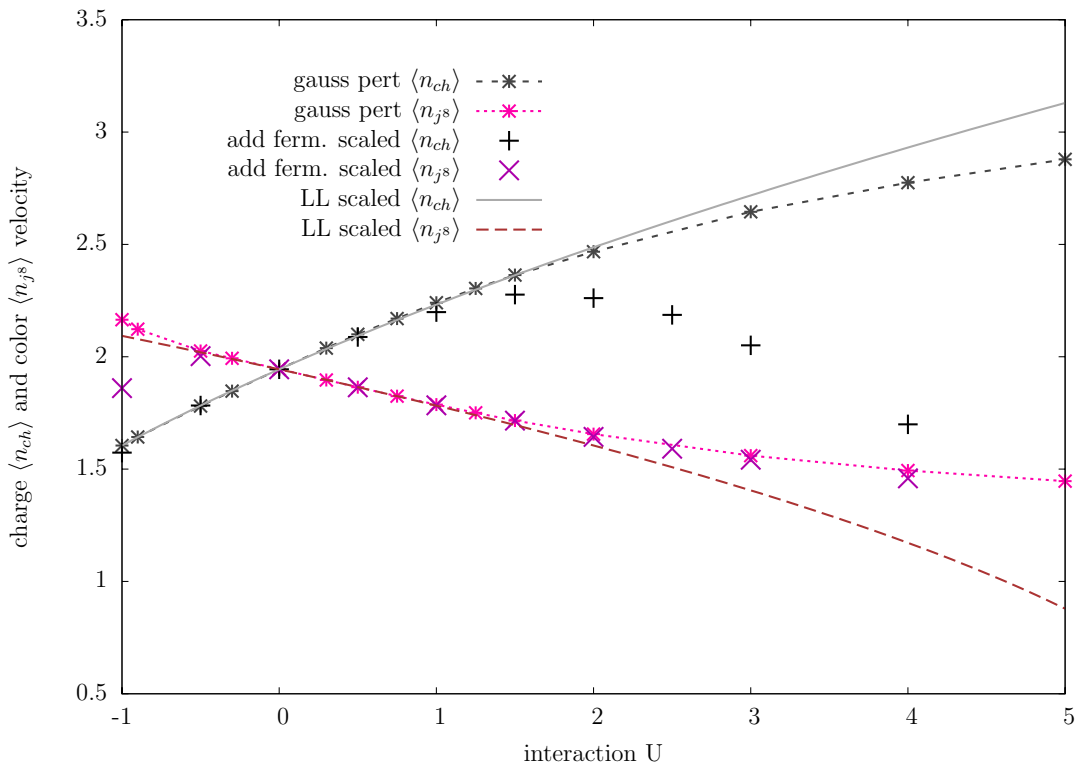


Figure 6.3: Packet velocities in the Hubbard model for different interaction strengths. Indicated by the legend, the solid and long-dashed line correspond to Luttinger liquid results (see text). While the connected points result from an initial perturbation potential, the unconnected points display velocities of an additional particle.

The velocities extracted in this way are plotted in Fig. 6.3. Three sets of velocities are included. The velocities of an additional fermion of the last chapter have to be examined carefully, since we cannot ensure they have reached convergence to the correct states.

However, the velocities extracted from a Gaussian perturbation fit well for a greater range on an analytical curve, which is extracted from a Luttinger liquid description. For attractive interactions $U < -1$, the extraction of the wave packets becomes doubtful, since the shape of the excitation changes, which might be due to many-body excitations that are extremely sensitive to finite-size effects, i.e. the width of the initial perturbation or this indicates the transition into a new physical phase.

As discussed in 2.2 and 2.3, the theoretical velocity at $U = 0$ of $v = 2 \sin k_0 \approx 1.975$ for the added fermion and $v = 2.0$ for the Gaussian perturbation can only be achieved for infinitely broad packets. If we assume that this finite-size slow-down is interaction independent, we can scale all velocities down by the factor given by the extracted velocity at $U = 0$. This was done in Fig. 6.3, where the data and the analytical curve were scaled to match the velocity at $U = 0$ of the Gaussian perturbation.

Bosonisation approach In the bosonisation approach, valid in the weak-coupling limit, the low-energy effective theory of the model can be expressed in terms of the collective fluctuations of the densities of the three species. Introducing three bosonic fields for each colour and combining these as in (6.2) and (6.3) yielding bosonic fields for the charge density and the two colour densities $\phi_{\text{ch}}(x)$, $\phi_{j^3}(x)$, $\phi_{j^s}(x)$, the $SU(3)$ symmetric Hubbard model can be separated within the Luttinger approach into two parts, charge H_{ch} and colour H_{col} . The velocity parameter of each Luttinger liquid can be approximated for small U as

$$\begin{aligned} v_{\text{ch}} &= v_F K_{\text{ch}}^{-1} = v_F \left(1 + \frac{2U}{\pi v_F} \right)^{\frac{1}{2}} \\ v_{\text{col}} &= v_F K_{\text{col}}^{-1} = v_F \left(1 - \frac{U}{\pi v_F} \right)^{\frac{1}{2}} \end{aligned} \tag{6.4}$$

Note the factor of $(n - 1) = 2$ for the $SU(3)$ case in the charge sector compared to the $SU(2)$ case in (4.4). The analytical curves in Fig. 6.3 are given by the right-hand side of these relations. This is valid for small U , where non-linear terms in the Hamiltonians can be neglected and the right-hand side of (6.4) could well be linearised which would not change when comparing with the simulation in Fig. 6.3. For larger $|U|$, the cosine terms in H_{col} lead to deviations, which we can already see in our simulation.

6.2 Summary

In this final chapter, we extended our previously gained knowledge about the $SU(2)$ Hubbard model to the $SU(3)$ case. Motivated by the recent developments in ultra-cold atomic gases, where approximate $SU(3)$ particles can be realised, we showed that the separation of colour and charge in one dimension is manifest in the Hubbard model. Using time evolution DMRG, we simulated both, explicitly added particles and initial perturbation potentials, to extract the colour and charge velocity. Comparing to the analytic Luttinger liquid results, we find excellent agreement of the perturbation potential

over a wide range of interaction and over a smaller range of interactions for the added particle.

A Appendix

A.1 Error analysis for time evolution with DMRG

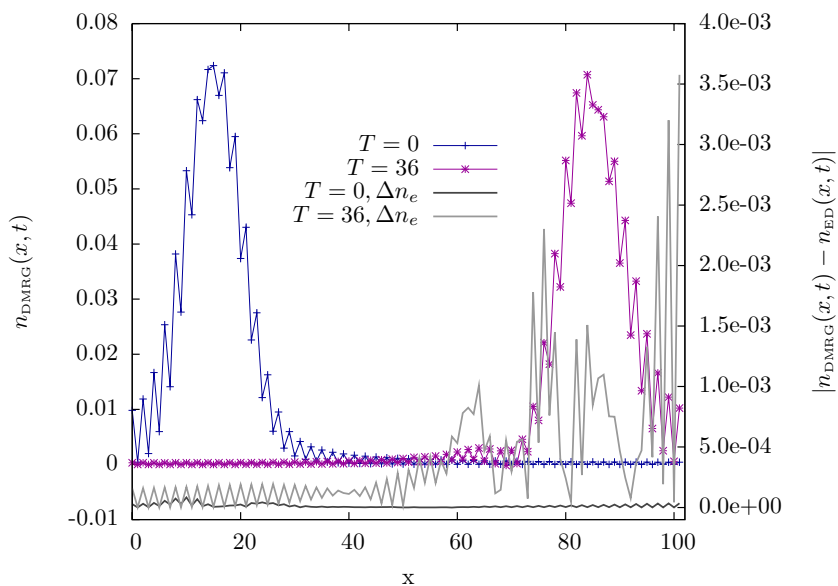
In section 2.3 we have shown the finite size scaling of the time evolution of an electron above the ground state moving in a non-interacting system. We used periodic boundary conditions, which do not lead to Friedel oscillations and ease the extraction of the wave packet propagation in real space.

In this appendix, we analogously investigate the hard-wall boundary case. Then we are able to compare the wave packet velocities from the exact diagonalisation with the $U = 0$ result of our DMRG simulation of the Hubbard model of section 4.4.1. Analogously to figure 2.6, we first extract the evolution of the wave packet velocity, but now for hard-wall boundary conditions. We fit a Gaussian shape for every time step and plot the difference quotient of the fitted centres $c(t)$ at time step t and 0

$$v(t) = \frac{c(t) - c(0)}{t}. \quad (\text{A.1})$$

The data of the wave packet density in real space (subtracted from the ground state stationary density) is shown exemplarily for the two time steps $t = 0$ and $t = 36$ in figure A.1 (left axis). Figure A.2 shows the extracted velocities for the $M = 102$ site

Figure A.1: The time evolved wave packet density at two time steps (left axis) from a DMRG simulation. The absolute error in the density of the DMRG simulation compared to the exact simulation plotted for the same two time steps (right axis).



system with an electronic excitation of momentum $k_0 = \pi/2 + 0.1$ over the half-filled ground state for different widths of the Gaussian. Also analogously to section 2.3, there is a settling time at the beginning, followed by a monotonously increasing window before the packet hits the end of the system and turns around. It was already shown in 2.3 that if the system is large enough, the velocity curve does not depend on the system size, but only on the width of the excitation. The inset shows the scaling behaviour of the velocity with the width of the packet at one fixed time in the window after the settling time (here $t = 13$). We find that the hard-wall boundary condition give the same results as periodic boundary conditions, thus asymptotically approaching the single momentum

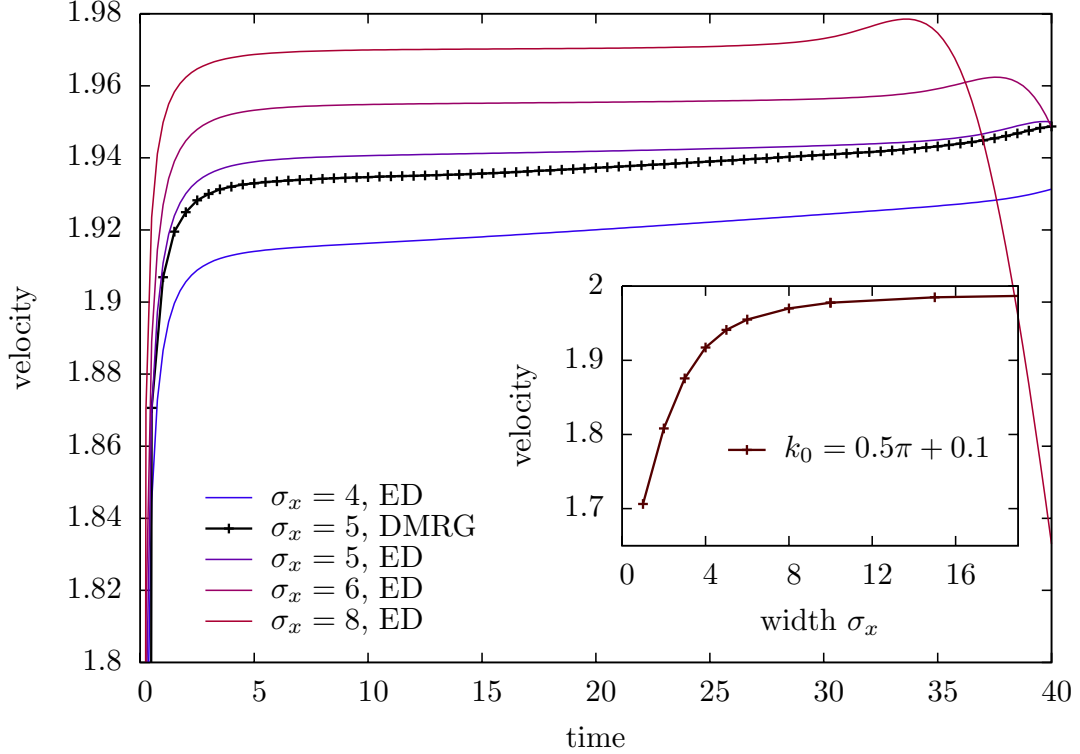


Figure A.2: Wave packet velocity for ED with hardwall boundary conditions on $M=102$ sites compared to DMRG results (black curve) for a fixed width. Inset shows the asymptotic scaling to a single momentum excitation.

excitation result (the ideal limit of an infinitely narrow packet in momentum space), which would travel with velocity $v_\delta = \left. \frac{\partial \varepsilon(k)}{\partial k} \right|_{k_0} = 2 \sin(\pi/2 + 0.1) \sim 1.990$.

Next, the absolute error in the density $|n_{\text{ED}}(t) - n_{\text{DMRG}}|$ of the DMRG simulation compared to the exact diagonalisation (ED) is also plotted in figure A.1. While at $t = 0$ (dark grey) the worst error is at the area of the excitation, at $t = 36$ (light grey) the worst error comes from the boundary and there is also discrepancy between DMRG and ED trailing behind the peak. However, the relative error has only increased from about 10^{-5} to 10^{-3} during the simulation time. The peak relative error as defined in (4.9) is $\delta n_p(0) = 7 \cdot 10^{-5}$ and $\delta n_p(36) = 7 \cdot 10^{-3}$.

The quite accurate results of DMRG in the density is, however, not reflected in the extracted velocity. The reason is that a fitting of the peak centre bears the uncertainty in x-direction, which is not related to inaccuracy in the density, which is orthogonal to the x-direction. Figure A.2 also displays the wave packet velocity of the DMRG simulation (black curve) and the difference between the DMRG result and the exact diagonalisation of the same width $\sigma_x = 5$ is apparent. The error between both is for maximally about $3 \cdot 10^{-3}$ in the velocity. This is not a large error, considering that a fitting procedure is used, but it shows that care has to be taken of an additional source of inaccuracy, when measuring velocities.

A.2 Towards numerics on graphics cards

In our DMRG code we use Posix threads to parallelise the code which is described in detail in [48]. The advantage of this approach lies in the flexibility of choosing worker threads. Here we present first steps to make use of this flexibility by evaluating the possibility to offload workload to acceleration or graphics cards. Within this parallelisation scheme we are not restricted to a single type of worker, but we can schedule different types of workers. We report first benchmark results where we use our threading facility to distribute matrix-matrix multiplications over different worker types, namely one worker that makes use of the GPU on a graphics card to increase throughput.

Single precision

For first benchmarks, we use an older graphics card with single precision hardware (Radeon HD 2400 XT, GPU RV 610), which we can only feed with `sgemm` calls. For compilation we used gcc 4.3.2 (Debian 4.3.2-1.1). In Fig. A.3 we compare ACML (acml-4.2.0), MKL (10.1.1.019/em64t), GotoBLAS [71] (r1.26/penryn) and ACML-GPU (CAL RT & CL v. 1.3.158, acmlg v0.7). Looking at the CPU performance alone one notices that ACML, Goto, and ATLAS give approximately the same performance, with ACML being the fastest of these three libraries. However, MKL gives a factor of two in performance, demonstrating that the choice of BLAS implementation is very important.

The platform used was a quad core Intel-based system (“Intel”) with 8 GB of RAM (See the “highend” version with an upgrade to 8 GB RAM and an Intel Core2 Quad Q9300 processor of <http://portal.uni-freiburg.de/bw-pc/bwpcII>). Next, we use one worker thread that calls the ACML-GPU version of `sgemm` while in the remaining threads we employed the ATLAS (gcc-atlas-acmlg) or MKL (gcc-mkl-acmlg). This version of the ACML-GPU library does not allow to take full control over the distribution of `sgemm` calls to CPU or GPU. Thus, we had problems in linking simultaneously against the ACML-GPU and the normal ACML which stems from namespace clashes in these libraries, since they are not supposed to be used at the same time. Also note, that in the ACML-GPU documentation it is stated that the library is not thread safe and must not be used simultaneously by two different programmes or threads. However, since we have only one GPU worker, while the other workers are not accessing the GPU we are in compliance with this restriction albeit running a multi-threaded code. While at first sight these results do not look very encouraging, it is important to note that these benchmarks are only a proof of concept. Note that within our approach we are not restricted to offload work to a single GPU board. We could even utilise a mixture of acceleration boards.

Double precision

Recently we got access to a machine with a floating point capable graphic card (Radeon HD 4870, GPU RV770). This platform (“AMD”) contains an Phenom(tm) II X4 920

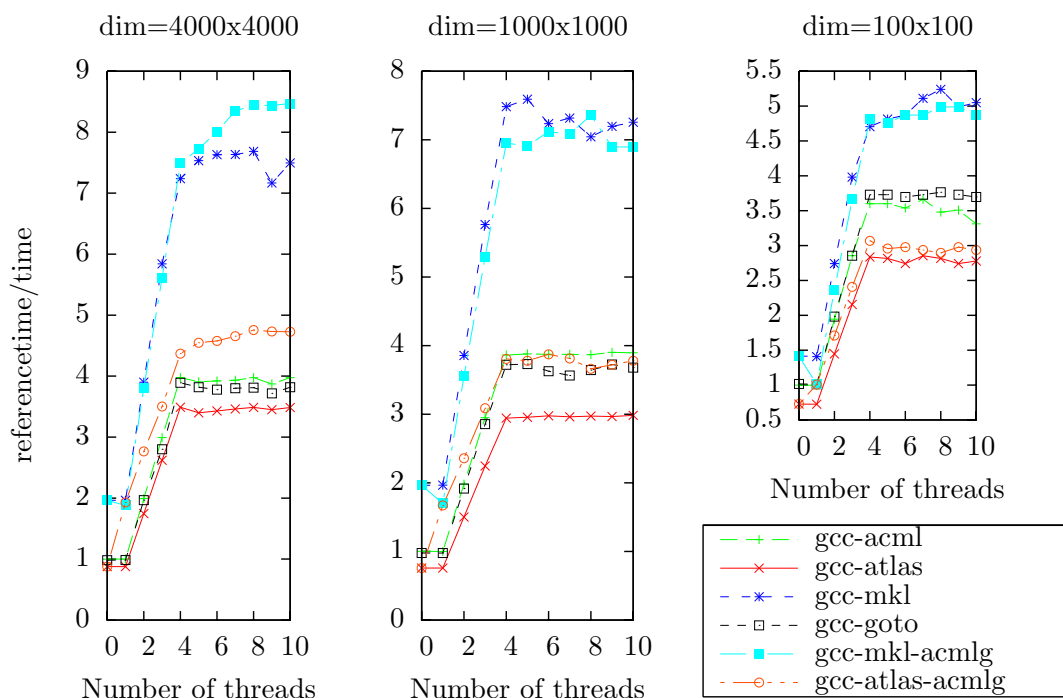


Figure A.3: `sgemm` performance within our multi-threaded testing code on the “Intel” platform (see text) for different BLAS libraries and in two cases with an additional graphics processor unit running one thread of ACML-GPU `sgemm` calls. All data are relative to the `gcc-acml` data serial run at number of threads = 0.

Processor (Quadcore 2.8GHz) with 16 GB RAM. Our benchmark is presented in Fig. A.3. It shows the pure CPU performance (“AMD”) starting from a serial run (number of threads=0) and continuing with up to 10 threads on the CPUs. The scaling up to the 4 CPU cores and the stagnation for more than 4 threads is evident. In contrast, the additional GPU thread result (“+GPU”) shows again a serial CPU run at zero number of threads. The first thread is started on the GPU alone, while more threads are thereafter started on the CPU cores. Thus, a scaling up to 5 threads could be expected, which is not seen. In the compilation, we used MKL (10.1.1.019/em64t) and the GPU libraries CAL RT & CL version: 1.4.227, `acmlg` v1.0.

With this newer hardware the performance boost for the largest matrices due to the graphics card is clearly visible. However, already for the 1000x1000 matrices the quad Intel CPU is of comparable performance. While this benchmark does now look encouraging, the total gain in performance for our DMRG code was marginal. This is to be expected from the benchmark, since the matrices involved were typically smaller than 1000x1000. However, from this benchmark we expect that the use of graphics card is getting interesting for us, if the typical matrix size is at least of the order of 4000x4000. Since we can employ a scheduling depending on the matrix size this will be an interesting option for the future, especially if the BLAS support of the graphics cards improves in the next versions of the ACML. Finally we would like to note that we

also tested an NVIDIA based card. However the library “cublas” is conflicting with our “pthreads”-library leading to spurious deadlocks.

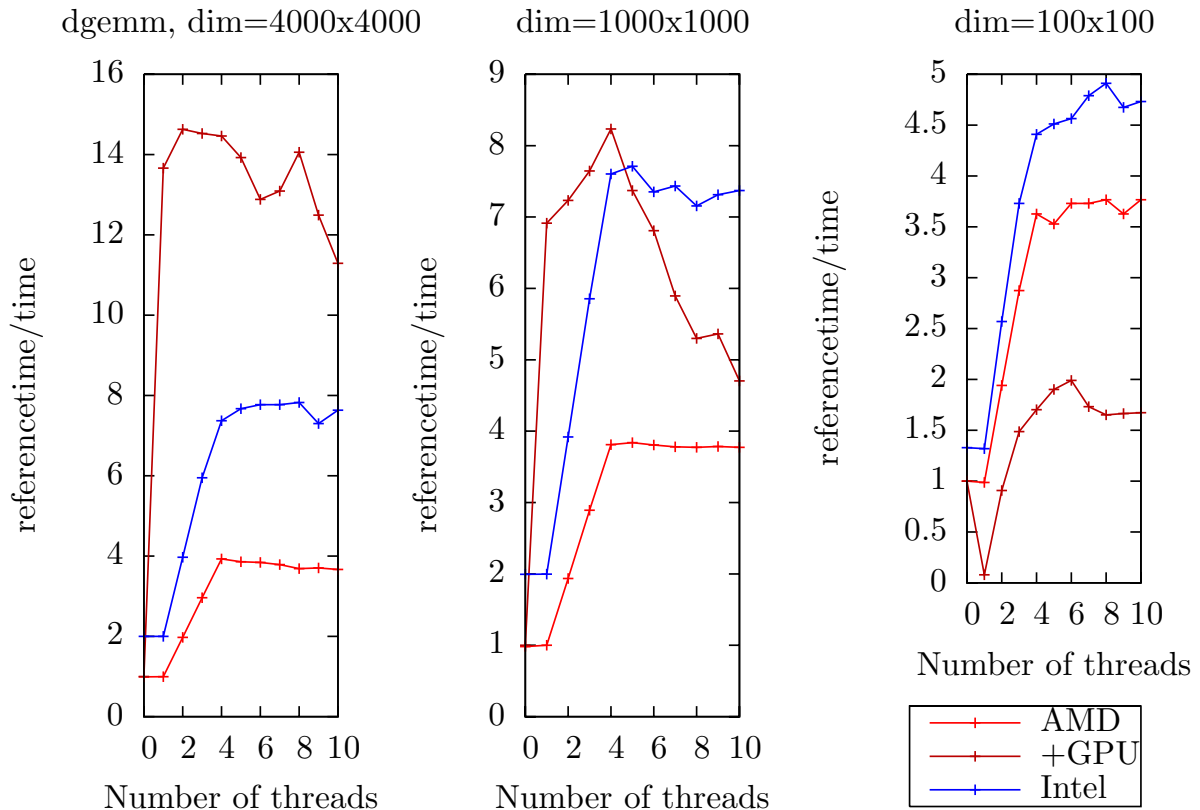


Figure A.4: `dgemm` performance on an AMD platform using only CPUs (AMD), the same platform with one CPU thread replace by a GPU thread (+GPU), compared to the gcc-mkl data of Fig. A.3 (“Intel”)

Bibliography

- [1] Tobias Ulbricht and P. Schmitteckert. Is spin-charge separation observable in a transport experiment? *EPL*, 86(5):57006+, 2009.
- [2] Tobias Ulbricht and Peter Schmitteckert. Signal transport in and conductance of correlated nanostructures. In Wolfgang E. Nagel, Dietmar B. Kröner, and Michael Resch, editors, *High Performance Computing in Science and Engineering '08*, pages 71–82. Springer, Berlin, 2008.
- [3] Matthias Vojta and Tobias Ulbricht. Magnetic excitations in a bond-centered stripe phase: Spin waves far from the semi-classical limit. *Phys. Rev. Lett.*, 93(12):127002–127006, Sep 2004.
- [4] Fabian H. L. Essler, Holger Frahm, Frank Göhmann, Andreas Klümper, and Vladimir E. Korepin. *The One-Dimensional Hubbard Model*. Cambridge University Press, Cambridge, February 2005.
- [5] Reinhard M. Noack and Salvatore R. Manmana. Diagonalization- and numerical renormalization-group-based methods for interacting quantum systems. In Adolfo Avella and Ferdinando Mancini, editors, *Correlated Electron Systems and High-Tc Superconductors*, volume 789, pages 93–163, Salerno, Italy, 2005. AIP.
- [6] Reinhard M. Noack and Salvatore R. Manmana. Diagonalization- and numerical renormalization-group-based methods for interacting quantum systems, Oct 2005.
- [7] Karen A. Hallberg. New trends in density matrix renormalization. *Advances in Physics*, 55(5):477–526, 2006.
- [8] U. Schollwöck. The density-matrix renormalization group. *Rev. Mod. Phys.*, 77(1):259+, 2005.
- [9] Kenneth G. Wilson. The renormalization group: Critical phenomena and the kondo problem. *Reviews of Modern Physics*, 47(4):773–840, Oct 1975.
- [10] Steven R. White. Density-matrix algorithms for quantum renormalization groups. *Physical Review B*, 48(14):10345–10356, Oct 1993.
- [11] Javier Rodriguez-Laguna. *Real Space Renormalization Group Techniques and Applications*. PhD thesis, CSIC Spain, July 2002.
- [12] Cleve Moler and Charles Van Loan. Nineteen dubious ways to compute the exponential of a matrix, twenty-five years later. *SIAM Review*, 45(1):3–49, 2003.

- [13] Peter Schmitteckert. Nonequilibrium electron transport using the density matrix renormalization group method. *Phys. Rev. B*, 70(12):121302, 2004.
- [14] Y. Saad. Analysis of some krylov subspace approximations to the matrix exponential operator. *SIAM Journal on Numerical Analysis*, 29(1):209–228, 1992.
- [15] Roger B. Sidje. Expokit: a software package for computing matrix exponentials. *ACM Trans. Math. Softw.*, 24(1):130–156, 1998.
- [16] Guifré Vidal. Efficient simulation of one-dimensional quantum many-body systems. *Physical Review Letters*, 93(4):040502+, July 2004.
- [17] A. J. Daley, C. Kollath, U. Schollwöck, and G. Vidal. Time-dependent density-matrix renormalization-group using adaptive effective hilbert spaces. *J. Stat. Mech.*, 2004(04):P04005+, 2004.
- [18] Steven R. White and Adrian E. Feiguin. Real-time evolution using the density matrix renormalization group. *Phys. Rev. Lett.*, 93(7):076401, 2004.
- [19] Eric Jeckelmann. Dynamical density-matrix renormalization-group method. *Phys. Rev. B*, 66(4):045114+, Jul 2002.
- [20] Eric Jeckelmann. Density-matrix renormalization group methods for momentum- and frequency-resolved dynamical correlation functions. *Prog. Theor. Phys. Supp.*, 176:143–164, Aug 2008.
- [21] Thierry Giamarchi. *Quantum Physics in One Dimension*. International Series of monographs on physics. Oxford University Press, 2004.
- [22] Johannes Voit. One-dimensional fermi liquids. *Rep. Prog. Phys.*, 58(9):977–1116, 1995.
- [23] Alexander O. Gogolin, Alexander A. Nersesyan, and Alexei M. Tsvelik. *Bosonization and Strongly Correlated Systems*. Cambridge University Press, December 2004.
- [24] J. M. Luttinger. An exactly soluble model of a many-fermion system. *Journal of Mathematical Physics*, 4(9):1154–1162, 1963.
- [25] Sin-Itiro Tomonaga. Remarks on bloch’s method of sound waves applied to many-fermion problems. *Prog. Theor. Phys.*, 5:544–569, 1950.
- [26] H. J. Schulz. Interacting fermions in one dimension: from weak to strong correlation, Feb 1993.
- [27] F. D. M. Haldane. ’luttinger liquid theory’ of one-dimensional quantum fluids. i. properties of the luttinger model and their extension to the general 1d interacting spinless fermi gas. *J. Phys. C*, 14(19):2585–2609, 1981.

- [28] Elliott H. Lieb and F. Y. Wu. Absence of mott transition in an exact solution of the short-range, one-band model in one dimension. *Phys. Rev. Lett.*, 20(25):1445–1448, 1968.
- [29] Minoru Takahashi. One-dimensional hubbard model at finite temperature. *Progress of Theoretical Physics*, 47(1):69–82, January 1972.
- [30] Bertrand I. Halperin. Spin-charge separation, tunneling, and spin transport in one-dimensional metals. *J. Appl. Phys.*, 101(8):081601, 2007.
- [31] T. Lorenz, M. Hofmann, M. Gruninger, A. Freimuth, G. S. Uhrig, M. Dumm, and M. Dressel. Evidence for spin-charge separation in quasi-one-dimensional organic conductors. *Nature*, 418(6898):614–617, August 2002.
- [32] R. Claessen, M. Sing, U. Schwingenschlögl, P. Blaha, M. Dressel, and C. S. Jacobsen. Spectroscopic signatures of spin-charge separation in the quasi-one-dimensional organic conductor ttf-tcnq. *Phys. Rev. Lett.*, 88(9):096402, 2002.
- [33] B. J. Kim, H. Koh, E. Rotenberg, S. J. Oh, H. Eisaki, N. Motoyama, S. Uchida, T. Tohyama, S. Maekawa, Z. X. Shen, and C. Kim. Distinct spinon and holon dispersions in photoemission spectral functions from one-dimensional srcuo2. *Nature Physics*, 2(6):397–401, June 2006.
- [34] Marc Bockrath, David H. Cobden, Jia Lu, Andrew G. Rinzler, Richard E. Smalley, Leon Balents, and P. a. u. l. . L. .. McEuen. Luttinger-liquid behaviour in carbon nanotubes. *Nature*, 397(6720):598–601, February 1999.
- [35] N. Tombros, S. J. van der Molen, and B. J. van Wees. Separating spin and charge transport in single-wall carbon nanotubes. *Phys. Rev. B*, 73(23):233403, 2006.
- [36] O. M. Auslaender, H. Steinberg, A. Yacoby, Y. Tserkovnyak, B. I. Halperin, K. W. Baldwin, L. N. Pfeiffer, and K. W. West. Spin-charge separation and localization in one dimension. *Science*, 308(5718):88–92, April 2005.
- [37] P. Segovia, D. Purdie, M. Hengsberger, and Y. Baer. Observation of spin and charge collective modes in one-dimensional metallic chains. *Nature*, 402(6761):504–507, December 1999.
- [38] J. Schäfer, C. Blumenstein, S. Meyer, M. Wisniewski, and R. Claessen. New model system for a one-dimensional electron liquid: Self-organized atomic gold chains on ge(001). *Physical Review Letters*, 101(23):236802+, 2008.
- [39] J. Graf, G. H. Gweon, K. .. McElroy, S. Y. Zhou, C. Jozwiak, E. Rotenberg, A. Bill, T. Sasagawa, H. Eisaki, S. Uchida, H. Takagi, D. H. Lee, and A. Lanzara. Universal high energy anomaly in the angle-resolved photoemission spectra of high temperature superconductors: Possible evidence of spinon and holon branches. *Phys. Rev. Lett.*, 98(6):067004, 2007.

- [40] C. Kollath, U. Schollwöck, and W. Zwerger. Spin-charge separation in cold fermi gases: A real time analysis. *Phys. Rev. Lett.*, 95(17):176401–4, October 2005.
- [41] A. Kleine, C. Kollath, I. P. McCulloch, T. Giamarchi, and U. Schollwöck. Spin-charge separation in two-component bose gases. *Phys. Rev. A*, 77(1):013607–6, January 2008.
- [42] Alexander Altland, C. H. W. Barnes, F. W. J. Hekking, and A. J. Schofield. Magnetotunneling as a probe of luttinger-liquid behavior. *Phys. Rev. Lett.*, 83(6):1203–1206, Aug 1999.
- [43] Inès Safi and H. J. Schulz. Interacting electrons with spin in a one-dimensional dirty wire connected to leads. *Phys. Rev. B*, 59(4):3040–3059, Jan 1999.
- [44] E. A. Jagla, K. Hallberg, and C. A. Balseiro. Numerical study of charge and spin separation in low-dimensional systems. *Phys. Rev. B*, 47(10):5849–5853, 1993.
- [45] R. Preuss, A. Muramatsu, W. von der Linden, P. Dieterich, F. F. Assaad, and W. Hanke. Spectral properties of the one-dimensional hubbard model. *Phys. Rev. Lett.*, 73(5):732–735, 1994.
- [46] M. G. Zacher, E. Arrigoni, W. Hanke, and J. R. Schrieffer. Systematic numerical study of spin-charge separation in one dimension. *Phys. Rev. B*, 57(11):6370–6375, 1998.
- [47] P. Schmitteckert. Signal transport in and conductance of correlated nanostructures. In Wolfgang E. Nagel, Dietmar B. Kröner, and Michael Resch, editors, *High Performance Computing in Science and Engineering '07*, pages 99–106. Springer, Berlin, 2007.
- [48] P. Schmitteckert and G. Schneider. Signal transport and finite bias conductance in and through correlated nanostructures. In Wolfgang E. Nagel, Willi Jäger, and Michael Resch, editors, *High Performance Computing in Science and Engineering '06*, pages 113–126. Springer, Berlin, 2006.
- [49] E. Boulat, H. Saleur, and P. Schmitteckert. Twofold advance in the theoretical understanding of far-from-equilibrium properties of interacting nanostructures. *Phys. Rev. Lett.*, 101(14):140601, 2008.
- [50] Cornelius F. Coll. Excitation spectrum of the one-dimensional hubbard model. *Phys. Rev. B*, 9(5):2150–2158, 1974.
- [51] H. J. Schulz. Correlated fermions in one dimension. *Int. J. Mod. Phys. B*, 5(1/2):57–74, January 1991.
- [52] Eric Jeckelmann and Holger Benthien. Dynamical density-matrix renormalization group. In *Computational Many-Particle Physics*, volume 739, pages 621–635. Springer, Berlin, 2008.

-
- [53] H. Benthien, F. Gebhard, and E. Jeckelmann. Spectral function of the one-dimensional hubbard model away from half filling. *Phys. Rev. Lett.*, 92(25):256401, 2004.
- [54] A. A. Ovchinnikov. Excitation spectrum in the one-dimensional hubbard model. *Sov. Phys. JETP*, 30:1160+, 1970.
- [55] J. M. P. Carmelo and K. Penc. General spectral function expressions of a 1d correlated model. *Eur. Phys. J. B*, 51(4):477–499, June 2006.
- [56] D. Bozi, J. M. P. Carmelo, K. Penc, and P. D. Sacramento. The ttf finite-energy spectral features in photoemission of ttftcnq: the hubbard-chain description. *J. Phys.: Condens. Matter*, 20(2):022205+, 2008.
- [57] H. Benthien and E. Jeckelmann. Spin and charge dynamics of the one-dimensional extended hubbard model. *Phys. Rev. B*, 75(20):205128–9, May 2007.
- [58] Holger Frahm and V. E. Korepin. Critical exponents for the one-dimensional hubbard model. *Phys. Rev. B*, 42(16):10553–10565, Dec 1990.
- [59] Holger Frahm and V. E. Korepin. Correlation functions of the one-dimensional hubbard model in a magnetic field. *Phys. Rev. B*, 43(7):5653–5662, Mar 1991.
- [60] K. Penc and J. Sólyom. One-dimensional hubbard model in a magnetic field and the multicomponent tomonaga-luttinger model. *Phys. Rev. B*, 47(11):6273–6292, Mar 1993.
- [61] Holger Frahm and Temo Vekua. The mott metalinsulator transition in the 1d hubbard model in an external magnetic field. *J. Stat. Mech.*, 2008(01):P01007+, January 2008.
- [62] J. Carmelo, P. Horsch, P. A. Bares, and A. A. Ovchinnikov. Renormalized pseudoparticle description of the one-dimensional hubbard model thermodynamics. *Phys. Rev. B*, 44(18):9967–9980, 1991.
- [63] J. M. P. Carmelo, F. Guinea, and P. D. Sacramento. Instabilities of the hubbard chain in a magnetic field. *Phys. Rev. B*, 55(12):7565–7578, Mar 1997.
- [64] S. Rabello and Q. Si. Spectral functions in a magnetic field as a probe of spin-charge separation in a luttinger liquid. *EPL*, 60(6):882–888, 2002.
- [65] Immanuel Bloch, Jean Dalibard, and Wilhelm Zwerger. Many-body physics with ultracold gases. *Reviews of Modern Physics*, 80(3):885–964, July 2008.
- [66] C. A. Regal. *Experimental realization of BCS-BEC crossover physics with a Fermi gas of atoms*. PhD thesis, University of Colorado, 2005.
-

- [67] Ákos Rapp, Gergely Zaránd, Carsten Honerkamp, and Walter Hofstetter. Color superfluidity and “baryon” formation in ultracold fermions. *Physical Review Letters*, 98(16):160405, 2007.
- [68] M. Bartenstein, A. Altmeyer, S. Riedl, R. Geursen, S. Jochim, C. Chin, Hecker J. Denschlag, R. Grimm, A. Simoni, E. Tiesinga, C. J. Williams, and P. S. Julienne. Precise determination of ^6Li cold collision parameters by radio-frequency spectroscopy on weakly bound molecules. *Physical Review Letters*, 94(10):103201+, Mar 2005.
- [69] T. B. Ottenstein, T. Lompe, M. Kohnen, A. N. Wenz, and S. Jochim. Collisional stability of a three-component degenerate fermi gas. *Physical Review Letters*, 101(20):203202+, 2008.
- [70] Roland Assaraf, Patrick Azaria, Michel Caffarel, and Philippe Lecheminant. Metal-insulator transition in the one-dimensional $\text{SU}(n)$ hubbard model. *Physical Review B*, 60(4):2299–2318, Jul 1999.
- [71] Kazushige Goto and Robert Van De Geijn. High-performance implementation of the level-3 blas. *ACM Trans. Math. Softw.*, 35(1):1–14, 2008.

Revision: r875